4-2016

Improving Damage Tolerance of Composite Sandwich Structures Subjected to Low Velocity Impact Loading: Experimental and Numerical Analysis

Ravi B. Gondaliya

IMPROVING DAMAGE TOLERANCE OF COMPOSITE SANDWICH STRUCTURES SUBJECTED TO LOW VELOCITY IMPACT LOADING: EXPERIMENTAL AND NUMERICAL ANALYSIS

A Thesis

Submitted to the Faculty

of

Embry-Riddle Aeronautical University

by

Ravi B. Gondaliya

In Partial Fulfillment of the

Requirements for the Degree

of

Master of Science in Aerospace Engineering

April 2016

Embry-Riddle Aeronautical University

Daytona Beach, Florida

IMPROVING DAMAGE TOLERANCE OF COMPOSITE SANDWICH STRUCTURES SUBJECTED TO LOW VELOCITY IMPACT LOADING: EXPERIMENTAL AND NUMERICAL ANALYSIS

by

Ravi B. Gondaliya

A Thesis prepared under the direction of the candidate's committee chairman, Dr. David J. Sypeck, Department of Aerospace Engineering, and co-chairman Dr. Dae Won Kim, Department of Aerospace Engineering and has been approved by the members of the thesis committee Dr. Feng Zhu, Department of Mechanical Engineering. It was submitted to the School of Graduate Studies and Research and was accepted in partial fulfillment of the requirements for the degree of Master of Science in Aerospace Engineering.

THESIS COMMITTEE

David J Sypeck

Committee Chair , Dr. David J. Sypeck

Committee Co-Chair, Dr. Dae Won Kim

Member, Dr. Feng Zhu

Department Chair, Dr. Anastasios Lyrintzis
or Graduate Program Coordinator, Dr. Eric Perrell

29 Apr 2016

Date

Dean of College of Engineering, Dr. Maj Mirmirani

4/29/16

Date

Vice Chancellor, Academic Support, Dr. Christopher Grant

4/29/16

Date

ACKNOWLEDGMENTS

First, I would like to thank Michael Sillus and Gilles Debril from AIRBUS for the initial project conception feedback as well as serving as mentors for the Airbus's biannual 'Fly Your Ideas' challenge. Those endless phone conversations to validate the feasibility of this project were invaluable. It was this global competition that sparked the imagination for creating a solution for damage tolerance issues in composite materials. A great deal of gratitude to Dr. David Sypeck for spending endless hours of testing composite materials and for training me in the usage of specialized machines required for compression and impact testing. His great enthusiasm and zeal for innovative solutions helped propel this thesis work forward. I would also like to thank Dr. Feng Zhu in the Mechanical Engineering Department for teaching me the basics of numerical impact modeling. Without his arduous training, numerical simulation would not have been possible. Special thanks to Dr. Daewon Kim and Dr. David Sypeck for helping me secure internal funding during the conceptual stage of the project. I am also grateful to Dr. Jeff Brown in the Mechanical Engineering Department for helping me with thermographic imaging during the nebulous stage of the idea. Huge thanks go to the National Science Foundation for major research instrumentation and NASA Kennedy Space Center for supporting instrumentation upgrades.

Last but not the least, I am extremely grateful to my friends and family members who kept me motivated and supported me throughout the arduous research journey of mine. Without their emotional support, this work would not have been possible.

TABLE OF CONTENTS

LIST OF TABLES vi
LIST OF FIGURES vii
SYMBOLS x
ABBREVIATIONS xi
ABSTRACT xii
1. Introduction 1
1.1 Problem Statement 2
1.2 Research Purpose 8
1.3 Research Significance 9
2. Prior Investigations 10
3. Experimental Approach 13
3.1 Coupon Fabrication 13
3.1.1 2024-T3 Aluminum Alloy 13
3.1.2 Neat CFRP Prepreg 14
3.1.3 Cores With CFRP Faceskins 15
3.2 Drop-Weight Impact Testing 18
3.3 Experimental Results 19
3.3.1 2024-T3 Aluminum Alloy Sheet 19
3.3.2 Neat CFRP 22
3.3.3 Sandwich Structure With CFRP Faceskins 24
3.4 Compressions After Impact (CAI) Testing 33
4. Numerical Simulation 44
4.1 Aluminum 2024-T3 Impact Simulation 44
4.2 Neat CFRP Plate Impact Simulation 50
4.3 Composite Sandwich Structure (Nomex Core) Impact Simulation 60
5. Conclusions 72
6. Recommendations And Future Work 74
REFERENCES 75
Appendices 79
Appendix A: CFRP Prepreg Material Properties (ACP Composites, Livermore, CA) 79
Appendix B: LS-DYNA Material Type 54-55 Card 81
Appendix C: LS-DYNA Material Type 63 Card 87
Appendix D: LS-DYNA Material Type 4 Card 89

Appendix E: Aluminum 2024-T3 Alloy Sheet Mechanical Properties 92

LIST OF TABLES

Table 1. Input mechanical properties of 2024-T3 sheet for MAT_PLASTIC_KINEMTATIC material card (Type 3). 46
Table 2. Input mechanical properties of the individual ply entered in FEMAP. 52
Table 3. Input mechanical properties of CFRP laminate (Type 54-55). 55
Table 4. Input mechanical properties of Nomex® honeycomb in Hypermesh 61
Table 5. Input mechanical properties of top and bottom plate. 63
Table 6. Input mechanical properties of 7 layered CFRP facing skins (Type 54-55). 68
Table 7. Numerical vs. Experimental Energy (J) absorbed for composite sandwich. 68

LIST OF FIGURES

Figure 1. Increased usage of composite structures in next generation aircrafts. 2
Figure 2. Composite usage in Airbus A350 XWB. 2
Figure 3. Through-the-thickness tensile strength comparison. 3
Figure 4. General locations of an impact on an AIRBUS aircraft. 4
Figure 5. BVID example on Airbus A330 after horizontal stabilizer accident. 5
Figure 6. Sub-laminates (top) and buckled sub-laminates in compression (bottom). 6
Figure 7. Delamination orientation dependence on ply angles of a laminate. 7
Figure 8. Steel-Rubber-Composite hybrid material after low velocity impacts. 12
Figure 9. Wabash Compression Press (left) and Leco MSX255 Benchtop Sectioning Machine (right). 15
Figure 10. Composite sandwich fabrication process and final cross-sections of fabricated coupons. 17
Figure 11. Instron 9250 HV Impact Test Instrument. 19
Figure 12. Post impacted 2024-T3 aluminum alloy sheet coupons. 20
Figure 13. Displacement (mm) vs. Time (ms) curves for 2024-T3 aluminum alloy sheet at varying impact velocities. 20
Figure 14. Energy (J) vs. Time (ms) curves for 2024-T3 aluminum alloy sheet at varying impact velocities 21
Figure 15. Force (kN) vs. Time (ms) curves for 2024-T3 aluminum alloy sheet at varying impact velocities 21
Figure 16. Displacement (mm) vs. Time (ms) curves for $(CF)_{14}$ and 2024-T3 at varying impact velocities 23
Figure 17. Energy (J) v/s Time (ms) curves for $(CF)_{14}$ and 2024-T3 at varying impact velocities. 23
Figure 18. Force (kN) vs. Time (ms) curves for $(CF)_{14}$ and 2024-T3 at varying impact velocities. 24
Figure 19. Displacement (mm) vs. Time (ms) curves for $(CF)_{14}$ and CFRP sandwich structures at different impact velocities. 25
Figure 20. Specific Energy (J/g) vs. Time (ms) curves for $(CF)_{14}$ and CFRP sandwich structures at different impact velocities. 26
Figure 21. Force (kN) vs. Time (ms) curves for $(CF)_{14}$ and CFRP sandwich structures at different impact velocities. 26
Figure 22. Specific Energy (J/g) vs. Time (ms) for the sandwiches impacted at 3.0 m/s impact velocity. 28
Figure 23. Energy Per Thickness (J/mm) vs. Time (ms) for the sandwiches impacted at 3.0 m/s impact velocity. 28
Figure 24. D3O® mesh with interlocking mechanism schematic. The thickness of the mesh is 0.40 cm. 29
Figure 25. FEI Quanta 650 with a Bruker EDX system at ERAU SEM Laboratory. 30
Figure 26. Cressington 108 Sputter Coater at ERAU SEM Laboratory. 31
Figure 27. 50x SEM magnification image of D3O® sample. 32
Figure 28. 400X SEM magnification image of D3O® sample. 33
Figure 29. Assembled CAI test fixture (no specimen installed). 34
Figure 30. Instron 8802 with CAI test fixture 36

Figure 31. Compressive failure modes. End crushing brooming (left) and edge compression shear (middle and right). 36
Figure 32. CAI test of 14 layered CFRP impacted at 1.25 m/s. Before (left) and after (right) CAI test images shown. 38
Figure 33. CAI tested 14 layered CFRP coupons (top face). Impacted and unimpacted coupons (left to right). 38
Figure 34. CAI tested 14 layered CFRP coupons (bottom face). Impacted and unimpacted coupons (left to right). 39
Figure 35. Stress vs. Strain curve of the impacted and unimpacted CFRP coupons during CAI tests. 39
Figure 36. CAI tested CFRP sandwich coupons (front face). Impacted at 1.25 m/s. 41
Figure 37. CAI tested CFRP sandwich coupons (bottom face). Impacted at 1.25 m/s. ... 41
Figure 38. CAI tested CFRP sandwich coupons (front face). Impacted at 3.0 m/s. 42
Figure 39. CAI tested CFRP sandwich coupons (bottom face). Impacted at 3.0 m/s. 42
Figure 40. Specific Stress vs. Strain curve of the impacted CFRP sandwich coupons during CAI tests. 43
Figure 41. Meshed model of 2024-T3 sheet and indenter in Hypermesh. 46
Figure 42. Numerical vs. Experimental comparison of Displacement (mm) vs. Time (ms) curves for 2024-T3 specimen at 1.0 m/s impact. 47
Figure 43. Numerical vs. Experimental comparison of Energy (J) vs. Time (ms) curves for 2024-T3 specimen at 1.0 m/s impact. 47
Figure 44. Numerical vs. Experimental comparison of Force (kN) vs. Time (ms) curves for 2024-T3 specimen at 1.0 m/s impact. 48
Figure 45. Numerical vs. Experimental comparison of Displacement (mm) vs. Time (ms) curves for 2024-T3 specimen at 1.25 m/s impact. 48
Figure 46. Numerical vs. Experimental comparison of Energy (J) vs. Time (ms) curves for 2024-T3 specimen at 1.25 m/s impact. 49
Figure 47. Numerical vs. Experimental comparison of Force (kN) vs. Time (ms) curves for 2024-T3 specimen at 1.25 m/s impact. 49
Figure 48. ABD matrix calculation in Femap. 52
Figure 49. CFRP plate modelling with impact indenter. 55
Figure 50. Numerical vs. Experimental comparison of Displacement (mm) vs. Time (ms) curves for 14 layered neat CFRP specimen at 1.00 m/s impact. 56
Figure 51. Numerical vs. Experimental comparison of Energy (J) vs. Time (ms) curves for 14 layered neat CFRP specimen at 1.00 m/s impact. 57
Figure 52. Numerical vs. Experimental comparison of Force (kN) vs. Time (ms) curves for 14 layered neat CFRP specimen at 1.00 m/s impact. 57
Figure 53. Numerical vs. Experimental comparison of Displacement (mm) vs. Time (ms) curves for 14 layered neat CFRP specimen at 1.25 m/s impact. 58
Figure 54. Numerical vs. Experimental comparison of Displacement (mm) vs. Time (ms) curves for 14 layered neat CFRP specimen at 1.25 m/s impact. 58
Figure 55. Numerical vs. Experimental comparison of Force (kN) vs. Time (ms) curves for 14 layered neat CFRP specimen at 1.25 m/s impact. 59
Figure 56. Initial (left) and final (right) displacement contour of 14 layered neat composite sheet at 1.25 m/s. 59

Figure 57. Numerical (top) vs. Experimental (bottom) rear damage at impact velocity of 2.0 m/s. 60
Figure 58. Crush test (top left), experimental stress-strain curve (top right) and FEA modelling of compressive test (bottom). 62
Figure 59. Numerical vs. Experimental Stress (GPa) vs. Strain curves for Nomex® honeycomb structure. 64
Figure 60. Energy (J) vs. Time (ms) curve for CFRP Nomex® sandwich structure impacted at 1.0 m/s. 65
Figure 61. Energy (J) vs. Time (ms) curve for CFRP Nomex® sandwich structure impacted at 1.25 m/s. 65
Figure 62. Energy (J) vs. Time (ms) curve for CFRP Nomex® sandwich structure impacted at 3.0 m/s. 66
Figure 63. Von Misses Stress (GPa) contour on Nomex® honeycomb at 1.0 m/s impact. 69
Figure 64. Von Misses Stress (GPa) contour on Nomex® honeycomb at 1.25 m/s impact. 70
Figure 65. Von Misses Stress contour (GPa) on Nomex® honeycomb at 3.0 m/s impact. 71

SYMBOLS

$(CF)_7$	7 Layered Carbon Fiber Laminate
$(CF)_{14}$	14 Layered Carbon Fiber Laminate
E	Elastic Young's Modulus
E_1	Young's Modulus In In-plane Direction 1 (Longitudinal)
E_{1f}	Fiber Young's Modulus In In-plane Direction 1 (Longitudinal)
E_{1m}	Matrix Young's Modulus In In-plane Direction 1 (Longitudinal)
E_2	Young's Modulus In In-plane Direction 2 (Transverse)
E_A	Young's Modulus In In-plane Direction 2 (Longitudinal)
E_B	Young's Modulus In In-plane Direction 2 (Transverse)
e_c	Chang-Chang Failure Factor for Compression Failure Mode
e_d	Chang-Chang Failure Factor for Compression Matrix Mode
e_f	Chang-Chang Failure Factor for Tensile Failure Mode
e_m	Chang-Chang Failure Factor for Tensile Matrix Mode
G_{12}	In-plane Shear Modulus
G_{AB}	In-plane Shear Modulus
ϑ	Poisson's Ratio
ϑ_{12}	In-plane Poisson's Ratio
ϑ_{AB}	In-plane Poisson's Ratio
ρ	Density
S_C	In-plane Shear Strength
SC	In-plane Shear Strength
σ_{aa}	Tensile/Compressive Stress (Longitudinal)
σ_{ab}	In-plane Tensile/Compressive Stress in 1-2 plane
σ_{bb}	Tensile/Compressive Stress (Transverse)
σ_y	Yield Strength
V	Volume Fraction
V_f	Fiber Volume Fraction
V_m	Matrix Volume Fraction
X_c	Longitudinal Compressive Strength
X_t	Longitudinal Tension Strength
XC	Longitudinal Compressive Strength
XT	Longitudinal Tension Strength
Y_C	Transverse Compressive Strength
Y_t	Transverse Tension Strength
YC	Transverse Compressive Strength
YT	Transverse Tension Strength

ABBREVIATIONS

ASTM	American Society For Testing And Materials
BVID	Barely Visible Impact Damage
CAI	Compression After Impact
CFRP	Carbon Fiber Reinforced Polymer
FEA	Finite Element Analysis
FS	Failure Strain
GFRP	Glass Fiber Reinforced Polymer
NDE	Nondestructive Evaluation
SEM	Scanning Electron Microscope
TSC	Tensile Stress Cutoff

ABSTRACT

Gondaliya, Ravi MSAE, Embry-Riddle Aeronautical University, March 2016. Improving Damage Tolerance Of Composite Sandwich Structures Subjected To Low Velocity Impact Loading: Experimental And Numerical Analysis

Sandwich structures with composite facing skins have seen applications in variety of sectors including aerospace and automobile, owing to their high specific mechanical properties. However, there is a need to develop better damage tolerant sandwich structures since conventional composite facing skins exhibit low impact resistance in the transverse direction. Here, composite skin sandwich structures with three different impact resistant core materials were fabricated and tested both experimentally and numerically. Neat CFRP and 2024-T3 aluminum alloy sheets were also investigated. Cores utilizing impact resistant D3O® were found to have very favorable weight specific energy absorbing properties at higher impact velocities as compared to those made from Nomex® or Sorbothane® cores. Nonlinear finite element analysis was also performed using Hypermesh/LS-DYNA for 2024-T3 aluminum alloy sheet, neat CFRP and sandwich with Nomex® core with CFRP faceskins. Numerical vs. Experimental impact results were compared and comments regarding impact behavior of different candidate materials were made. CAI tests were performed for CFRP sandwich structures. Sandwiches with cores made out of D3O® and Sorbothane® showed more ductility when compared with Nomex® core sandwich composite.

1. Introduction

Carbon Fiber Reinforced Polymer (CFRP) structures are used extensively in aerospace, marine, civil, wind energy and recreational industries. These industries use composite materials in great quantities to manufacture their respective products like airplanes, pressure vessels, wind turbine blades, sporting equipment, etc. owing to their high stiffness and strength to weight ratio, excellent corrosion and fatigue resistance, low maintenance requirements, and ability to form into complex shaped parts. Aerospace industries, above all, reap great benefits from CFRP structures because they are relatively lower in weight compared to conventional aluminum alloy structures. Lower aircraft weight results in greater fuel efficiency, greater range and increase in profit margins for the airlines. In today's world where energy consumption is at an all-time high, CFRP structures can bring revolutionary solutions to many of these problems.

Recently, a new generation of commercial aircraft like the Boeing (Chicago, IL) B787 Dreamliner and Airbus (Toulouse, France) A350XWB have started using composite materials very extensively, Figure 1. CFRP structures have experienced immense usage on A350XWB, accounting for 53% of its structural weight (Airbus S.A.S., 2016). They are also widely used to construct primary structures of these new generation aircraft including the wing, fuselage and empennage (Faivre and Morteau, 2011) as shown in Figure 2. CFRP composites allow structural designers to design the fiber orientation as per the loading requirements for the particular structure. Thus, there can be a potential weight savings in the overall structure as unnecessary material weight is not added for non-load carrying parts. As aerospace and other industries increase the usage of CFRP, various shortcomings of CFRP structures will also be inherited. The proposed thesis research topic sheds the light

on mitigating some of the issues with using CFRP and further broadening the advantages and applications of CFRP based structures (monolithic and sandwich composites).

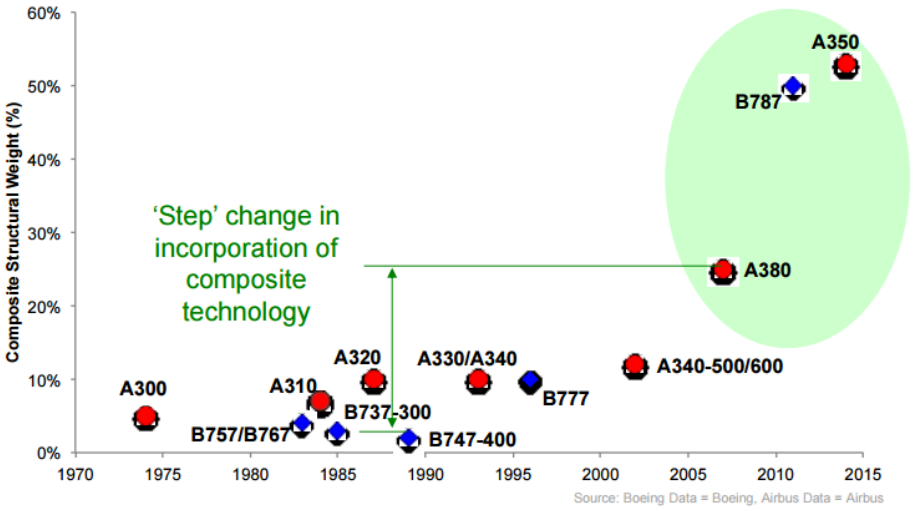

Figure 1. Increased usage of composite structures in next generation aircrafts.

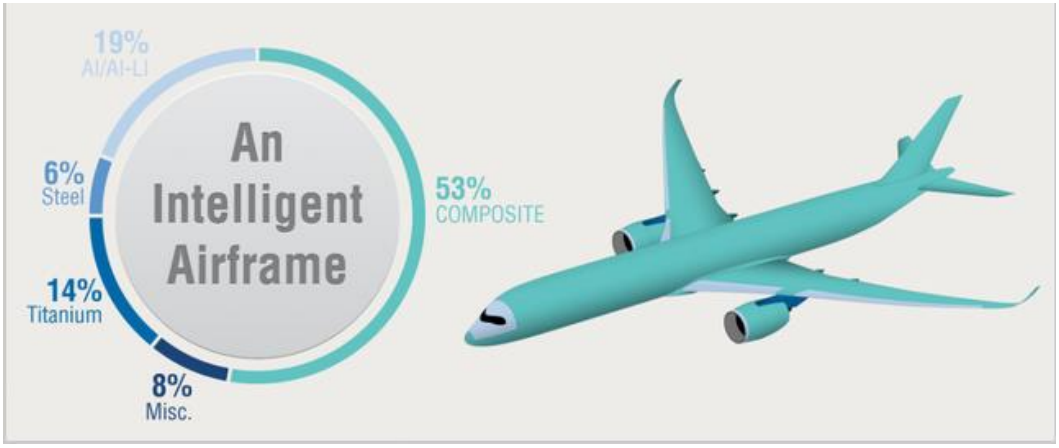

Figure 2. Composite usage in Airbus A350 XWB.

1.1 Problem Statement

Composite materials normally exhibit high stiffness and strength in the fiber direction while matrix dominated properties in the transverse direction, such as shear and impact resistance, are generally poor (Reid and Zhou, 2000). Moreover, through-the-thickness tensile strengths of CFRP laminates are typically lower than their isotropic

counterparts. For example, through-the-thickness tensile strength comparisons of 2024-T3 aluminum alloy sheet, 7075-T6 aluminum alloy sheet and CFRP laminates are shown in Figure 3 (Horton and McCarty, 1987).

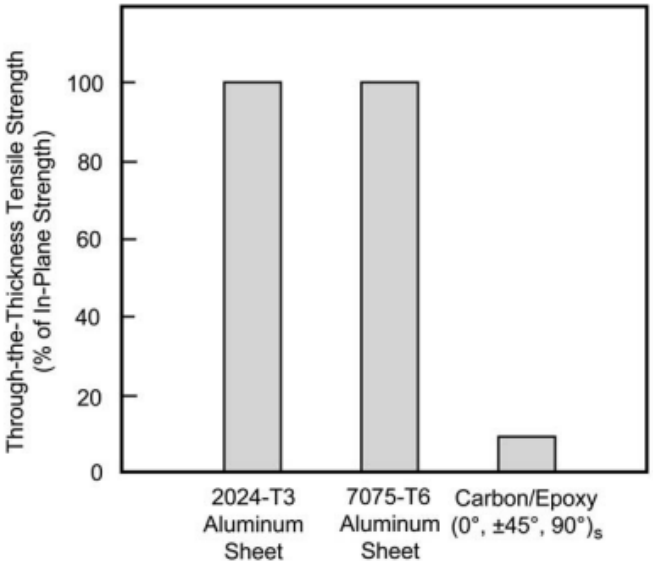

Figure 3. Through-the-thickness tensile strength comparison.

CFRP structures are often subjected to non-catastrophic impact damage during fabrication, maintenance or in-service operations (e.g., tool drops, bird strikes, hail, runway debris, ground support equipment, etc.). Around 80% of in-service aircraft damages are caused by impact strikes (Cook, Boulic, Harris, Bellamy and Irving, 2012). The areas of impact typically cover most of the locations of an aircraft's exterior structure (e.g., passengers and cargo doors, nose, fuselage and wings) as shown in Figure 4 (Faivre and Morteau, 2011). Impacts on composite structures can usually be characterized by one of two types: 1) High velocity impacts 2) Low velocity impacts. What is considered "high" as compared to "low" varies depending on agency and researcher. Here, low velocity impacts will be investigated with the goal of finding innovative solutions to improve

damage tolerance for non-catastrophic types of events. The high velocity impact response of composites and its damage tolerance will be considered out of scope for the current thesis research.

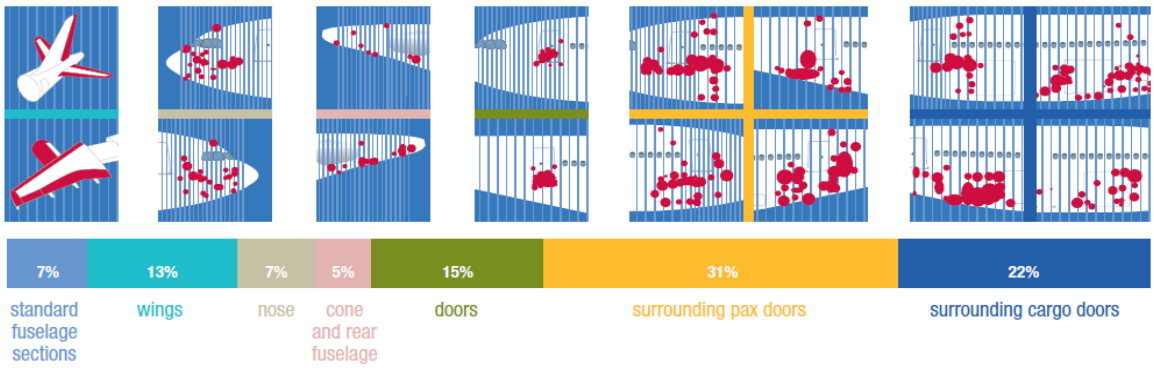

Figure 4. General locations of an impact on an AIRBUS aircraft.

Low-velocity impacts on CFRP composites structures often create Barely Visible Impact Damage (BVID), which can reduce residual mechanical properties, like compressive strength, immensely. BVID type damage can be a mixture of internal delamination driven largely by interlaminar shear and tension and lamina matrix cracking (Davis, G.A.O and Zhang, 1994). Such damage may be invisible from the exterior because of the higher permanent deformation resistance of CFRP while the subsurface may be damaged, Figure 5 (Waite, 2006). Thus, compared to metallic structures, detection of impact damage in CFRP is difficult as it does not readily show signs of a dent (Faivre and Morteau, 2011).

Figure 5. BVID example on Airbus A330 after horizontal stabilizer accident.

It has been shown that the compressive strength of CFRP laminates drops significantly after impact because of the multiple failure modes. For example, compressive strengths of graphite fiber based composite structures have shown reduction of as much as 60% after sustaining low velocity impact (Dobyns and Porter, 1981). Because of unpredictability of compression after impact (CAI) strengths, current design strategy has lower after impact allowable strains, often as low as 0.3%, while the undamaged composite can withstand strains of order 1% (Davis et al., 1994). Delamination created in the laminate during low velocity impact is a critical mode of failure that helps induce reduction in compressive strength of the laminate. During the compression, delamination often creates a void between laminate causing local buckling of the sub-laminates (Nettles, 2010). This problem is not seen in tension after impact as the delamination simply closes-up and not much change is seen in laminate tensile strength. Figure 6 (Nettles, 2010) shows the sub-laminates created after impact as well as their buckling during compression.

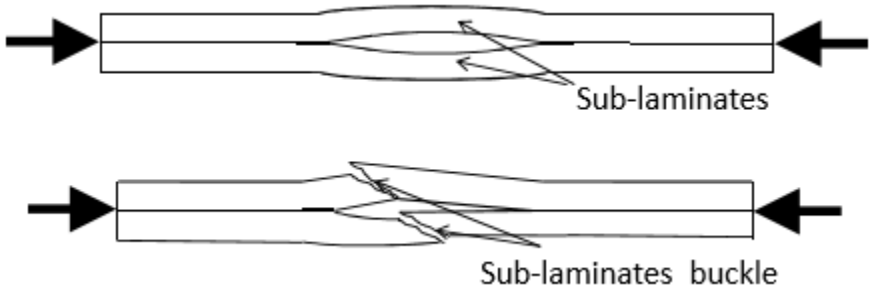

Figure 6. Sub-laminates (top) and buckled sub-laminates in compression (bottom).

Delamination is found to be initiated at a certain impact energy threshold with final delamination size increasing linearly with increasing impact energy (Abrate, 1998). Damage generated by impact depends on the composite lay-up, as well as velocity, shape, material and shape of the indenter. In addition, boundary conditions of the impacted specimen also affect the impact damage (Liu, 1988). The delamination pattern also depends on the lay-up orientation angle of the plies as shown in Figure 7 (Abrate, 1998). Research has also suggested that for low velocity impacts of the same energy level, all other governing impact behavior parameters kept constant, impact cases involving low masses at high velocities created more delamination damage and lower CAI strengths compared to impacts involving high mass, low velocity scenarios (Starnes, Dickson and Rouse, 1984). For a specific impact energy, stiffness of the indenter also plays a significant role in damage induced to composites. A stiffer impactor will generate more damage for a given impact energy level compared to a more elastic (or pliable) impactor.

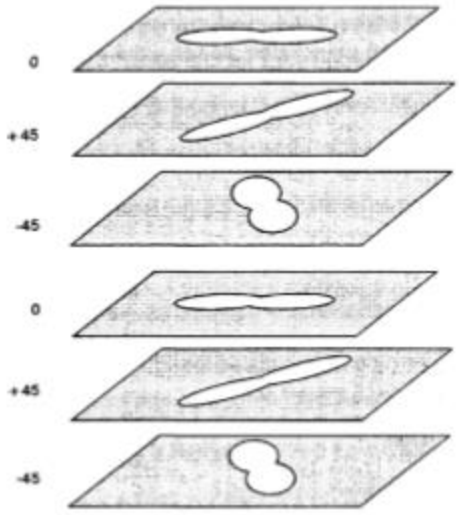

Figure 7. Delamination orientation dependence on ply angles of a laminate.

Simple visual inspection in composites cannot be relied upon as a means of Non-Destructive Evaluation (NDE), unlike metallic counterparts. If the BVID caused by low-velocity impact goes undetected but with subsurface delamination's, the composite structure may not be able to withstand its design limit load and its ultimate load carrying capacity maybe reduced (Christoforou and A.P., 2001). Furthermore, late detection of these subsurface delamination's can increase the maintenance costs as the entire composite component may have to be replaced because of expanded damage over use and time. Therefore, there is a long felt need to develop better damage tolerant composite structures. A more damage tolerant structure would give maintenance crew a greater window of opportunity to detect the damage and in turn may also increase flight cycles of an impact damaged CFRP structure.

1.2 Research Purpose

The purpose of this research is to investigate the effect of low-velocity impacts on CFRP and isotropic structures. Moreover, new types of CFRP based sandwich structures with energy absorbing cores will be investigated for their energy absorbing effectiveness. Overall, this research seeks to develop a lighter and thinner alternative to conventionally used honeycomb core sandwich structures (e.g., with Nomex® and/or Al alloy cores) for energy absorbing purposes. The proposed sandwich structures may be proven to be more damage tolerant compared to Nomex® honeycomb core structures and more easily deployed in existing CFRP structures to improve its damage tolerance and mitigate the effects of damage due to low-velocity impact loadings. The material configurations proposed here will be relatively less expensive and less technologically demanding compared to conventional impact resisting techniques and approaches. Practicality and fast adoption of the proposed structures are key motives of this work. The new types of sandwich structures with energy absorbing cores and CFRP facing skins will be compared with isotropic and neat CFRP laminate for their weight and energy absorbing characteristics.

Initially, 2024-T3 aluminum alloy sheet and CFRP laminates will be evaluated numerically and experimentally under low-velocity impact loading. After confirming the validity of numerical modelling, experiments will be conducted for different proposed sandwich coupons. Impact, weight and energy absorption characteristics of the different proposed sandwich structures will also be compared experimentally and numerically to Nomex® honeycomb sandwich structure.

Lastly, CAI strength tests will be conducted on impacted and neat samples to evaluate the drop in compressive strength after impact of the candidate materials. Thus, by using experimental and numerical methods, the research hopes to uncover new sandwich structure configurations that increase the damage tolerance of CFRP based sandwich structures while decreasing their weight and thickness.

1.3 Research Significance

The proposed thesis research is of unique significance to aerospace and other industries (especially automobile) whose products often experience low velocity impact loadings, requiring significant impact resistance and damage tolerance for their safe use and certifications. Thus, it is the multidisciplinary aspect of this research that makes the proposed problem solution amenable to multidisciplinary methods. Eventually, the research seeks to enable commercial development of energy absorbing composite sandwich structures with decreased overall weight and thickness.

2. Prior Investigations

The field of composite damage tolerance has seen many investigations over the past few years seeking ways of improving the impact resistance and residual strength of composite structures. Glass Fiber Reinforced Polymer (GFRP) composite structures have proved superior to CFRP in terms of sustaining mechanical performance after being damaged by impacts. This can partly be explained by GFRP's lower modulus and weaker interface between the glass fibers and matrix (Davies et al., 1994). The strain to failure of most glass fibers is also higher than carbon fibers. However, the compressive strength of GFRP is considered low for many aerospace applications because of their flexibility. Thus their superior damage tolerance performance is not of significant importance in the aerospace industry as compared to CFRP. Furthermore, hybrid composite structures involving stiff carbon, flexible glass and intermediate aramid fibers can offer an acceptable compromise (Dorey, Sigerty, Stellbrink and Hart, 1987) and (Marom, Drukker, Weinberg and Banbaji, 1986). Usage of tougher resins, particularly thermo-plastic matrix (e.g., polyether ether ketone) with high strain fibers have also been found to improve damage tolerance of composite structures (Davies and Robinson, 1992).

A variety of methods have been investigated to improve the damage tolerance of composite structures and to arrest delamination created by impact loading conditions. There have been reviews of most of the current methods used to improve impact damage tolerance in stringer-stiffened aerospace composite components (Greenhalgh and Hiley, 2003). The methods include tougher matrix systems, 2D and 3D woven materials, stitching and z-pinning, selective interlayers, protective surface layers, and hybrid laminates. However, most of these methods do not allow for refurbishing the damaged structures, they

are also expensive and sometimes carry weight penalties with them. Hence there is a need to develop a cost effective and lightweight solution for the problem.

Studies have been performed to improve the damage tolerance of the composite sandwich structures. For example, foam filled sandwich structures with variety of different facing skins and analysis of impact damage tolerance with CAI strength have been performed (Yang et al., 2015). It was found that in the sandwich with carbon fiber composite facing skins, matrix cracking, fiber breaking, foam cracking and debonding were the main failure modes during the impact. It was also found that sandwich with glass fiber composite facing skins showed the lowest rate of decline in compression strength while sandwich with carbon fiber composite facing skins showed highest rate of decline. Studies were also made where facing skins were developed from a hybrid of carbon and glass fiber composite facing skins. Damage tolerance of the sandwich was improved through this approach as the rate of compressive strength was dropped. However, overall compressive strength of undamaged hybrid sandwich structure was lower than the undamaged composite sandwich with carbon fiber facing skins.

Various researchers have investigated the influence of fiber staking sequence, different foam materials and temperature on impact tolerance properties of composite sandwich structures. Some have suggested the usage of rubber between layered steel and composite in order to absorb energy and decrease the interfacial damage in hybrid composite structure (Sarlin et al., 2015). It was found that the hybrid composite with 1.5 mm of rubber layer between steel and composite showed a reduction of 50% in the damage area caused by impact damage. Figure 8 shows the impacted hybrid specimen (Sarlin et al., 2015).

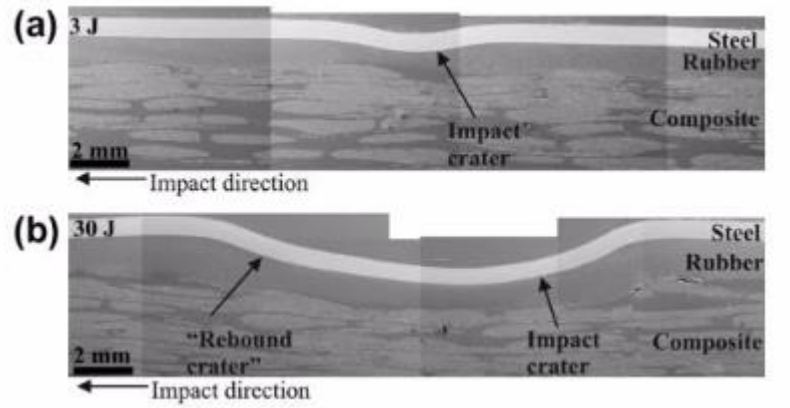

Figure 8. Steel-Rubber-Composite hybrid material after low velocity impacts.

3. Experimental Approach

The experimental approach investigated here involves a variety of experiments designed to obtain the low velocity impact response of the composite candidate facing skins and energy absorbing sandwich structures. Candidate coupon structures were fabricated inside the Embry-Riddle Composites Lab using a hot press molding technique. Drop weight tests were conducted at low velocities in order to obtain Force vs. Time, Energy vs. Time and Displacement vs. Time impact characteristics. Energy vs. Time results were normalized by weight and thickness of the impacted coupons in order to compare weight and thickness effects on energy absorption. Moreover, CAI tests on impacted and neat samples help determine the increase/decrease in residual compressive strength of the candidate materials.

3.1 Coupon Fabrication

Coupons tested for low velocity impacts included 2024-T3 aluminum alloy sheets, 14 layer neat CFRP composite laminated and sandwich structures with one of a Sorbothane®, Nomex® or D3O® core each with 7 layers of CFRP acting as top/bottom facing skins. Besides that, the neat and sandwich structures were tested for CAI compressive strength. Specific details of the materials are found later.

3.1.1 2024-T3 Aluminum Alloy

2024-T3 aluminum alloy sheet was acquired from Kaiser Aluminum (Spokane, WA). The thickness of the sheet was 0.4 mm and test coupons weighted 10 g when trimmed to 101.6 mm x 152.4 mm (4 x 6 in) dimensions. Nine 2024-T3 aluminum alloy coupons were used to conduct the experiments.

3.1.2 Neat CFRP Prepreg

The neat CFRP prepreg material was a 2 x 2 twill weave obtained from ACP Composites (Livermore, CA), see Appendix A for specific details. This is a room temperature storage item. Even so, a freezer was used to further extend the lifetime of the prepreg. Two types of CFRP samples were fabricated, one type with 7 layers of composite and another with 14 layers. The neat CFRP coupons made from them were denoted as $(CF)_7$ and $(CF)_{14}$ respectively. Fiber orientations of 0/90 twill were kept the same during the layup building. This means that fibers with 0^o orientation were parallel to all 0^o fibers and fibers with 90^o orientation were parallel to all 90^o fibers throughout the thickness. The hot press aluminum mold plate was initially sanded to make sure there was no residual contaminants and was cleaned with acetone afterwards. Moreover, Fiberglass 1153 FibRelease® release agent (Fiber Glast Development Corporation, Brookville, OH) was applied before stacking composite layers on the aluminum plate mold. This was the done for the ease of removal of the cured composite plates at the end of hot press molding process. Peel ply, breather, vacuum bag (Fiber Glast Development Corporation, Brookville, OH) and aluminum foil (Reynolds Metals Company, Lincolnshire, IL) were applied on top of the composite layup for uniform pressure distribution and excess epoxy absorption purposes.

CFRP coupons were fabricated using a Genesis series Wabash Compression Press (Wabash, IN), Figure 9. Prepregs were cured at 154^oC (310^oF) for 70 min as mandated by the manufacturer and to ensure the quality of fabrication. A uniform pressure resulting from a load of 13,350 N (1.5 Ton) was applied throughout the hot press molding process. Fabricated CFRP materials were then trimmed with a Leco (St. Joseph, MI) MSX 255

Benchtop Sectioning Machine, Figure 9. Neat CFRP coupons were trimmed to get dimensions of 101.6 mm x 152.4 mm (4 x 6 in) to comply with ASTM D3763 (American Society For Testing And Materials, West Conshohocken, PA) impact test standards.

Figure 9. Wabash Compression Press (left) and Leco MSX255 Benchtop Sectioning Machine (right).

3.1.3 Cores With CFRP Faceskins

Standard cell Nomex® honeycomb with cell size of 4.8 mm (3/16 in) and thickness of 6.4 mm (1/4 in) was acquired from ACP Composites. Sorbothane® (Kent, OH) with Durometer 30 and thickness of 5 mm (approx. 3/16 in) was also obtained. D3O® recoil pads with thickness of 4.0 mm were obtained from Musto Ocean Engineered® (Essex, UK). Nomex®, Sorbothane® and D3O® were cut to the dimensions of 101.6 mm x 152.4 mm (4 x 6 in) to match with the CFRP facing skin dimensions. Each of the three types of cores were attached to the 7 layered neat CFRP facing skins using Lord® (Cary, NC) 7542A/B

Urethane Adhesive (two component). To adhere, an appropriate mixing tip/gun was used to apply 6 thin standardized strips in one direction and 5 in the other direction (to form a crossing pattern) on the dry sanded CFRP sides that would eventually face the core. A wood mixing stick was then used to smooth the adhesive uniformly. Moreover, when adhering to the cores, masking tape was used on the perimeter of the facing skin and core assemblies in order to restrict any relative movement between them during vacuum bagging. Each entire assembly was vacuum bagged at room temperature and allowed to cure for 24 hr under vacuum. A rotary vane pump capable of 10^{-3} Torr range was used to achieve vacuum. Figure 10 below shows the initial adhesive pattern on the CFRP facing skins as well as the fabrication sequence for the composite sandwich structures along with cross-sectional views of each different sandwich structure.

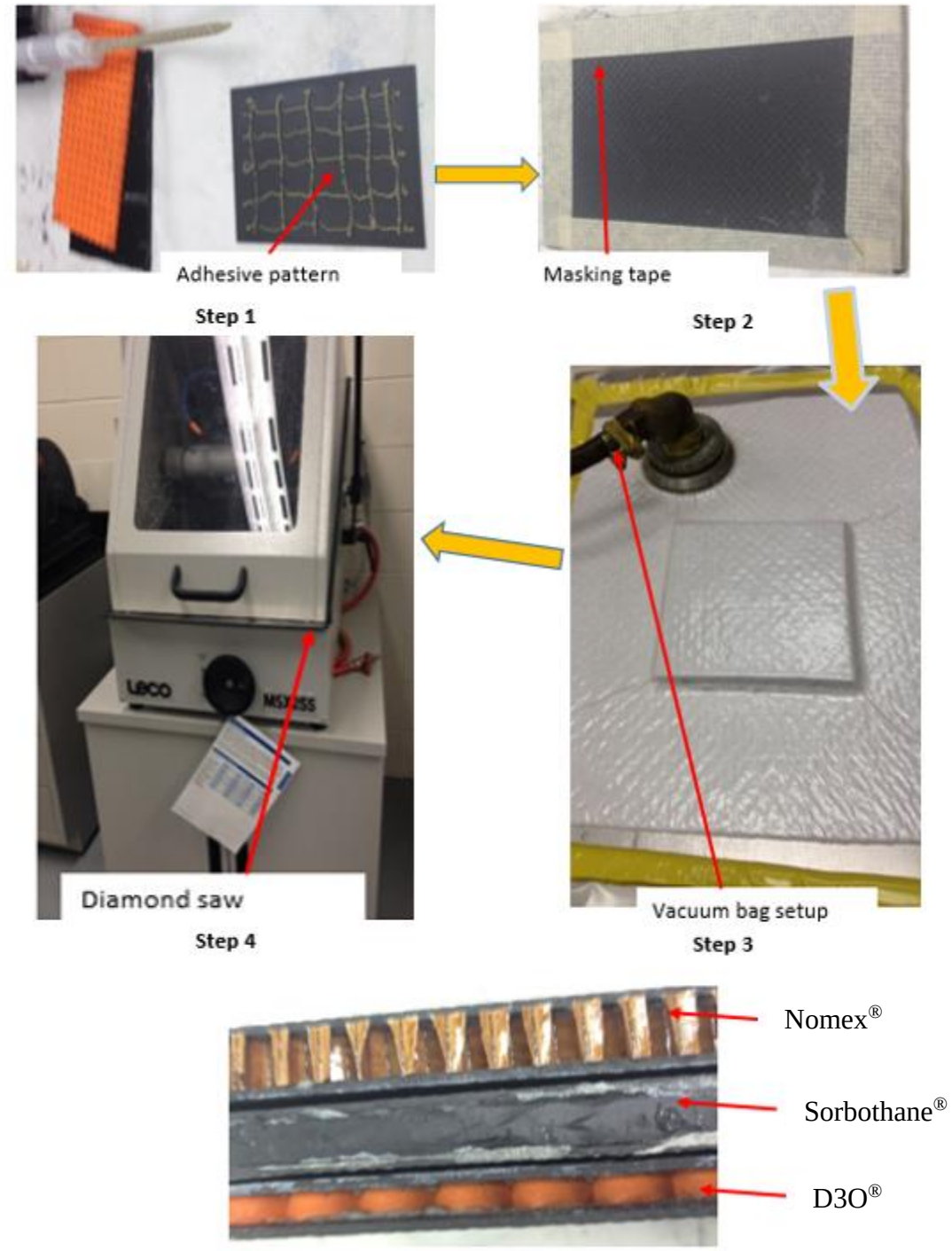

Figure 10. Composite sandwich fabrication process and final cross-sections of fabricated coupons.

3.2 Drop-Weight Impact Testing

Drop-weight impact testing is usually performed to measure the impact strength and energy absorption characteristics of a material. An Instron (Norwood, MA) 9250 HV Impact Test Instrument was used following ASTM D7136/D7136M standards. It was equipped with a 12.7 mm (0.5 in) hemispherical steel indenter, adjustable crosshead and drop weights, pneumatic clamp and rebound brake, 22.2 kN strain gauge instrumented impact tup and Impulse DAQ system and Controller - Version: 3.6.76. An impact mass of 6.64 kg was used. Low speed impacts at velocities ranging from 1.0 m/s to 3.5 m/s were performed on all test specimens; 2024-T3 aluminum alloy sheets, neat CFRP and the three different types of CFRP skin sandwich structures. Figure 11 below shows the drop-weight tower used to perform impact tests. Also, the hemispherical indenter and clamp fixture are shown in detail for clearer understanding. The clamp fixture created a nearly fixed boundary condition at the edges of the test specimen(s). These boundary conditions are created by pneumatic clamping device. The fixture is clamped utilizing 551 - 620 kPa (80 - 90 psi) shop air for the impact experiments. Rebound brakes were also activated to avoid unwanted dual impacts (“the bounce”) on the specimen(s). All experimental results reported in this research involved a single impact event as no second rebound strike was allowed. Various calibration tests were performed on simple cardboard sacrificial samples to make sure all systems and data acquisition were working properly. The impact mass was measured independently using a small digital mass scale for weight confirmation. Impact data was set to be recorded over an event duration range of 15 ms. The maximum impact force was set at about the mid-range of the 22.2 kN tup.

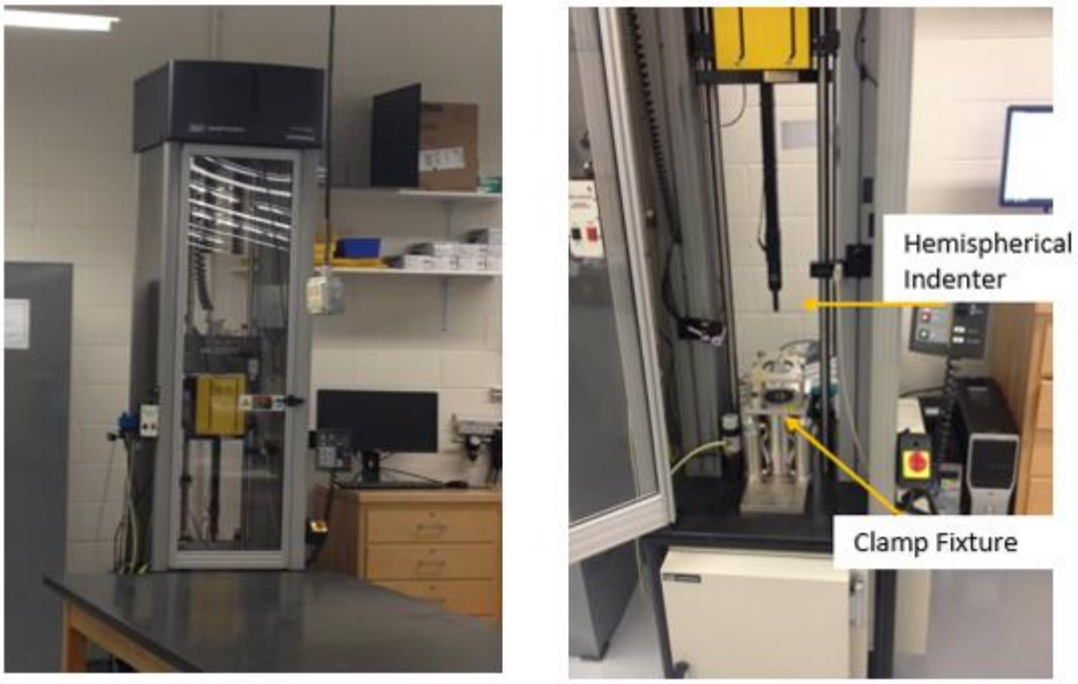

Figure 11. Instron 9250 HV Impact Test Instrument.

3.3 Experimental Results

3.3.1 2024-T3 Aluminum Alloy Sheet

Impact tests were performed on 2024-T3 aluminum alloy coupons with dimensions of 101.6 mm x 152.4 mm (4 x 6 in) at impact velocities of 1.0 m/s, 1.25 m/s, 1.5 m/s, 3.0 m/s and 3.5 m/s in order to observe the strain rate effect (if any) and to notice changes of Displacement, Force and Energy absorbed vs. time curves with changes in impact velocity. Two tests were performed at each velocity (except 3.5 m/s which was just one test). Figure 12 below depicts the impacted coupons with velocity increasing from left to right.

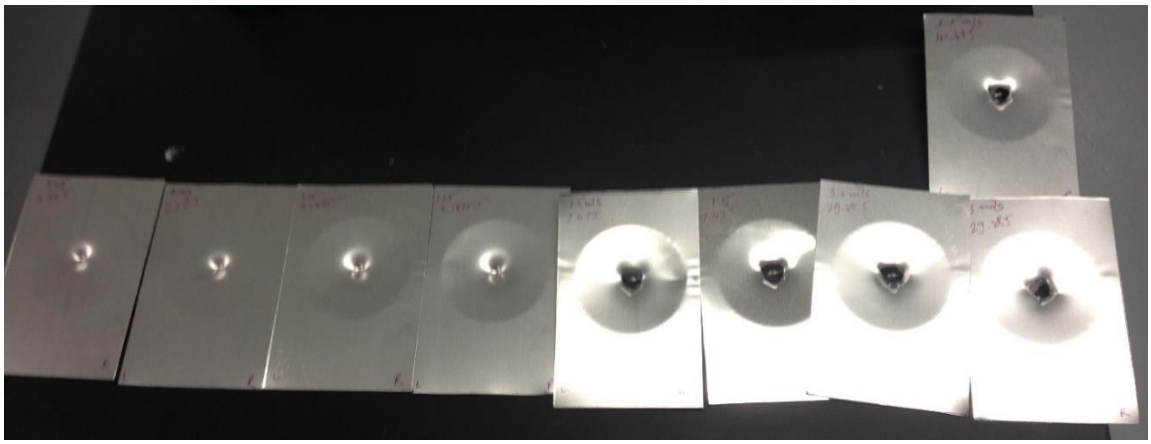

Figure 12. Post impacted 2024-T3 aluminum alloy sheet coupons.

Figure 13, 14 and 15 below show the Displacement (mm), Energy (J) and Force (kN) curves vs. Time (ms) respectively for the prescribed impact velocities. As seen below in the Force vs. Time curve(s), Figure 15, a sudden drop in Force was observed at 1.5, 3.0 and 3.5 m/s suggesting total penetration of the impactor through the specimen.

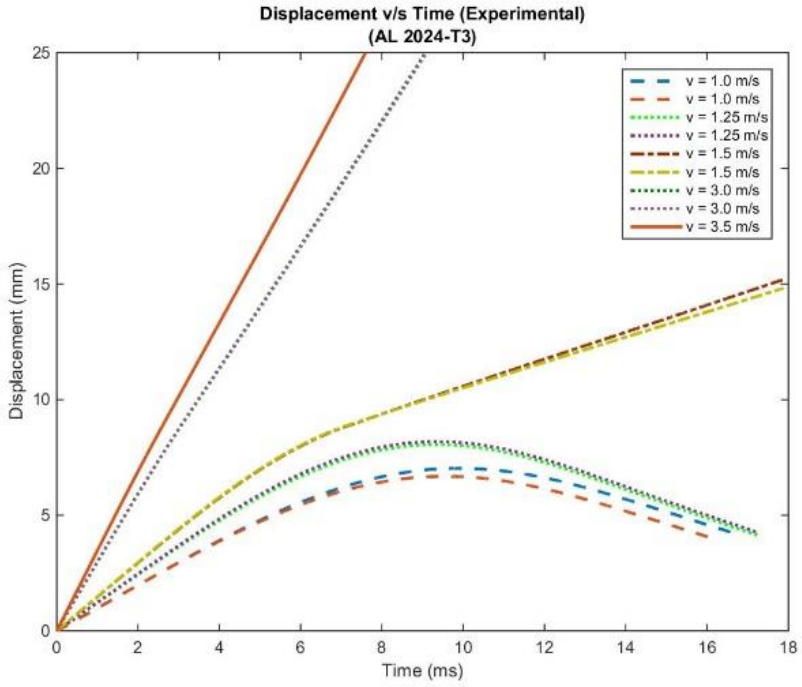

Figure 13. Displacement (mm) vs. Time (ms) curves for 2024-T3 aluminum alloy sheet at varying impact velocities.

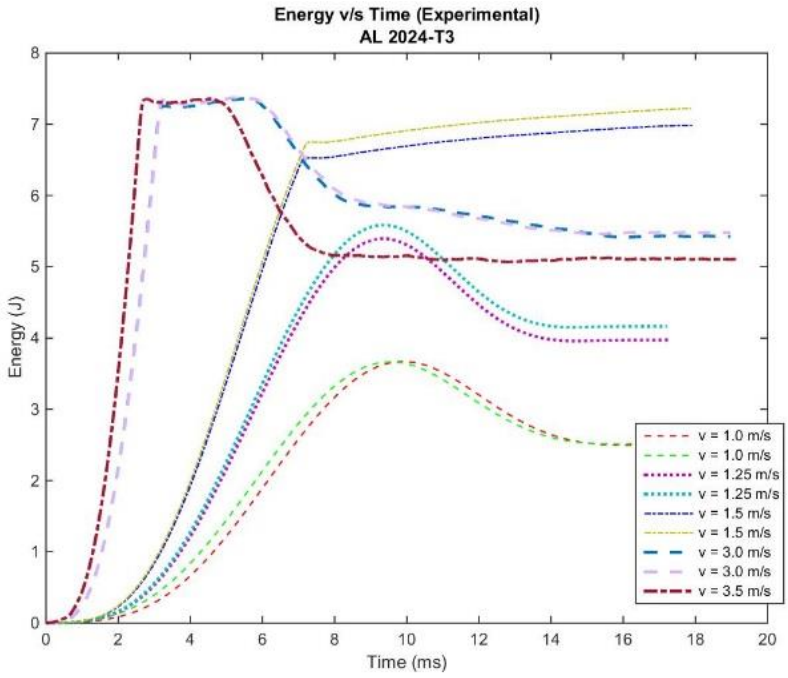

Figure 14. Energy (J) vs. Time (ms) curves for 2024-T3 aluminum alloy sheet at varying impact velocities.

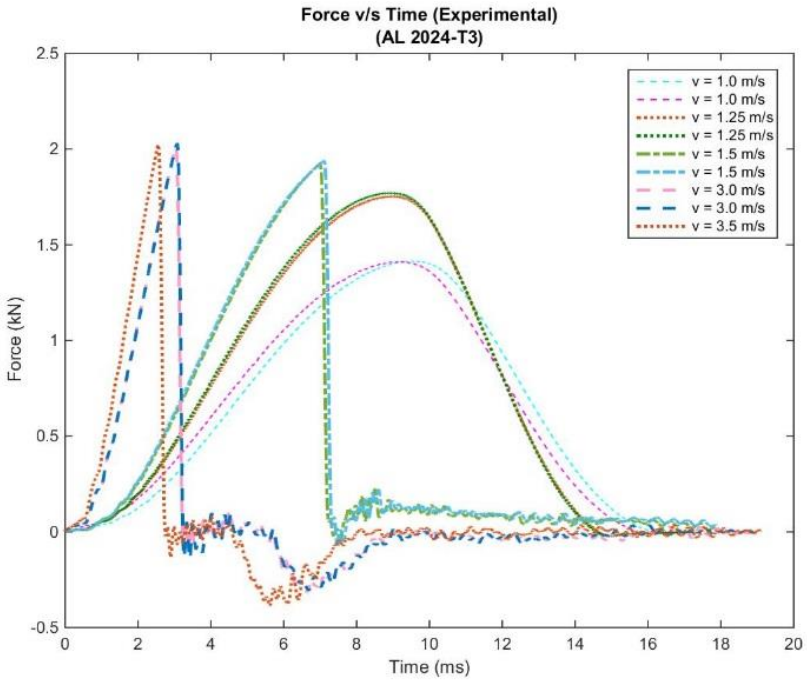

Figure 15. Force (kN) vs. Time (ms) curves for 2024-T3 aluminum alloy sheet at varying impact velocities.

3.3.2 Neat CFRP

Impact tests were performed on two $(CF)_{14}$ coupons with dimensions of 101.6 mm x 152.4 mm (4 x 6 in) for impact velocities of 1.0 m/s and 1.25 m/s in order to observe the strain rate effect (if any) and to notice the change of Displacement, Force and Energy absorbed curves with the change in impact velocities. Note that total penetration occurred at velocities of 1.5 m/s and greater but these results were neglected since this is well beyond BVID. Figure 16, 17 and 18 below show the comparison of Displacement (mm), Energy (J) and Force (kN) curves vs. Time (ms) respectively for the prescribed impact velocities for 2024-T3 aluminum alloy and $(CF)_{14}$ coupons. As seen in the Force vs. Time curve for $(CF)_{14}$, spikes for Force curves changing with respect of time are seen. This indicates the complex nature of failure modes occurring within the neat CFRP sample during the impact loading. An initial drop in force is suggesting onset of delamination in $(CF)_{14}$ while the upper (and final) force drop suggests the beginning of fiber failures. In general, failure modes due to impact loading may include fiber breakage, fiber/matrix debonding, fiber kinking and delamination between adjacent plies. Also, the peak force (acceleration pulse) for the $(CF)_{14}$ is higher compared to its isotropic counterpart 2024-T3 owing to the higher stiffness property of the composite laminate. As observed from the below Displacement vs. Time curve, we see that 2024-T3 deflected more then $(CF)_{14}$ confirming with the more ductile behavior of isotropic materials compared to carbon fiber composite laminates. As seen in Energy vs. Time curve, even though the energy peek by $(CF)_{14}$ was obtained earlier in time (stiff response) and was similar in magnitude with energy peak from 2024-T3, the rebounded energy (absorbed energy) of $(CF)_{14}$ was lower than that of 2024-T3. Rebounded

energy (absorbed energy) of the 2024-T3 coupon is showed in Figure 17. Similarly, absorbed energy can be evaluated for composite laminates from the Figure 17 plot.

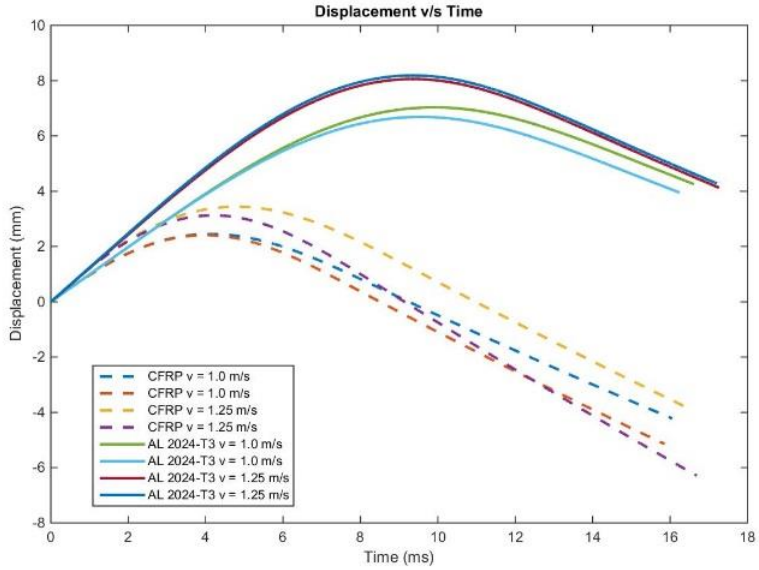

Figure 16. Displacement (mm) vs. Time (ms) curves for $(CF)_{14}$ and 2024-T3 at varying impact velocities.

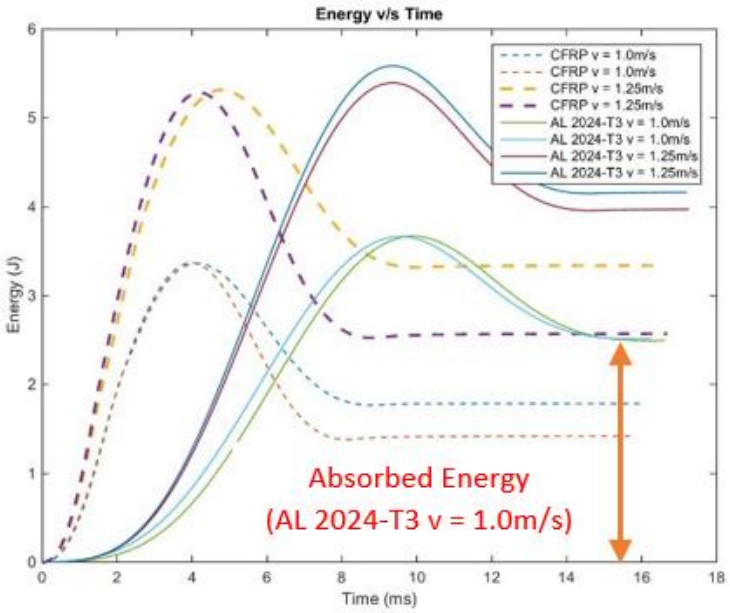

Figure 17. Energy (J) v/s Time (ms) curves for $(CF)_{14}$ and 2024-T3 at varying impact velocities.

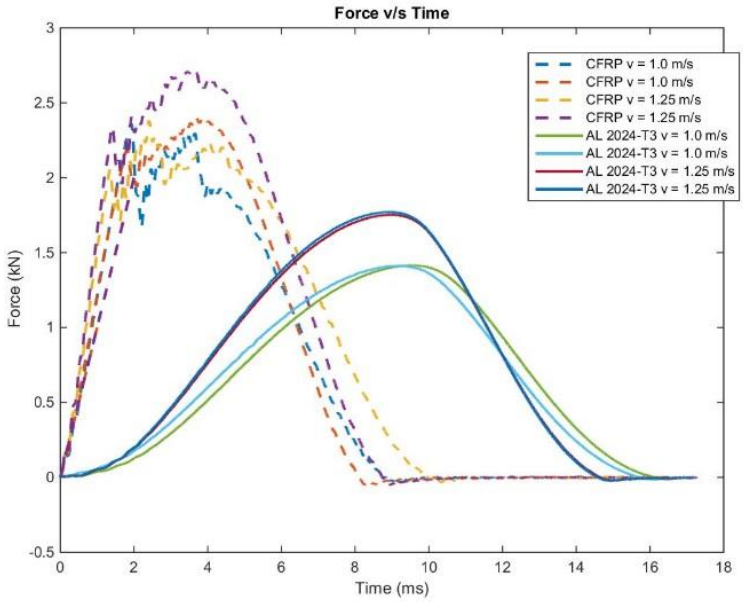

Figure 18. Force (kN) vs. Time (ms) curves for $(CF)_{14}$ and 2024-T3 at varying impact velocities.

3.3.3 Sandwich Structure With CFRP Faceskins

Impact tests were also performed on CFRP sandwich structure containing D3O®, Sorbothane® and Nomex® honeycomb as their cores respectively with dimensions of 101.6 mm x 152.4 mm (4 x 6 in). The impact velocities were 1.0 m/s and 1.25 m/s in order to observe the strain rate effect and to notice the change of Displacement, Force and Energy absorbed curves with the change in impact velocities. Fig. 19, 20 and 21 below show the comparison of Displacement (mm), Specific Energy (J/g) and Force (kN) curves vs. Time (ms) respectively for the prescribed impact velocities between $(CF)_{14}$ coupons and CFRP sandwich structures containing D3O®, Sorbothane® and Nomex® honeycomb cores respectively. It can be observed from the Force vs. Time curve response that the force peak (acceleration pulse) for the neat $(CF)_{14}$ coupon is higher than the CFRP sandwich structure owing to its stiffer response to impact loading. Moreover, from the Displacement vs. Time

curve, we can conclude that the CFRP sandwich structure deformed more than neat CFRP thereby proving its more ductile nature. Furthermore, specific energy with respect to time was computed with the plan of obtaining the most favorable lightweight energy absorbing sandwich material configuration. From the Specific Energy vs. Time curve, it can be concluded that CFRP facing skins with Nomex honeycomb core had higher specific energy absorbed then CFRP sandwich coupons with D3O® or Sorbothane® cores. Thus, at the lowest velocities tested (1.0 m/s and 1.25 m/s), validity and feasibility of using D3O® and Sorbothane® as a core material was not proven as compared to conventionally used Nomex® honeycomb cores for energy absorbing reasons. However, at higher velocities the D3O® core results are much more encouraging.

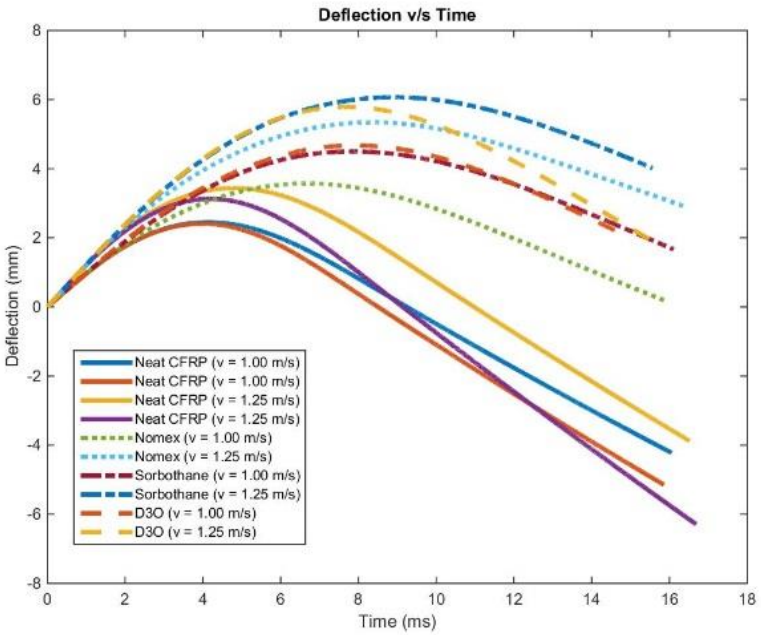

Figure 19. Displacement (mm) vs. Time (ms) curves for $(CF)_{14}$ and CFRP sandwich structures at different impact velocities.

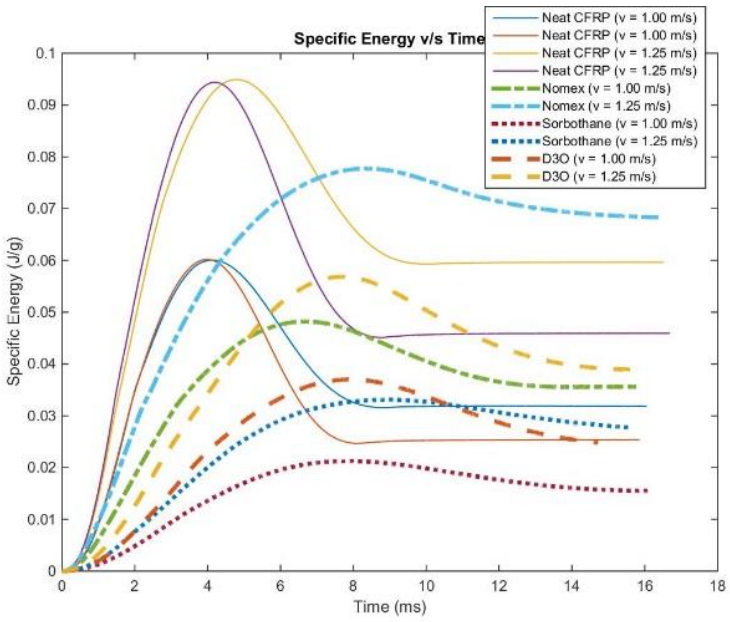

Figure 20. Specific Energy (J/g) vs. Time (ms) curves for $(CF)_{14}$ and CFRP sandwich structures at different impact velocities.

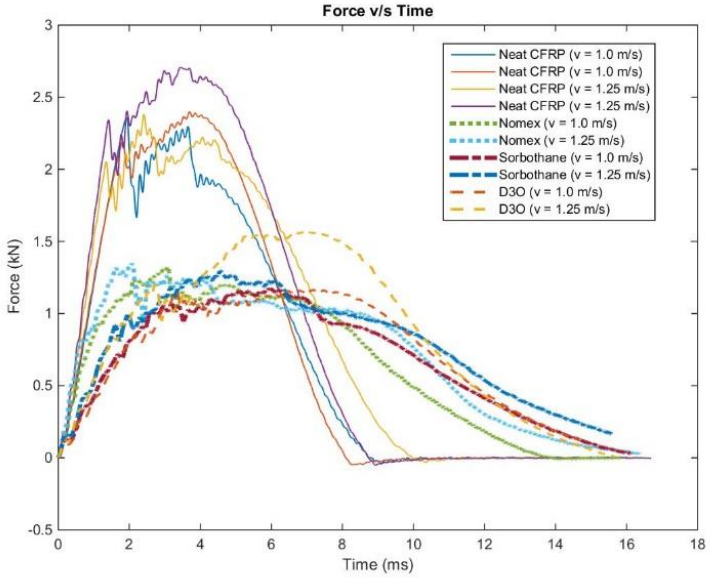

Figure 21. Force (kN) vs. Time (ms) curves for $(CF)_{14}$ and CFRP sandwich structures at different impact velocities.

Impact tests were also performed on all the three samples with CFRP faceskins and Nomex®, Sorbothane® and D3O® cores respectively at the relatively higher impact speed

of 3.0 m/s. It was believed that the strain rate sensitivity of the D3O® cores could be influential in energy absorbing capacity of the sandwich structure. Figures 22 and 23 show the specific energy (J/g) and energy absorbed per thickness (J/mm) for the three sandwich cores with CFRP faceskins impacted at 3.0 m/s. As seen in Figure 22, the sandwich with D3O® core absorbed almost same amount of specific energy as the sandwich with the Nomex® core. Sandwiches with the Sorbothane® core absorbed less amount of specific energy because of their apparent lack of strain rate sensitivity at higher impact speeds as well as their heavier weight. Thus, the hypothesis made for sandwiches with D3O® cores seems to be working at relatively higher impact speeds. This can result in the development of relatively lightweight structures subjected to relatively higher impact speeds (> 3.0 m/s). Moreover, as seen in Figure 23, D3O® cores also allowed for a thinner structure as evident in Energy Per Thickness (J/mm) vs. Time (ms) curves for all the sandwich configurations. This characteristics can help engineers design thinner and more compact sandwich structures.

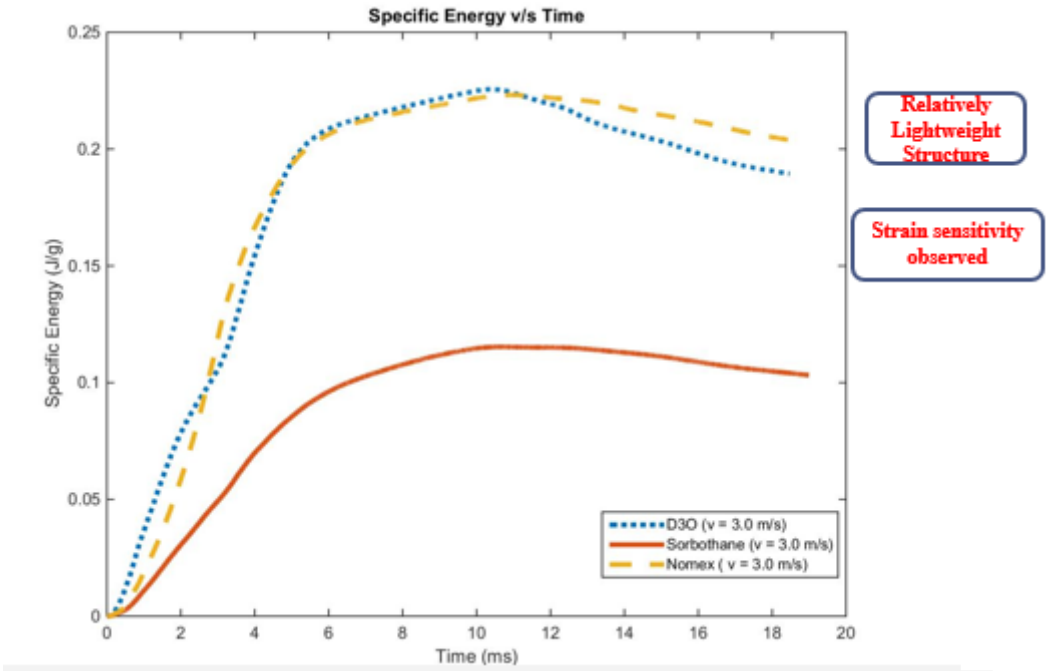

Figure 22. Specific Energy (J/g) vs. Time (ms) for the sandwiches impacted at 3.0 m/s impact velocity.

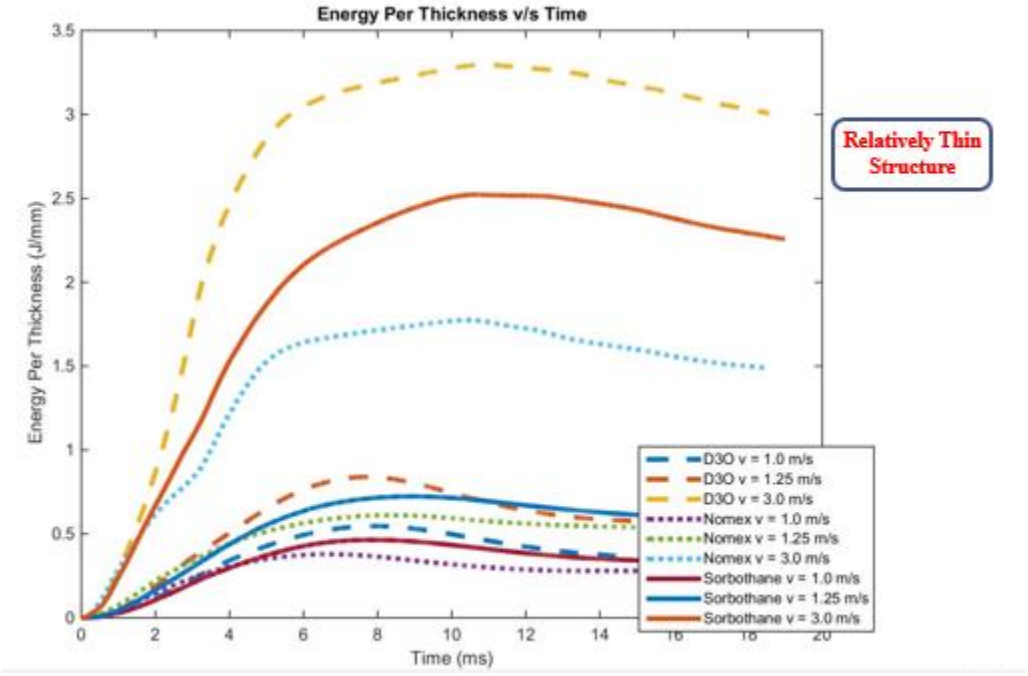

Figure 23. Energy Per Thickness (J/mm) vs. Time (ms) for the sandwiches impacted at 3.0 m/s impact velocity.

The sudden improved performance of sandwiches with D3O® cores is believed to be because of its superior strain rate sensitivity property. D3O® contains free molecules in its steady state (D3O® Impact Solutions, 2016). When this material experiences an impact, its molecules interlock to dissipate and absorb the impact energy. The material then quickly returns to its original flexible state. It is believed that D3O® sandwiched between CFRP plates will be more flexible and accommodating than a CFRP only composite plate. As a result, more energy is expected to be absorbed by a D3O® core sandwich structure than the CFRP plates with Nomex® and Sorbothane® cores. Figure 24 below shows a picture of the D3O® mesh and a schematic of the interlocking mechanisms (D3O® Impact Solutions, 2016).

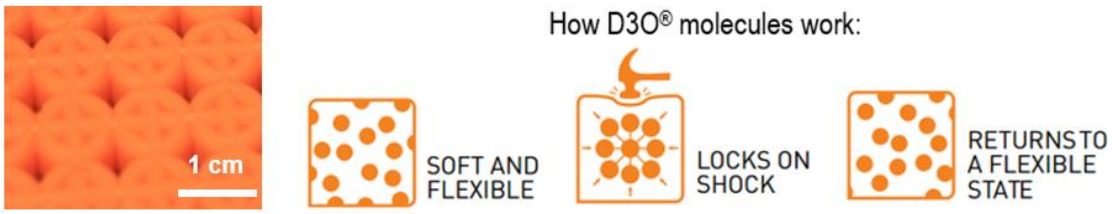

Figure 24. D3O® mesh with interlocking mechanism schematic. The thickness of the mesh is 0.40 cm.

A single circular unit with cross hatch from the D3O® foam pad was sliced and then gold sputter coated using a Cressington 108 Sputter Coater (Cressington Scientific Instruments, Watford, England). The coater picture is shown in below Figure 26. The sputter coated D3O® sample was then analyzed using a scanning electron microscope (SEM) to measure and characterize its interior foam structure. A FEI Quanta 650 with a Bruker EDX system (Hillsboro, Oregon), Figure 25, at ERAU was used. This SEM can

magnify up to 1,000,000x at a resolution of 3 nm, and also has a low-vacuum setting in order to image non-conductive samples. The D3O® sample was analyzed at 50x and 400x magnifications as seen in Figure 27 and Figure 28. It was found the foam indeed contains many tiny closed cells which are believed to collapse under impact loading to absorb energy.

Figure 25. FEI Quanta 650 with a Bruker EDX system at ERAU SEM Laboratory.

Figure 26. Cressington 108 Sputter Coater at ERAU SEM Laboratory.

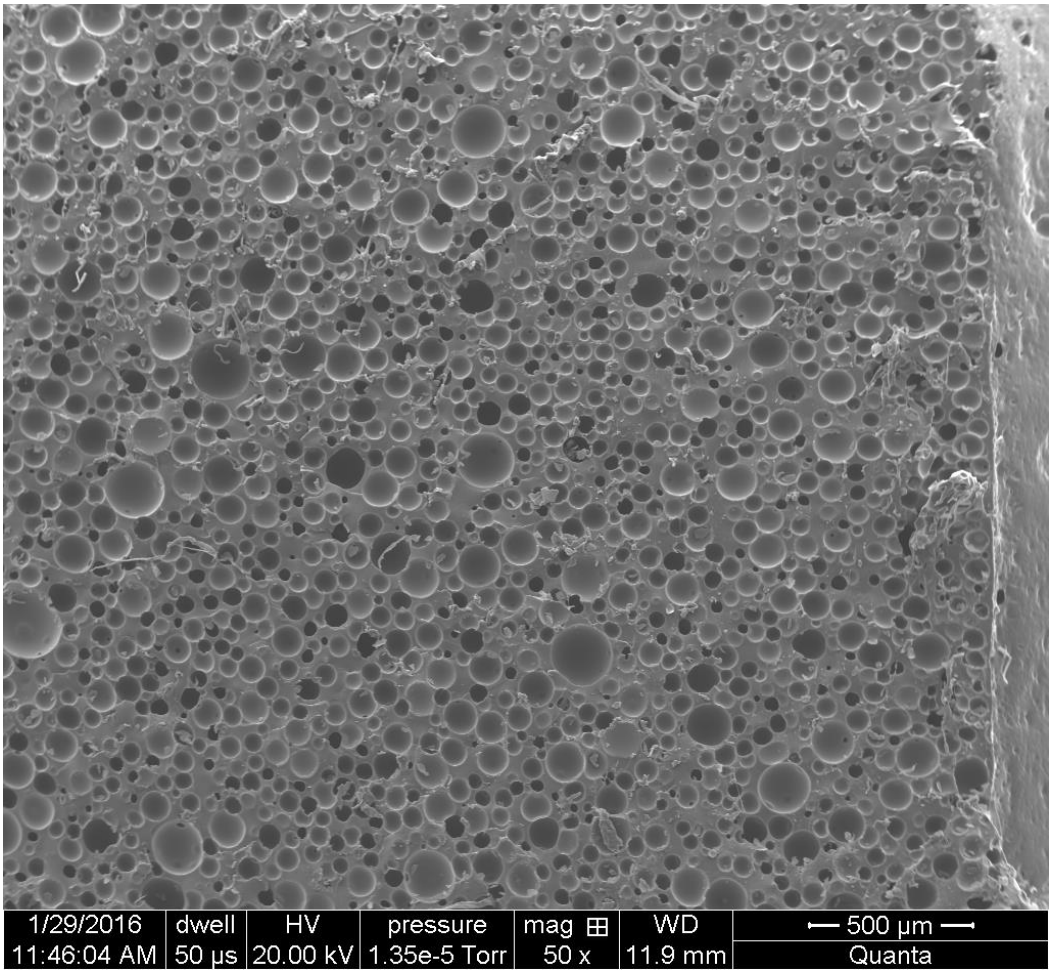

Figure 27. 50x SEM magnification image of D3O® sample.

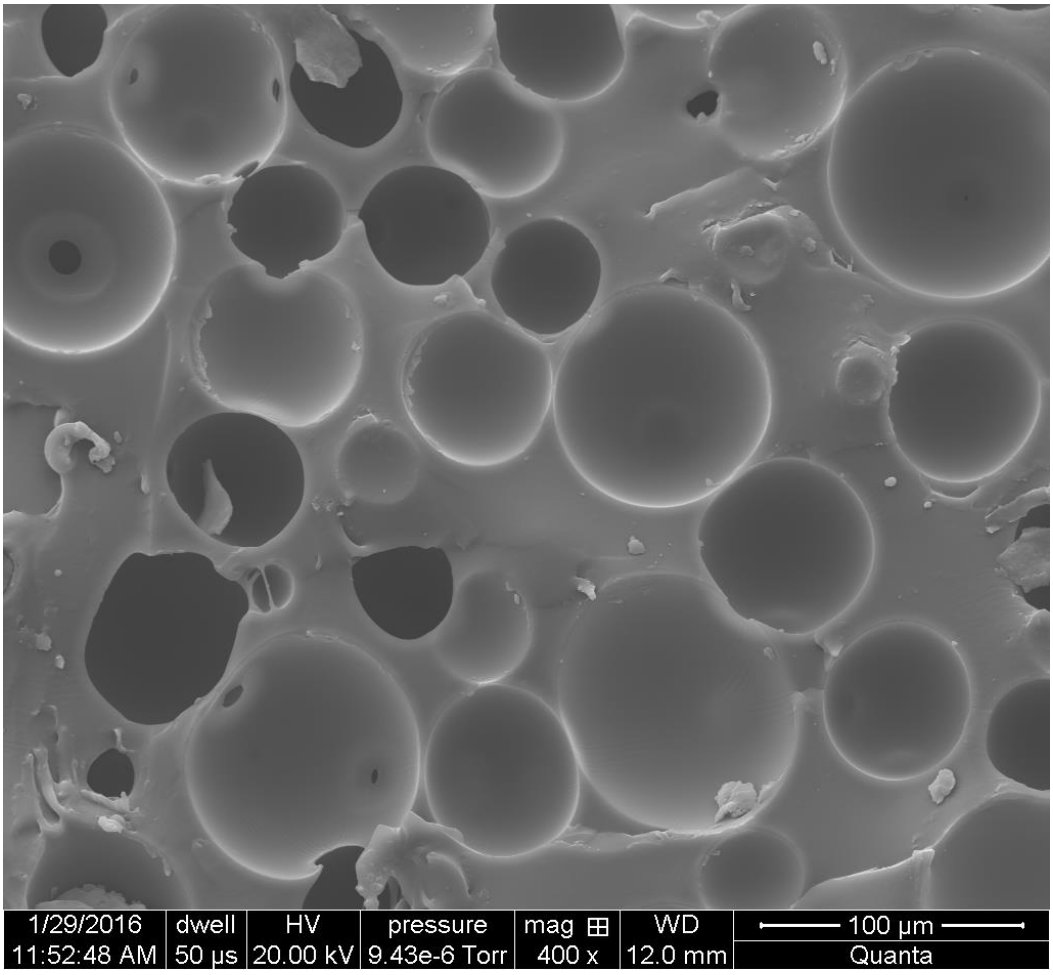

Figure 28. 400X SEM magnification image of D3O® sample.

3.4 Compressions After Impact (CAI) Testing

According to ASTM D7137/D7137M, Compression After Impact (CAI) tests are required to perform damage tolerance analysis of materials subjected to low velocity impacts. As a result, CAI tests were performed on unimpacted and impacted composite coupons. The primary goal of CAI tests was to investigate the drop in compressive strength of coupons after impact. As out-of-plane strength properties of CFRP are lower than their in-plane properties, analyzing compressive strength after impact is important. CAI tests

were performed using a Boeing Compression After Impact Compression Test Fixture obtained from Wyoming Test Fixtures (Salt Lake City, UT) following ASTM D7137/D7137M standards. The test Fixture is shown below in Figure 29. This fixture allows edgewise compression while maintaining constrained boundary conditions on four sides of specimen. Knife edges on the sides allow for axial compression of the specimen while top and bottom clamps are tied to restrict six degrees of freedom at the edge. The fixture is an industry standard and accepts standard size (6 in x 4 in) coupons.

With these types of tests, previous researchers have seen undesirable failure modes (e.g., compressive shear failure at the edge and end crushing brooming) for composite specimens with thicknesses less than about 3 mm (Sanchez, Barbero, Zaera and Navarro, 2005).

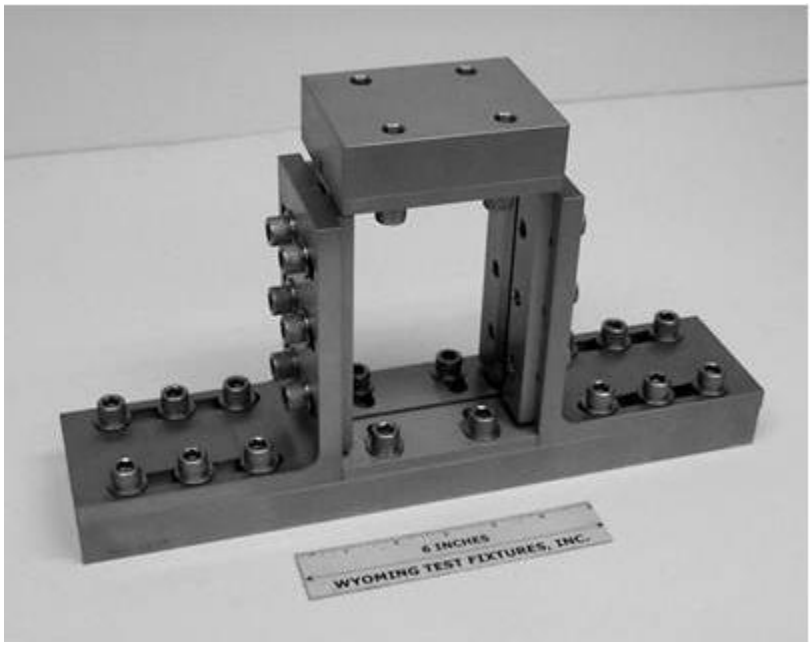

Figure 29. Assembled CAI test fixture (no specimen installed).

Several compression tests were performed on the neat and impacted CFRP coupons of thickness 2.5 mm using an Instron (Norwood, MA) 8802 Servohydraulic Materials Testing Instrument along with the CAI test fixture. The CAI test fixture is seen mounted on the Instron 8802 in Figure 30 below. However, most compression tests resulted in undesirable failure modes including compressive shear failure and crushing at the ends. Since the thickness of the coupons were less than 3 mm, a search was performed, but no reliable ASTM test method or fixture to prevent the compressive failure modes at the ends of coupon was found. Similar phenomenon has been observed by previous researchers (Sanchez et al., 2005). Figure 31 below shows typical failure modes at the ends of compressed composite coupons. Similar failure modes were observed for the impacted and neat CFRP coupons of this work. Therefore, low-velocity impacted specimen compression failure did not diverge from the end failure modes. As a result of these undesirable failure modes seen with thinner samples, coupons were also made with 35 CFRP plies and of thickness 6.25 mm. However, these types of undesirable failure modes were also observed in the thicker coupons.

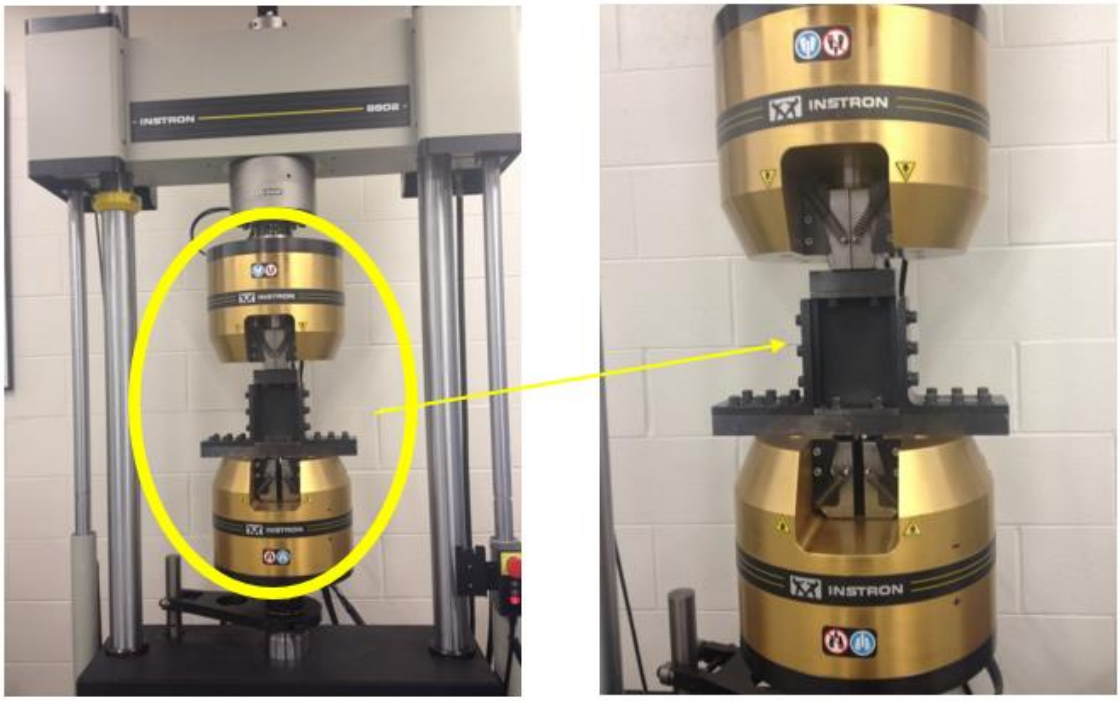

Figure 30. Instron 8802 with CAI test fixture.

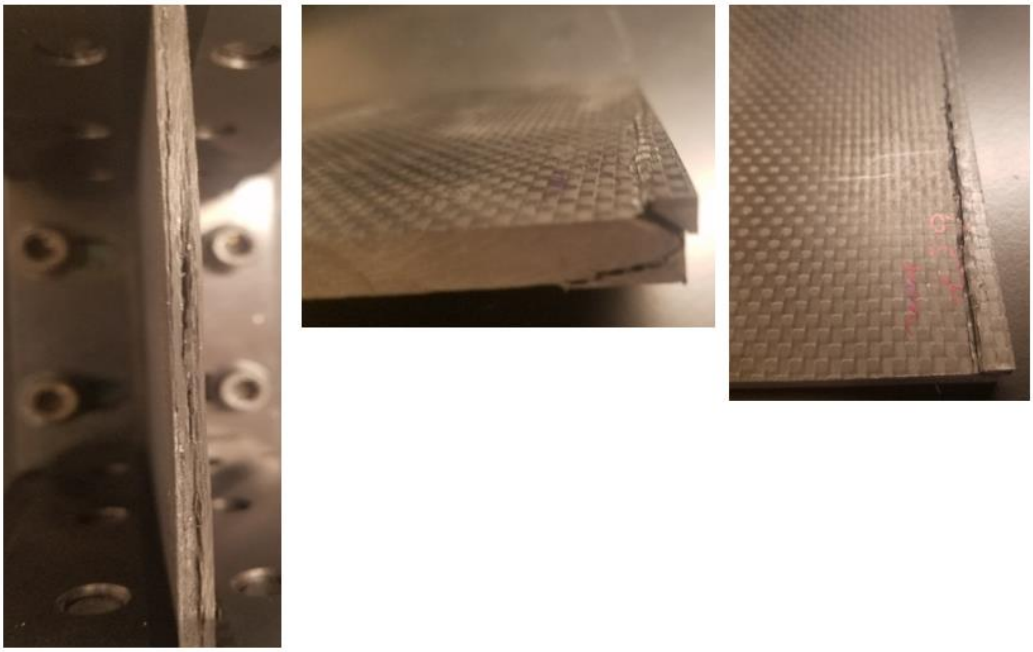

Figure 31. Compressive failure modes. End crushing brooming (left) and edge compression shear (middle and right).

In order to avoid undesirable failure modes, to top knife edge screws in the CAI fixture were clamped firmly while the middle and bottom screws were left moderately tightened. This would help force the damage mode to take place within the text fixture area. This ideology proved to work well and CAI strength of monolithic CFRP panels (neat and impacted) as well as CAI strength of CFRP sandwich panels (impacted) were obtained experimentally. Figure 32 below shows 14 layered CFRP pre and post CAI test coupon which was impacted at 1.25 m/s prior. As evident from the Figure, delamination created during impact expanded during the application of compressive load and the sample eventually cracked through the impacted area as expected. Similar CAI tests were also performed on neat unimpacted CFRP coupon as well as perforated CFRP coupon impacted at 3.0 m/s. Figure 33 and 34 shows the top and bottom surfaces of post CAI tested CFRP coupons. As seen in the Figures, unimpacted neat CFRP specimens failed in the region slightly offset from the center. This can be due to an absence of any delamination prior to CAI testing. Figure 35 shows the Stress vs. Strain curve of the respective coupons during CAI testing. From the Figure, a drop is the residual compressive strength of the impacted CFRP coupons is evident. About 13% drop in compressive strength was observed for the CFRP coupon impacted at 1.25 m/s. Moreover, the drop increased to around 29% for the coupons impacted at 3.0 m/s. Thus, the perforated specimen with 3.0 m/s impact suffered severe damage and the subsequent drop in compressive strength as expected. Since fracture and failure results often show large variations, more tests are needed help confirm and quantify these initial findings.

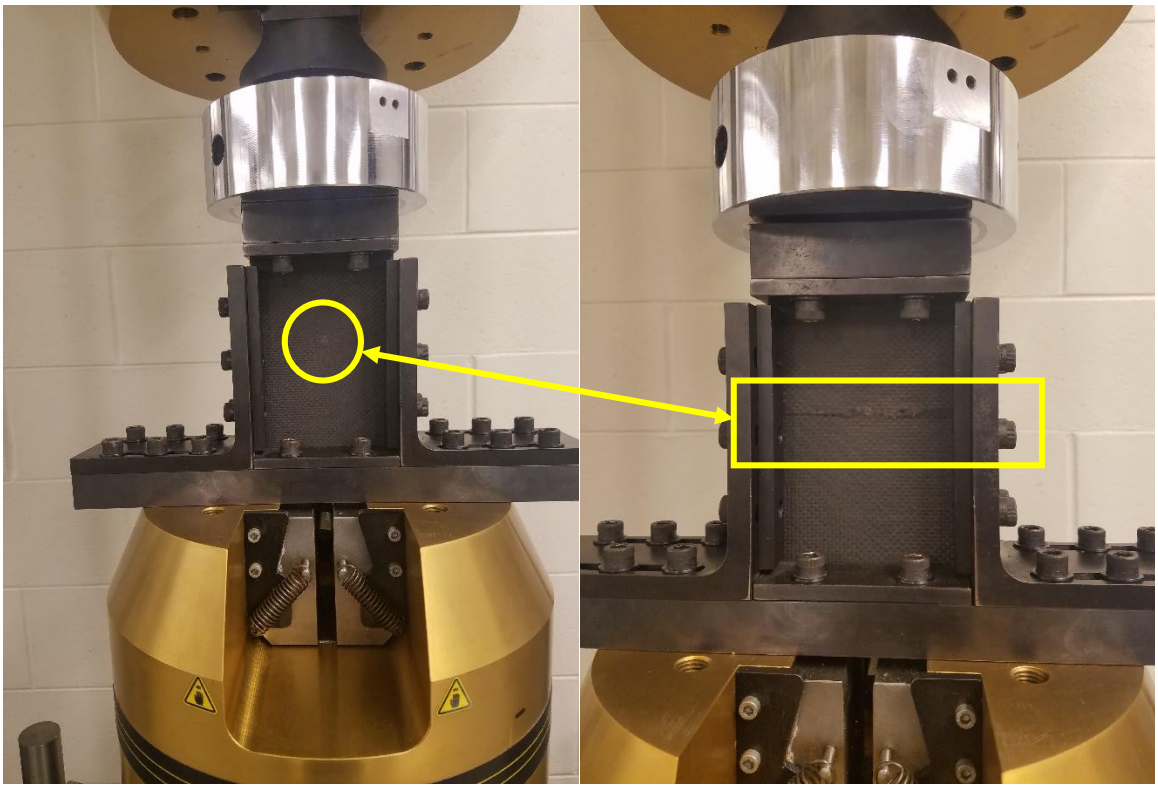

Figure 32. CAI test of 14 layered CFRP impacted at 1.25 m/s. Before (left) and after (right) CAI test images shown.

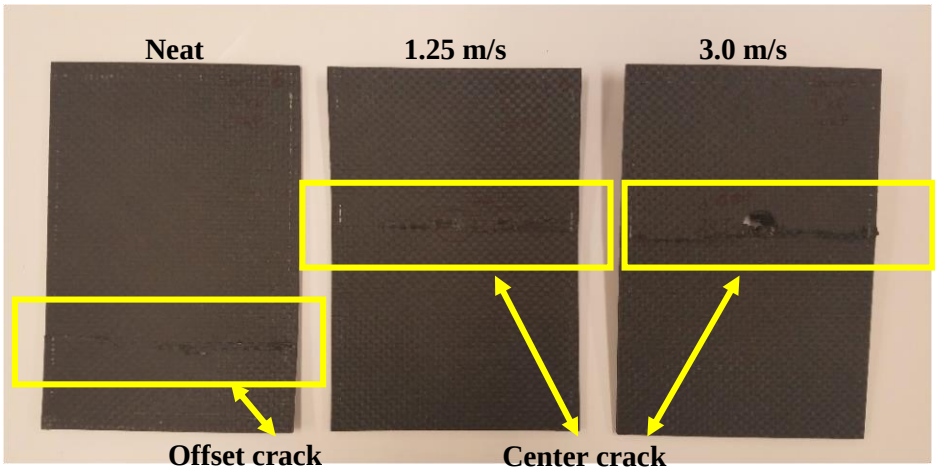

Figure 33. CAI tested 14 layered CFRP coupons (top face). Impacted and unimpacted coupons (left to right).

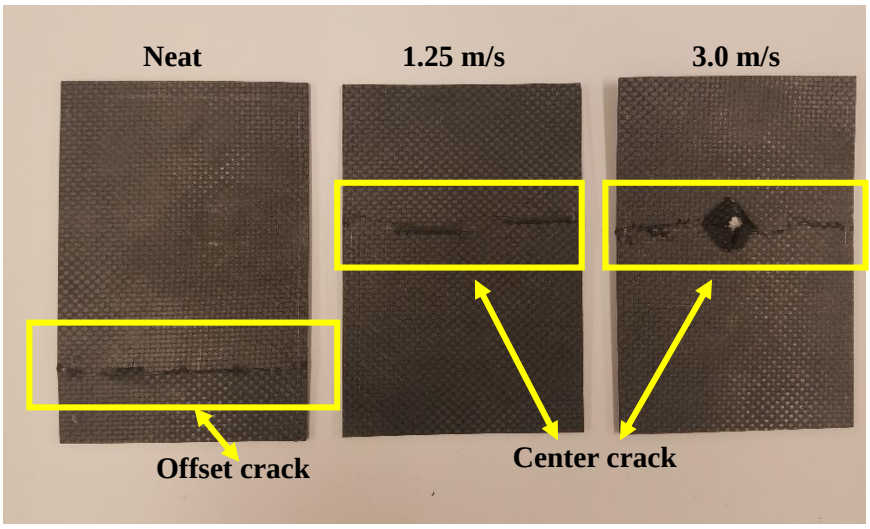

Figure 34. CAI tested 14 layered CFRP coupons (bottom face). Impacted and unimpacted coupons (left to right).

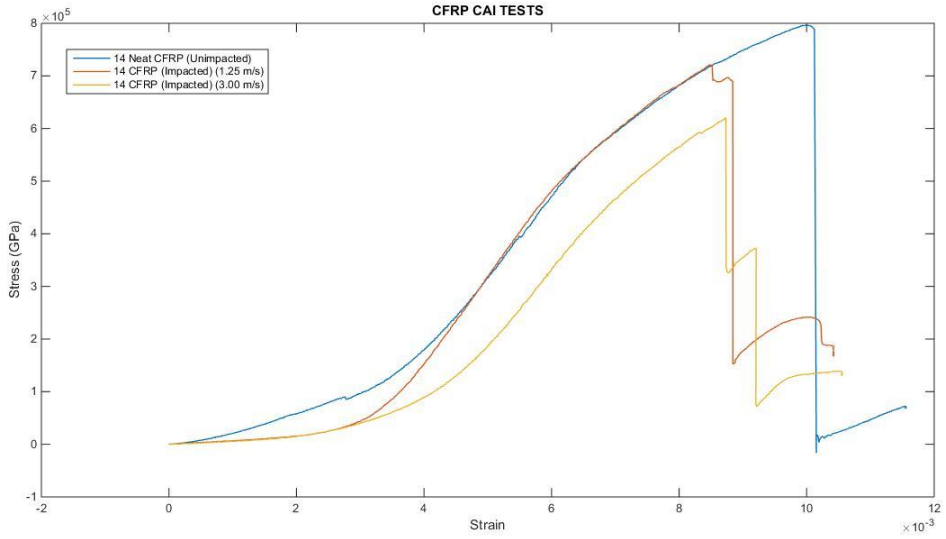

Figure 35. Stress vs. Strain curve of the impacted and unimpacted CFRP coupons during CAI tests.

CAI tests were also performed on the CFRP sandwich structures with Nomex®, Sorbothane® and D3O® cores. These sandwich structures were impacted at 1.25 m/s and 3.0 m/s velocity and then tested for residual compressive stress. Figures 36 and 37 show the front and back faces of CAI tested CFRP sandwich structures pre impacted at 1.25 m/s.

Figures 38 and 39 show the front and back faces of CAI tested CFRP sandwich structures pre impacted at 3.0 m/s. Figure 40 shows the specific Stress vs. Strain curve of the various CFRP sandwich structure configurations. It can be seen that CFRP with a Nomex® core showed the stiffest response compared to the Sorbothane® and D3O® core structures. A slight decrease in peak specific compressive strength was also seen for the Nomex® core sample impacted at 3.0 m/s compared to samples impacted at 1.25 m/s. A similar decrease in strength was also seen in sandwich structures with Sorbothane® and D3O® cores. Furthermore, it was seen that sandwich structures with Sorbothane® and D3O® cores showed a more ductile response, sustaining lower stress (compared to CFRP with Nomex® core) but for a longer period of strain. A complete crack was observed on the faceskins of the CAI tested CFRP sandwich with a Nomex® core accounting for the sudden drop in its compressive strength. Sandwiches with Sorbothane® and D3O® cores showed many small cracks in the CFRP faceskins. However, none of these cracks were able to propagate through the CFRP faceskins perpendicular to the loading direction. Thus, cores with Sorbothane® and D3O® were able to sustain lower loads for greater periods of time as they arrested cracks and forced new cracks to be formed in the faceskins. Additional energy was required to form and propagate new cracks in the faceskins of CFRP structure with Sorbothane® and D3O® cores. CAI stress value of the structure with a D3O® core was higher than that of the structure with a Sorbothane® core as seen in Figure 40 for lower (1.25 m/s) and relatively higher (3.0 m/s) speed impacts. Thus, it was proved that CFRP with D3O® cores can be used to sustain significant amount of compressive force with a more ductile failing mechanism thereby potentially giving the user a significant amount of time to service the damaged structure.

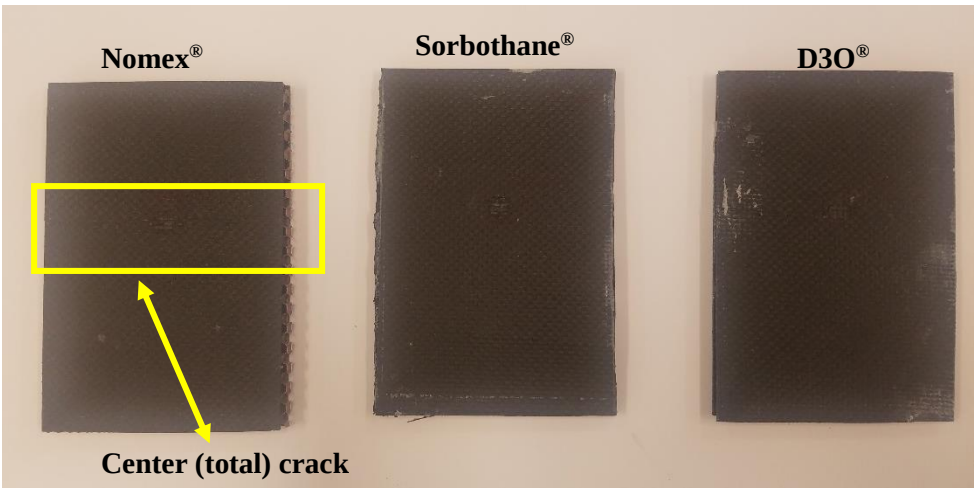

Figure 36. CAI tested CFRP sandwich coupons (front face). Impacted at 1.25 m/s.

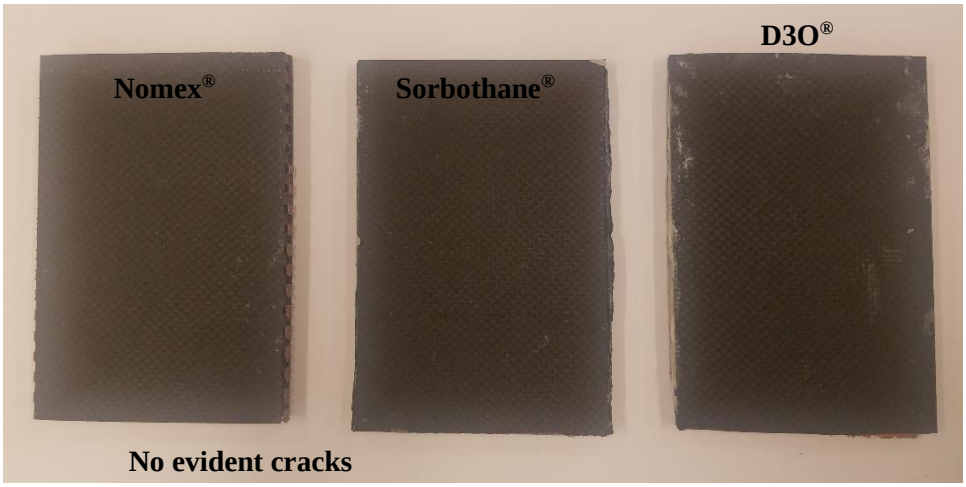

Figure 37. CAI tested CFRP sandwich coupons (bottom face). Impacted at 1.25 m/s.

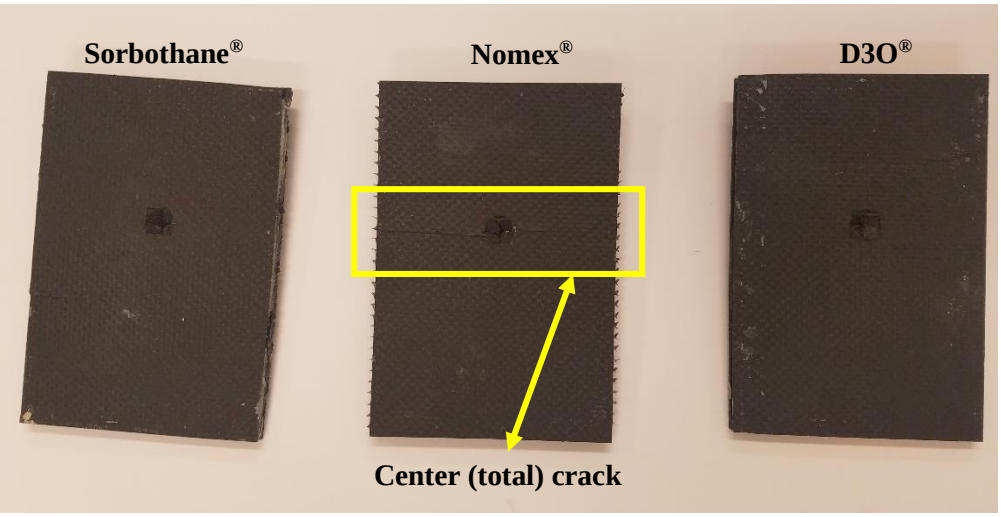

Figure 38. CAI tested CFRP sandwich coupons (front face). Impacted at 3.0 m/s.

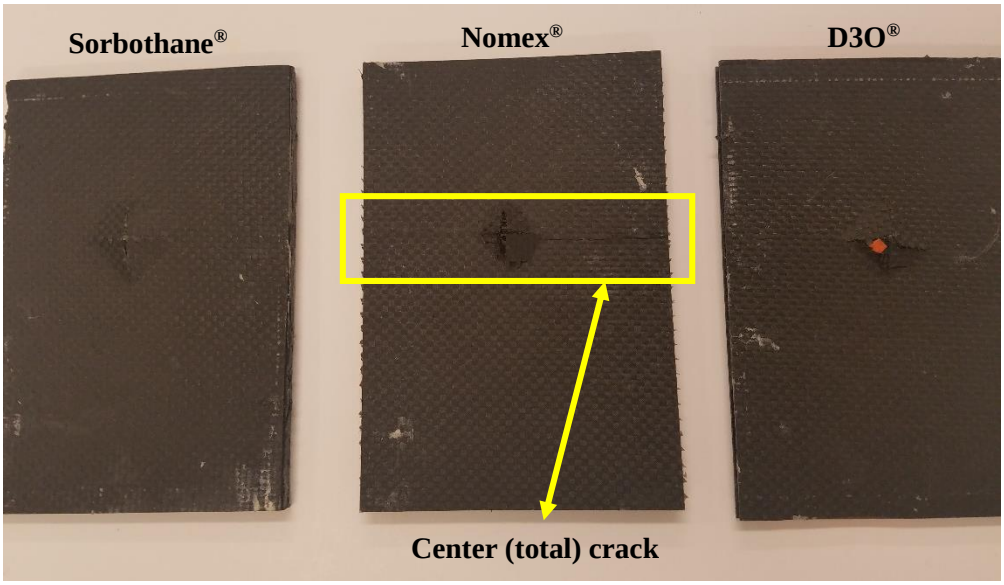

Figure 39. CAI tested CFRP sandwich coupons (bottom face). Impacted at 3.0 m/s.

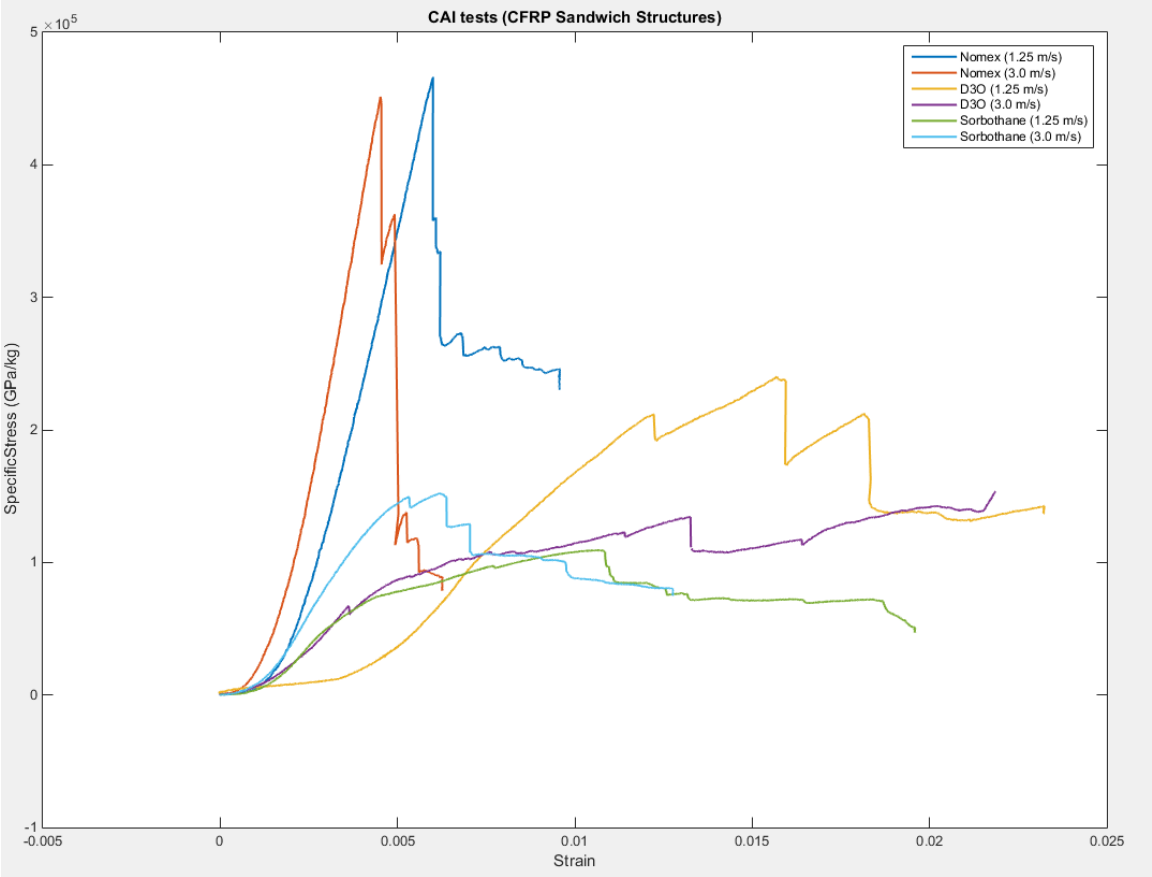

Figure 40. Specific Stress vs. Strain curve of the impacted CFRP sandwich coupons during CAI tests.

4. Numerical Simulation

In order to simulate low-velocity impacts on the 2024-T3 aluminum alloy sheets, as well as neat CFRP and CFRP sandwich specimens, a dynamic finite element model was created in Altair's (Altair Engineering, Troy, MI) Hypermesh pre-processing software. Geometry, mesh, material, property, boundary and initial conditions were applied in Hypermesh for the finite element model. The model was then solved using a commercially available FEA code named LS-DYNA (Livermore Software Technology Corporation (LSTC), Livermore, CA). LS-DYNA is a general purpose finite element code for analyzing large deformation static and dynamic responses of structures including structures coupled with fluids (Zhu, 2016). LS-DYNA was selected because the samples to be analyzed experienced impact loading and were locally deformed between elastic ranges. Analyzed models were then imported back to Altair's Hyperview in order to visualize the damage pattern through stress and displacement contours. Displacement, Energy and Force vs. Time graphs were finally plotted using Altair's Hypergraph post-processing software. These graphs were further compared to the experimental observations for selected impact velocities.

4.1 Aluminum 2024-T3 Impact Simulation

The indenter and 2024-T3 sheet were numerically modelled in Hypermesh and impacted at 1.0 m/s and 1.25 m/s (to simulate the earlier experiments). The 2024-T3 sheet was modelled using MAT_PLASTIC_KINEMATIC (Type 3) (Appendix D) material in order to effectively represent isotropic impact behavior. It was modelled having a 76.2 mm (3 in) diameter (size of the clamping fixture hole in the experimental impact test system) and a thickness of 0.4 mm. As the thickness is considerably less than the other two

dimensions, shell elements were used to mesh the 2024-T3 sheet. Table 1 below shows the input mechanical properties for MAT_PLASTIC_KINEMATIC (Type 3) 2024-T3 material model. Here, ρ, E, ϑ, σ_y and FS represent density, Young's Modulus, Poisson's Ratio, Yield Strength and Factor of Safety respectively. These mechanical properties were obtained from literature and are shown in Appendix E (ASM Aerospace Specification Metals Inc., 2016). The geometry, mesh of plate and impactor are shown in Figure 41 below. The sheet was treated as a slave while impactor was defined as a master contact. The values of coefficients for static and dynamic friction was defined as 0.3 and 0.2 respectively. Only part of hemispherical indenter was modelled and the density was normalized to adjust weight of the modelled indenter to 6.64 kg, similar to the indenter in the actual Instron 9250 HV Impact Test Instrument.

As it can be seen below in Figures 42 - 47, finite element (numerical) predictions of Displacement, Energy and Force vs. Time for the 2024-T3 sheet was very similar to experimental results with minimal error. Again, numerical simulations were performed a impact velocities before total penetration (i.e., 1.0 m/s and 1.25 m/s). By observing Displacement vs. Time graph, it can be inferred that LS-DYNA simulations gave more ductile response. However, Force peak and Energy peak observed numerically were lower than the experimental results. Overall, numerical and experimental results matched rather well giving enough confidence in the mesh sizing and geometry of the simulated model.

Table 1. Input mechanical properties of 2024-T3 sheet for MAT_PLASTIC_KINEMTATIC material card (Type 3).

ρ ($^{kg}/_{mm^3}$)	E (GPa)	ϑ	σ_y (GPa)	FS
2.78 x 10^{-6}	73.1	0.33	0.345	50

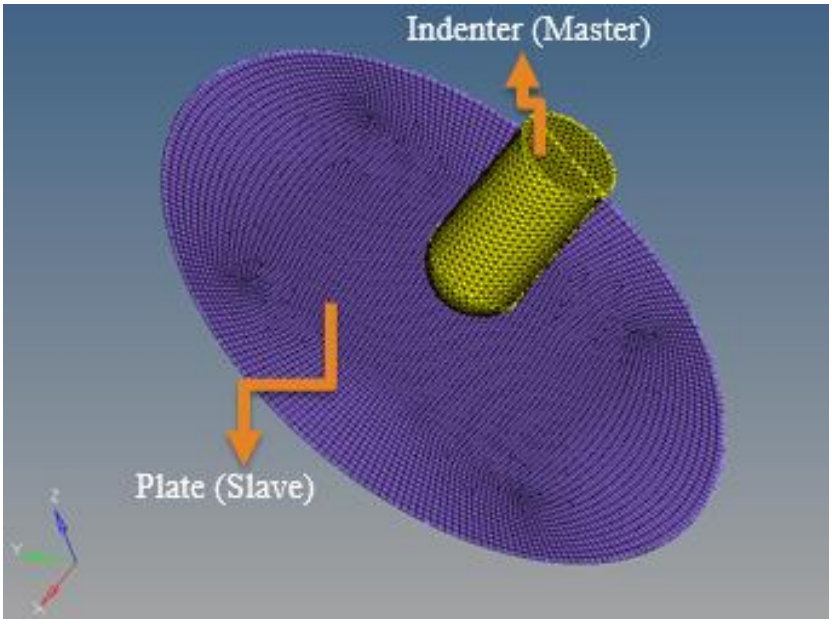

Figure 41. Meshed model of 2024-T3 sheet and indenter in Hypermesh.

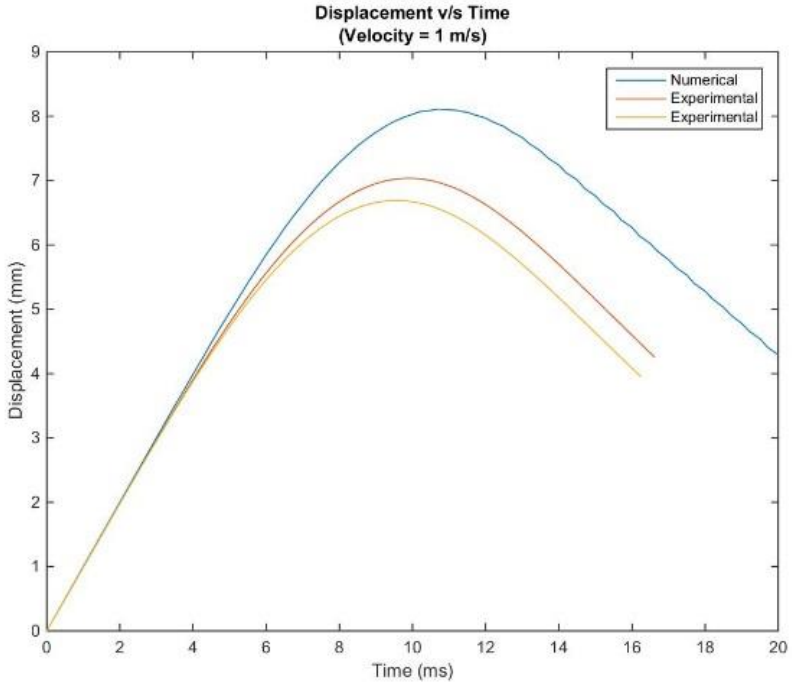

Figure 42. Numerical vs. Experimental comparison of Displacement (mm) vs. Time (ms) curves for 2024-T3 specimen at 1.0 m/s impact.

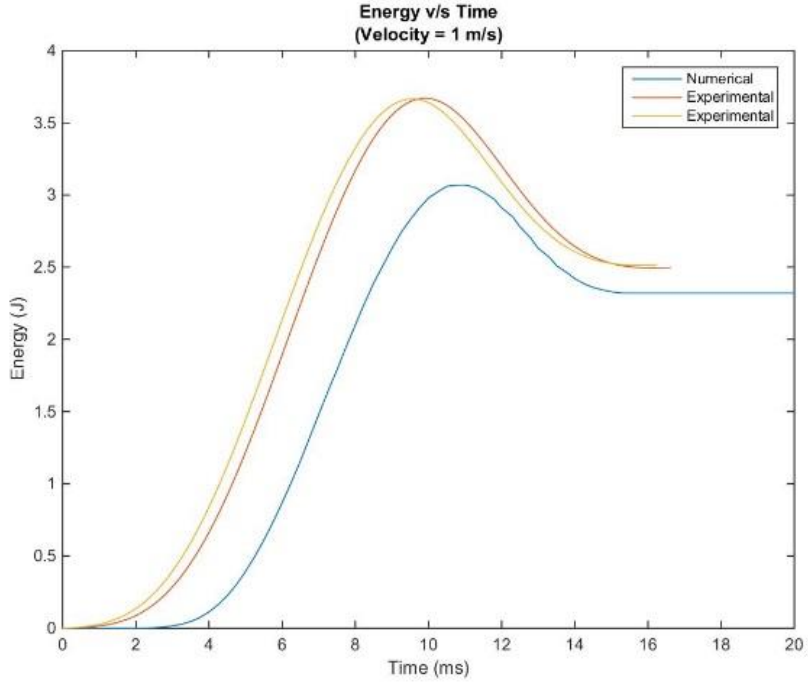

Figure 43. Numerical vs. Experimental comparison of Energy (J) vs. Time (ms) curves for 2024-T3 specimen at 1.0 m/s impact.

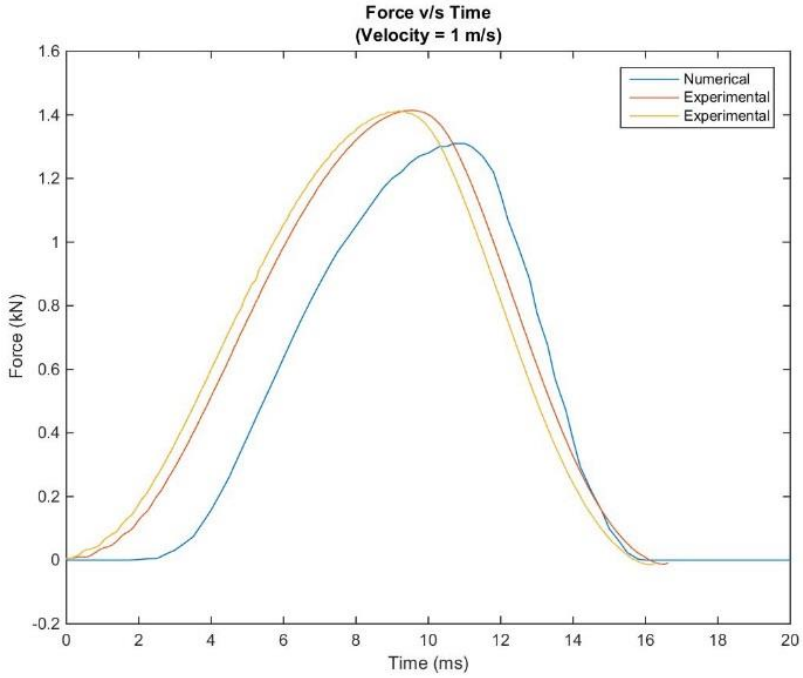

Figure 44. Numerical vs. Experimental comparison of Force (kN) vs. Time (ms) curves for 2024-T3 specimen at 1.0 m/s impact.

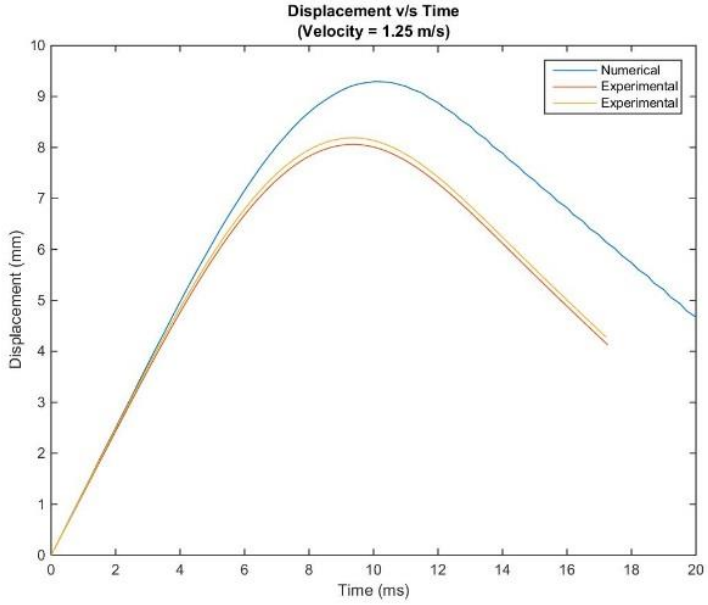

Figure 45. Numerical vs. Experimental comparison of Displacement (mm) vs. Time (ms) curves for 2024-T3 specimen at 1.25 m/s impact.

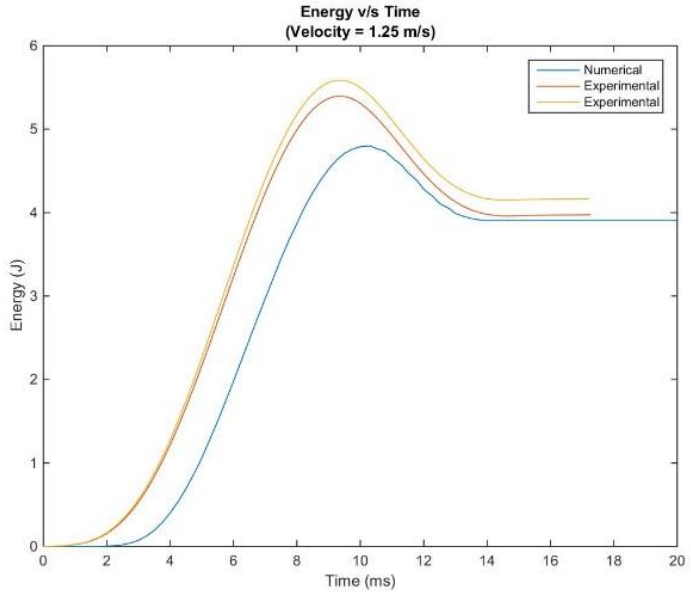

Figure 46. Numerical vs. Experimental comparison of Energy (J) vs. Time (ms) curves for 2024-T3 specimen at 1.25 m/s impact.

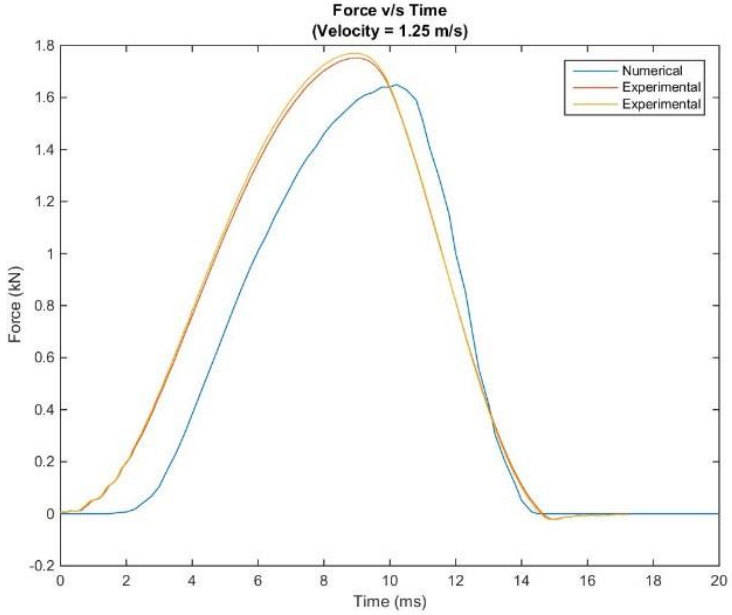

Figure 47. Numerical vs. Experimental comparison of Force (kN) vs. Time (ms) curves for 2024-T3 specimen at 1.25 m/s impact.

4.2 Neat CFRP Plate Impact Simulation

The neat CFRP were also modeled in Hypermesh with the same dimensions as the 2024-T3. Moreover, the same indenter used for modelling impacts on 2024-T3 sheet was used with its inherent material properties and mesh size. As the indenter's mass remained the same along with its properties, importing the proven indenter parameters provided a convenient option. In order to get the high fidelity modelling for composite damage, a material card named MAT_ENHANCED_COMPOSITE_DAMAGE (Type 54-55) was used. Chang-Chang (Appendix B) failure criteria is used which is a strength based failure theory. Chang-Chang failure model is only valid for thin composite shell elements. A variety of failure modes including tensile/compressive fiber failure and tensile/compressive matrix failure is considered in the model. Once the failure criteria is detected for any of the elements, load carrying capacity of that element is deleted as well as the failed element is eroded. Consider different failure mode criteria applicable to Chang-Chang failure model (equation 1, 2 and 3). For each of the failure modes, if the respective damage mode failure value (e_f, e_c, e_m and e_d) is greater than or equal to zero, an element is considered to be failed. If the value is less then zero, then the element is considered elastic and still has load carrying capabilities. Here the in plane stress values (σ_{aa}, σ_{bb} and σ_{ab}) are calculated internally by LS-DYNA while the in plane tensile/compression as well as shear strength of the laminate are inputted by the user in the material card. Final input material card properties are shown in Table 3. Appendix B describes the failure modes in detail for Material Type 54-55 card.

- For the tensile fiber mode:

$$e_f^2 = \left(\frac{\sigma_{aa}}{X_t}\right)^2 + \beta\left(\frac{\sigma_{ab}}{S_C}\right) - 1 \qquad ; \text{where } \sigma_{aa} > 0 \tag{1}$$

- For the compressive fiber mode:

$$e_c^2 = \left(\frac{\sigma_{aa}}{X_c}\right)^2 - 1 \qquad ; \text{where } \sigma_{aa} < 0 \tag{2}$$

- For the tensile matrix mode:

$$e_m^2 = \left(\frac{\sigma_{bb}}{Y_t}\right)^2 + \left(\frac{\sigma_{ab}}{S_C}\right)^2 - 1 \qquad ; \text{where } \sigma_{bb} > 0 \tag{3}$$

- For the compressive matrix mode:

$$e_d^2 = \left(\frac{\sigma_{bb}}{2S_C}\right)^2 + \left[\left(\frac{Y_C}{2S_C}\right)^2 - 1\right]\frac{\sigma_{bb}}{Y_C} + \left(\frac{\sigma_{ab}}{S_C}\right)^2 - 1 \qquad ; \text{where } \sigma_{bb} < 0 \tag{4}$$

A cumulative ABD matrix for the entire 14 layer laminate is obtained by using Femap (Siemens PLM Software, Plano, TX) pre-processing software. The composite lay-up calculation feature in Femap provided the ABD matrix table. Input mechanical properties for individual ply were entered in Femap and are shown in Table 2 below. The units of Young's modulus and shear modulus are GPa. Individual ply and matrix mechanical properties were obtained from the material data sheet shown in Appendix A. Also E_1 and E_2 properties of the laminate are the same as the twill weave composite with 0/90 cross ply as were used in the experimental research. As the moduli G_{12} and ϑ_{12} were not available from the material data sheet and the material characterization for shear modulus was not available in ERAU's material testing laboratories, general values of G_{12} , SC and ϑ_{12} for CFRP prepreg laminates were obtained from the literature (Berg, 1998). Moreover, volume fraction (V) of fiber and matrix in the composite prepreg was obtained from data shown in Appendix A. Cumulative composite laminate mechanical properties

were obtained using "Rule of Mixtures" and reported volume fractions of fibers and matrix in a laminate, Appendix A. Void fraction was considered zero to get the reference numerical values of a perfect laminate with no voids. Equation 5 shows the "Rule of Mixtures" equation applied to find cumulative Young's modulus (E_1 and E_2).

$$E_1 = E_2 = E_{1f}V_f + E_{1m}V_m \tag{5}$$

Table 2. Input mechanical properties of the individual ply entered in FEMAP.

	E_1 (GPa)	E_2 (GPa)	G_{12} (GPa)	ϑ_{12}	V
Fiber	230.974	230.974	-	-	0.64
Matrix	3.0337	3.0337	-	-	0.36
Composite	148.915	148.915	6	0.07	1

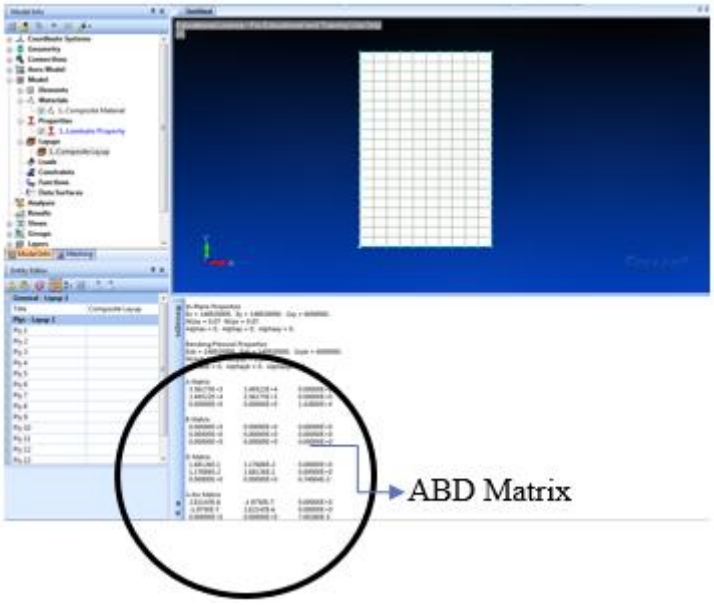

Figure 48. ABD matrix calculation in Femap.

Once the ABD matrix was calculated by Femap for the 14 layered composite prepreg, tension and compressive length of the laminate was obtained using Classical Lamination Theory (CLT) , Figure 39. Equation below shows the load-strain and moment-curvature relationship for the laminate. Here, the unites of N_x, N_y and N_{xy} is force per length while the units for M_x, M_y and M_{xy} is in moment per length. The curvatures (κ_x, κ_y and κ_{xy}) is considered zero as the layup is symmetric about the mid surface. Mid plane failure strains (ε_x^0 and ε_y^0) are calculated for the individual lamina using "Rule of Mixtures" (Equation 6) and CFRP material data sheet shown in Appendix A. Failure strains, ε_x^0 and ε_y^0, are considered same as the laminate has cross-ply lamina orientation. Simplification of Equation 7 yields equation 8. Here N_x is equal to N_y because the values of A_{11} and A_{22} are same. By dividing the value of N_x by the thickness of the laminate, axial tensile strength (XT/YT) is obtained. Furthermore, assumption was made that the failure strains in midplane (ε_x^0 and ε_y^0) would remain same during the compression making the values of tensile strength (XT/YT) same as compression strength (XC/YC) for the cross ply laminate. This assumption was made as the compressive failure strain of fiber and matrix were not indicated in the material data sheet of composite shown in Appendix A.

$$\varepsilon_x^0 = \varepsilon_y^0 = \epsilon_f V_f + \epsilon_m V_m \tag{6}$$

$$\begin{Bmatrix} N_x \\ N_y \\ N_{xy} \\ \hline M_x \\ M_y \\ M_{xy} \end{Bmatrix} = \begin{bmatrix} A_{11} & A_{12} & A_{16} & B_{11} & B_{12} & B_{16} \\ A_{12} & A_{22} & A_{26} & B_{12} & B_{22} & B_{26} \\ A_{16} & A_{26} & A_{66} & B_{16} & B_{26} & B_{66} \\ \hline B_{11} & B_{12} & B_{16} & D_{11} & D_{12} & D_{16} \\ B_{12} & B_{22} & B_{26} & D_{12} & D_{22} & D_{26} \\ B_{16} & B_{26} & B_{66} & D_{16} & D_{26} & D_{66} \end{bmatrix} \begin{Bmatrix} \varepsilon_x^0 \\ \varepsilon_y^0 \\ \gamma_{xy}^0 \\ \hline \kappa_x \\ \kappa_y \\ \kappa_{xy} \end{Bmatrix} \tag{7}$$

0

ABD Matrix (Known)

$$N_x = N_y = (A_{11} + A_{12})\, \varepsilon_x^{\circ} \tag{8}$$

Material properties required for MAT_ENHANCED_COMPOSITE_DAMAGE (Type 54-55) card is calculated and is shown in Table 3. Properties are homogenized so the shell elements can be used. As the thickness of the laminate is significantly lower than its radius, shell elements can be used to model composites as 'through-the-thickness' stress distribution is not a significant parameter. Rule of mixtures is applied to find cumulative E_A, E_B, ϑ_{AB} and ρ properties of a laminate. Moreover, Static and Dynamic coefficient of friction applied between indenter and composite plate was 0.3 and 0.2 respectively. The indenter is treated as a master surface while the composite plate is treated as a slave surface during numerical simulation. In addition, a total penetration scenario (2.0 m/s) was also numerically evaluated in order to check the validity of the model during total penetration impacts. V-shaped diamond looking damage is observed with the simulation, which is very similar to damage pattern observed experimentally. Thus, validity of the model was proven even for total penetration events. Figure 49 below shows the modelling of indenter (Master contact) with CFRP plate (Slave contact). Making elements of indenter as master contact allows plate element to displacement exactly as much as indenter during the impact event. As it is evident from the figure, CFRP plate is made of shell elements and the comprehensive model allows modeling of laminate without thickness.

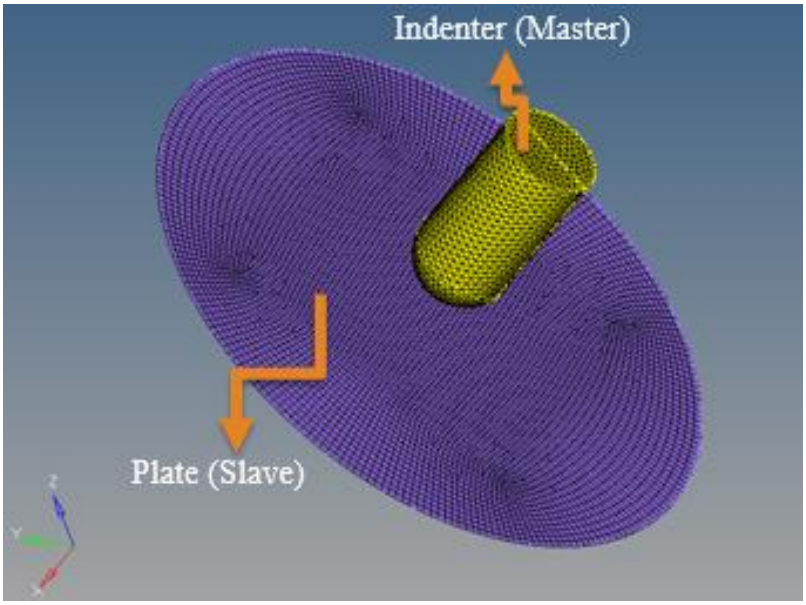

Figure 49. CFRP plate modelling with impact indenter.

Table 3. Input mechanical properties of CFRP laminate (Type 54-55).

$\rho\ (^{kg}/_{mm^3})$	E_A (GPa)	E_B (GPa)	ϑ_{AB}	G_{AB} (GPa)
1.575×10^{-6}	148.92	148.92	0.07	6
XT (GPa)	**XC (GPa)**	**YT (GPa)**	**YC (GPa)**	**SC (GPa)**
0.365	0.365	0.365	0.365	0.055

As it can be seen below in Figures 50-55, finite element (numerical) prediction of Displacement, Energy and Force vs. Time for CFRP laminate was very similar to experimental results with minimal error. Numerical simulations were performed at impact velocities before total penetration (i.e., 1.0 m/s and 1.25 m/s). By observing Displacement vs. Time graph, it can be inferred that LS-DYNA simulations gave more ductile response. However, Force peak and Energy peak observed numerically were lower than the experimental results. Overall, numerical and experimental results matched rather well

giving enough confidence in the mesh sizing and geometry of the simulated model. Moreover, as seen in Figure 52 and Figure 55, numerical force prediction shows first drop in force which is suggestive of matrix failure, way earlier then the experimental initial force drop. Figure 56 shows the displacement contour observed on composite laminate at 1.25 m/s. The simulation was also studied at 2.0 m/s impact speed to confirm the validity of Chang-Chang failure criteria. Figure 57 compares the penetrated shapes of the impacted rear side in the numerical vs. experimental environment. The diamond shaped damage observed on the rear side of impacted laminate is very similar to the numerical penetration shape suggesting the high fidelity of numerical modelling used.

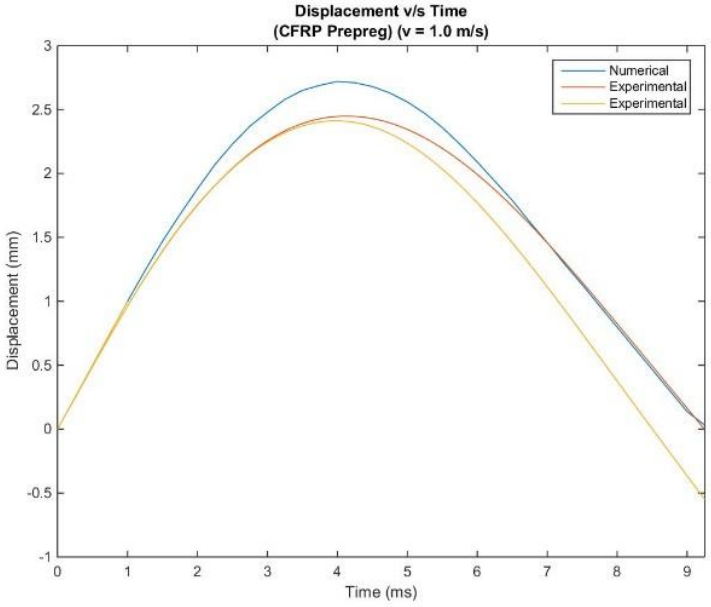

Figure 50. Numerical vs. Experimental comparison of Displacement (mm) vs. Time (ms) curves for 14 layered neat CFRP specimen at 1.00 m/s impact.

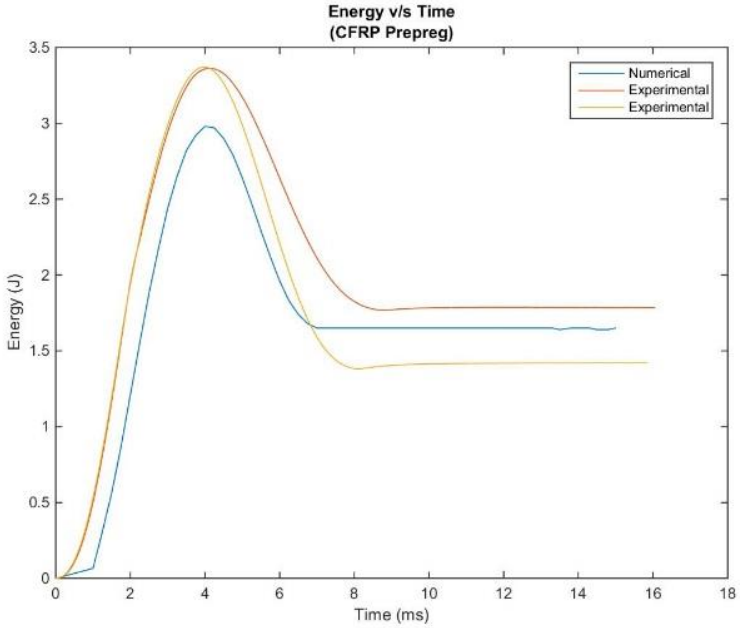

Figure 51. Numerical vs. Experimental comparison of Energy (J) vs. Time (ms) curves for 14 layered neat CFRP specimen at 1.00 m/s impact.

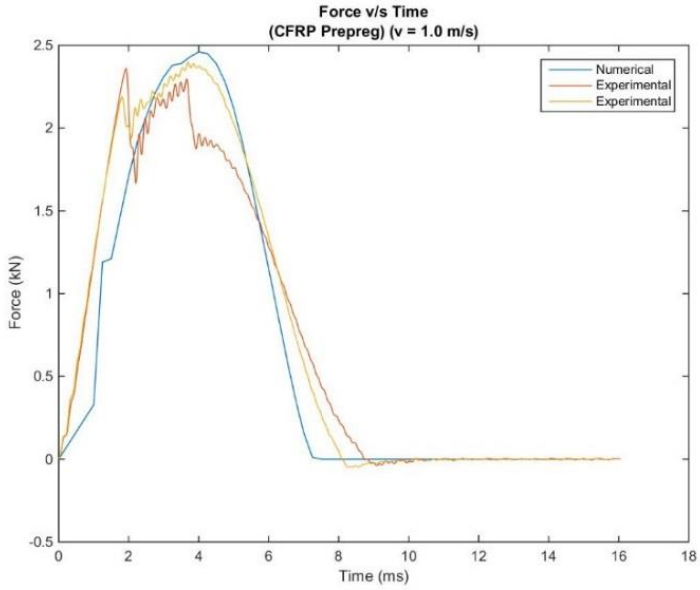

Figure 52. Numerical vs. Experimental comparison of Force (kN) vs. Time (ms) curves for 14 layered neat CFRP specimen at 1.00 m/s impact.

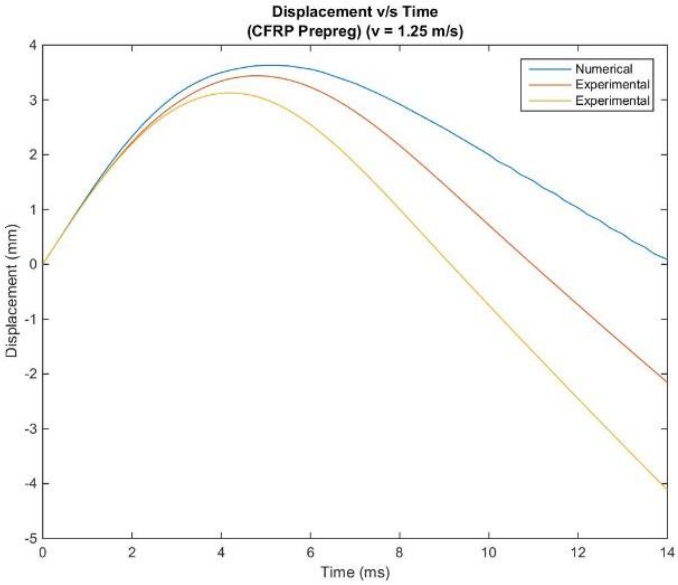

Figure 53. Numerical vs. Experimental comparison of Displacement (mm) vs. Time (ms) curves for 14 layered neat CFRP specimen at 1.25 m/s impact.

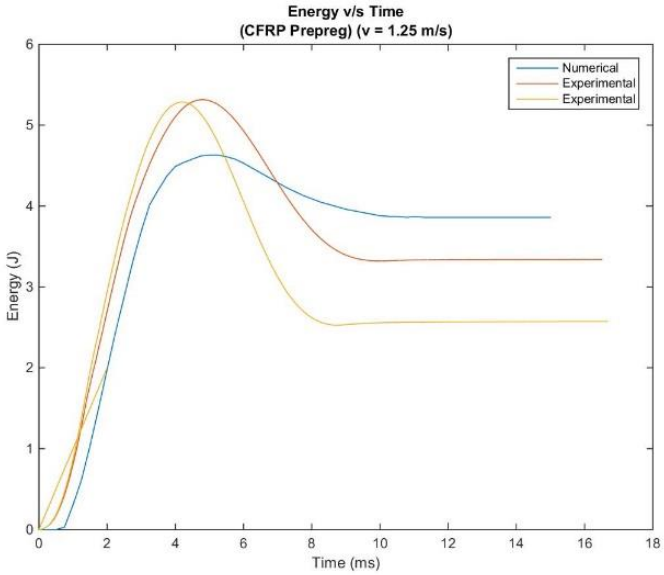

Figure 54. Numerical vs. Experimental comparison of Displacement (mm) vs. Time (ms) curves for 14 layered neat CFRP specimen at 1.25 m/s impact.

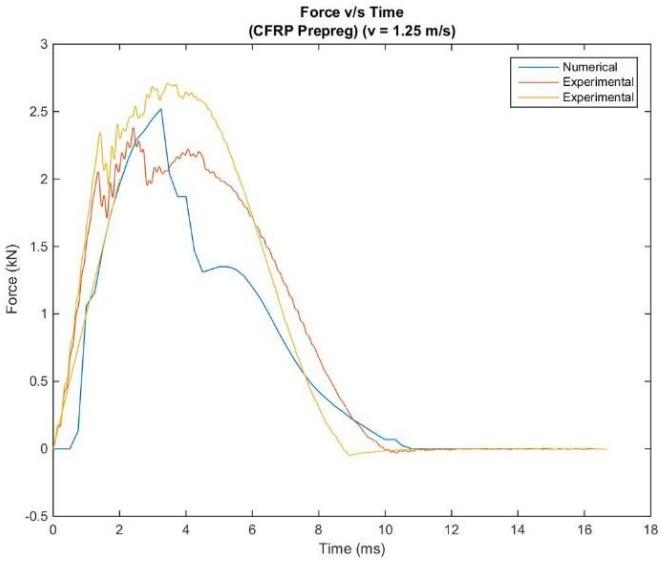

Figure 55. Numerical vs. Experimental comparison of Force (kN) vs. Time (ms) curves for 14 layered neat CFRP specimen at 1.25 m/s impact.

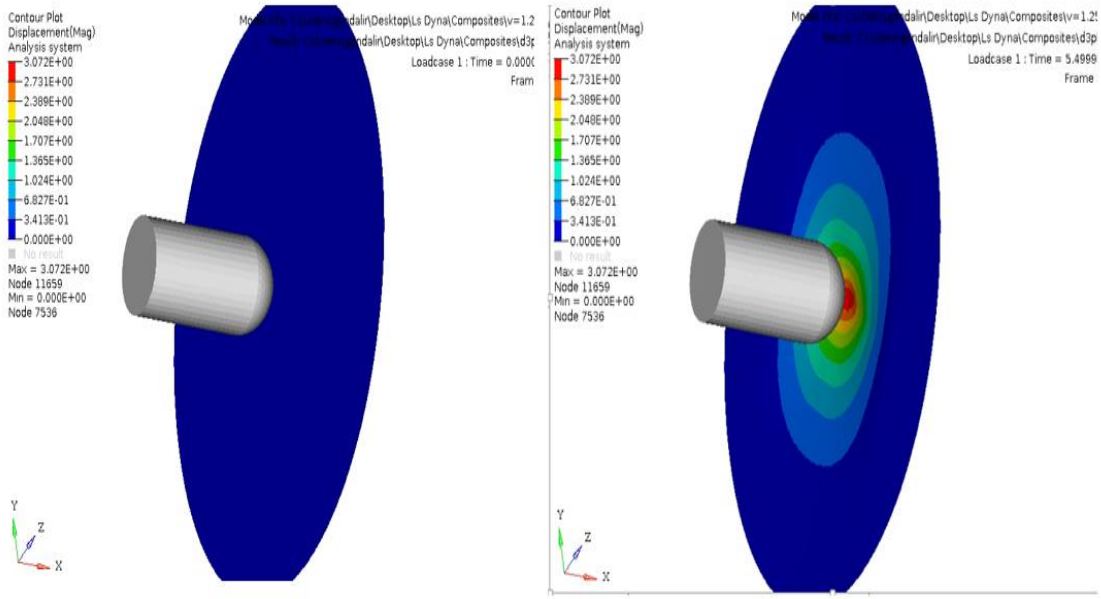

Figure 56. Initial (left) and final (right) displacement contour of 14 layered neat composite sheet at 1.25 m/s.

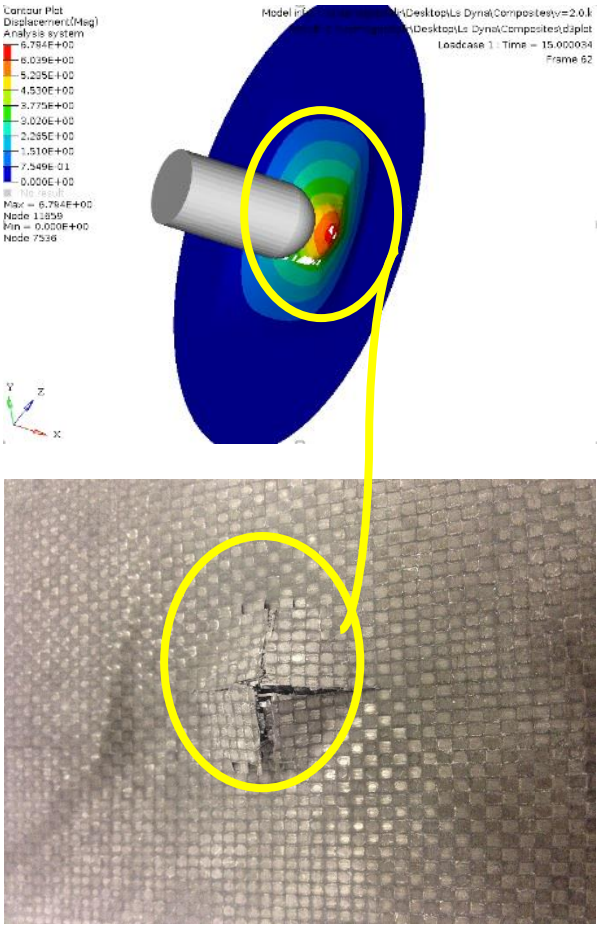

Figure 57. Numerical (top) vs. Experimental (bottom) rear damage at impact velocity of 2.0 m/s.

4.3 Composite Sandwich Structure (Nomex Core) Impact Simulation

Nonlinear Finite Element Analysis code was utilized in LS-DYNA to simulate the low speed impact on Nomex® core sandwich structures with CFRP faceskins. CFRP faceskins were kept of the same mechanical properties and mesh size as the neat CFRP simulation since these results gave close correlation to experimental results. However, mechanical properties were adjusted for 7 layers of CFRP rather than the 14 layered CFRP that were used in neat CFRP impact simulations. Table 4 shows the mechanical properties card input into Hypermesh preprocessing software in order to simulate Nomex®

honeycomb structure. Material card MAT_CRUSHABLE_FOAM (MATL63) (Appendix C) was used to simulate the Nomex® honeycomb core structure. Appendix C shows the detailed Material Type 63 card for LS-DYNA usage. Also the honeycomb modelled was made to be a unitized structure by extracting the 2D planar mesh. Meshing by this method eliminated the need to model the exact geometry of the honeycomb structure. Mesh development time can be saved with reliable results. Strain rate sensitive properties of the Nomex® honeycomb were ignored during this research as this type of core is likely much less strain rate sensitive than the other core materials, D3O® and Sorbothane®.

Table 4. Input mechanical properties of Nomex® honeycomb in Hypermesh

$\rho\ (^{kg}/_{mm^3})$	**E (GPa)**	ϑ	**TSC (GPa)**
3.2 x 10^{-8}	0.018	0.001	0.0045

After modeling the Nomex® honeycomb core by using the MATL63 material card, a compression (crush) test was performed on a 101.6 x 101.6 mm (4 in x 4 in) by a 6.4 mm thick Nomex® honeycomb coupon using a Tinius Olsen (Horsham, PA) Locap 290 testing machine to obtain its experimental stress-strain compressive response. The experimental stress-strain curve was then inputted in MATL63 material card to effectively simulate Nomex® honeycomb structure. The entire philosophy is shown in Figure 58 below.

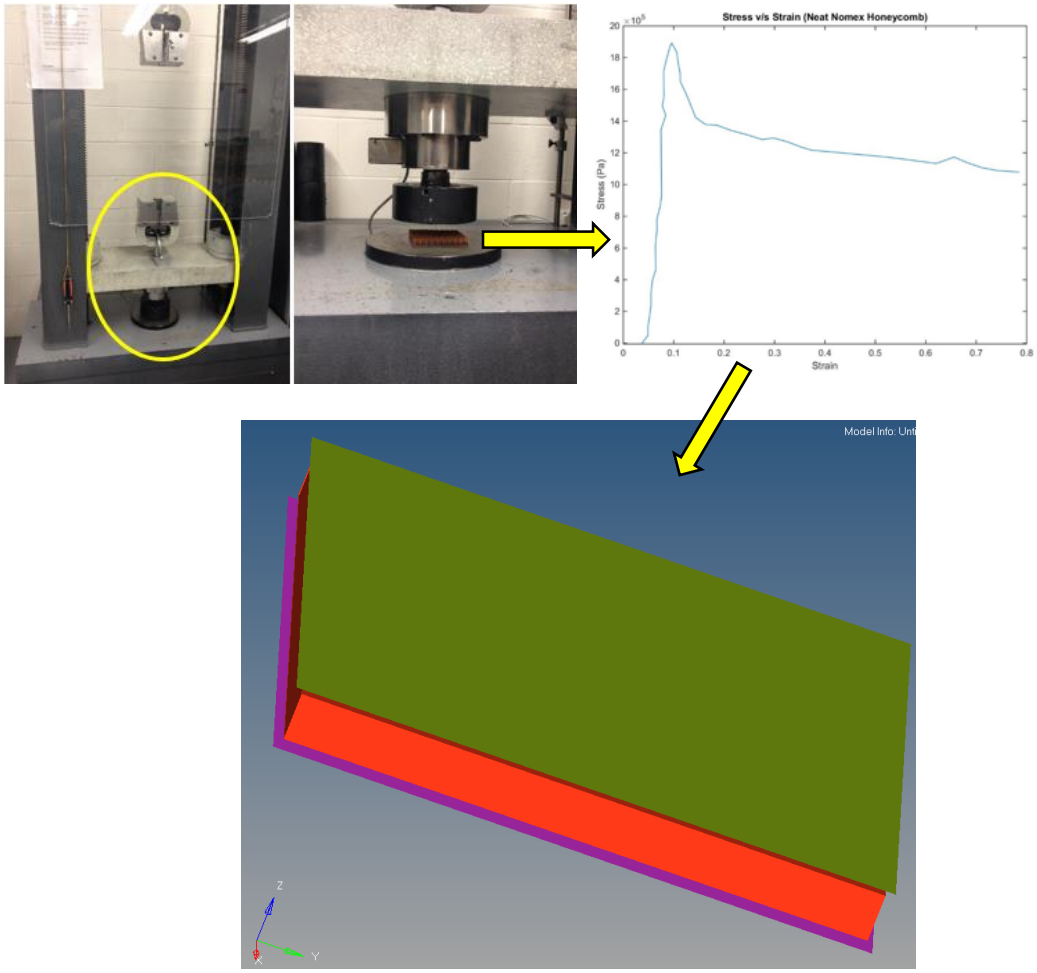

Figure 58. Crush test (top left), experimental stress-strain curve (top right) and FEA modelling of compressive test (bottom).

Finite element model of Nomex® honeycomb is then set up for a compressive test in Hypermesh using LS-DYNA as a processor. This process is done to make sure that the stress-strain curve obtained by numerical modeling matches with the experimental stress-strain curve. As shown in Figure 49, the top and bottom plates were modeled around Nomex® honeycomb to simulate a compression test. The top plate (green) had a small velocity of 0.5 m/s applied to it to simulate a quasi-static compression test while bottom plate (magenta) was kept fixed. Moreover, the Nomex® honeycomb was assumed to be

strain rate insensitive throughout the numerical modeling process. The top and bottom plate were modeled using shell elements and data from the MATL20 material card. Mechanical properties of the plates are shown in Table 5. Furthermore, hourglass control was applied between the plates and honeycomb in order to avoid penetration between their surfaces during the compression. Figure 59 shows the comparison between the numerical and experimental compressive crush test results for the Nomex® honeycomb structure. It can be inferred from the stress-strain curves that the numerical modelling of Nomex® honeycomb is accurate enough to simulate the experimental response. Thus, confidence in the validity of numerical simulation of Nomex® honeycomb structure was established. Note that the slight lag in the numerical stress-strain curve is due to time taken by top plate to reach the honeycomb plus the time taken by honeycomb to touch bottom plate during the compression sequence. This concludes the calibration process for the numerical modeling of Nomex® honeycomb structure. The sandwich component is now ready to be integrated with the CFRP facing skins and to be impact simulated at certain pre-determined velocities.

Table 5. Input mechanical properties of top and bottom plate.

$\rho\ (^{kg}/_{mm^3})$	**E (GPa)**	ϑ	**TSC**
7.83 x 10^{-5}	20	0.33	-

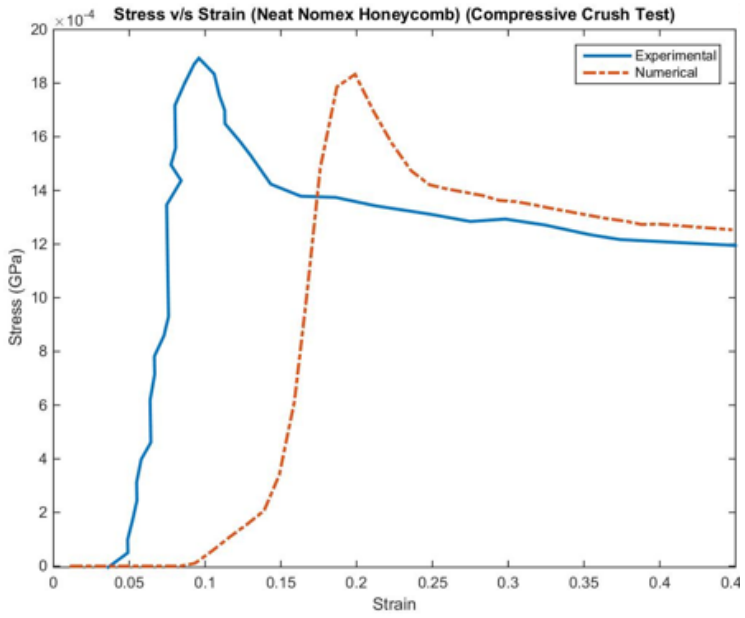

Figure 59. Numerical vs. Experimental Stress (GPa) vs. Strain curves for Nomex® honeycomb structure.

Numerical model for Nomex® honeycomb structure was constructed by basically using the same material properties for honeycomb core as shown in Table 4. The core thickness was modelled as 6.4 mm to represent the fabricated sandwich structure. 7 layer CFRP facing skins were modelled by using material properties as shown in Table 6 below. MAT_ENHANCED_COMPOSITE_DAMAGE (Type 54-55) with Chang-Chang failure criteria was used as impact simulation on monolithic CFRP plates gave relatively similar results to experimental results. Table 6 shows the changed CFRP mechanical properties as 14 layered CFRP was changed to 7 layered composite plate. Numerical simulations were performed for the velocities of 1.0 m/s, 1.25 m/s and 3.0 m/s respectively to correlate with experimental velocities. Figure 60, 61 and 62 compare experimental vs. numerical energy curves of the sandwich panel. Here the energy values represents the energy value of indenter throughout impact phenomenon.

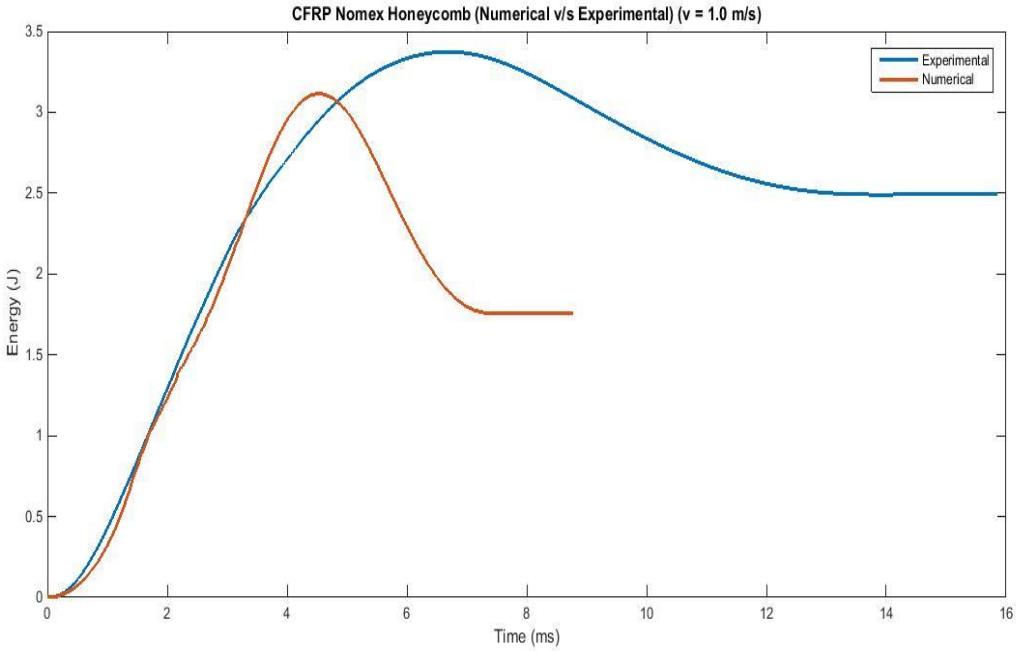

Figure 60. Energy (J) vs. Time (ms) curve for CFRP Nomex® sandwich structure impacted at 1.0 m/s.

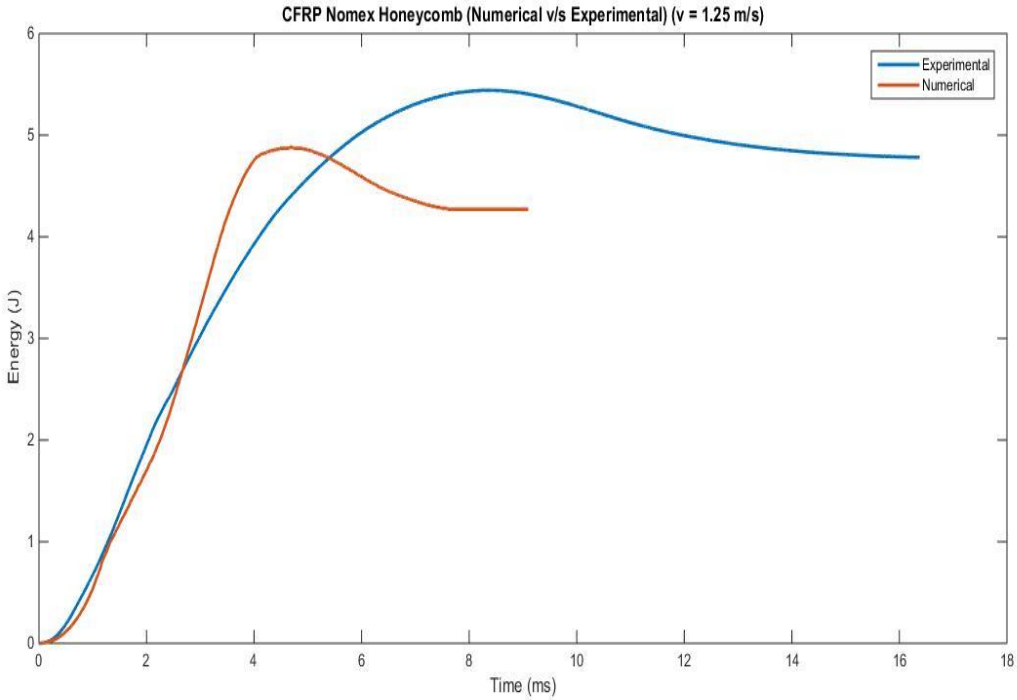

Figure 61. Energy (J) vs. Time (ms) curve for CFRP Nomex® sandwich structure impacted at 1.25 m/s.

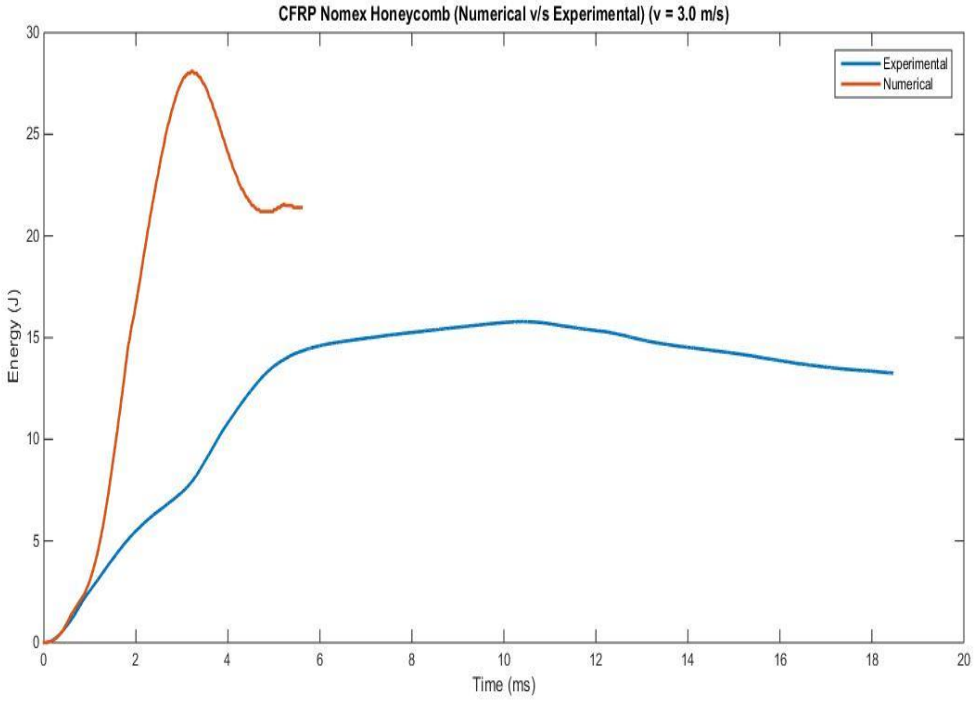

Figure 62. Energy (J) vs. Time (ms) curve for CFRP Nomex® sandwich structure impacted at 3.0 m/s.

From the plots, it can be inferred that the experimental energy curves for the indenter are very similar to the numerical energy curves for the indenter, at least for the elastic deformation event. Numerical impact curves differs from experimental energy curve for relatively higher impact speed of 3.0 m/s. This can be due to the instabilities caused in the numerical simulation at higher speeds as well as because of the strain rate sensitivity of the Nomex® honeycomb which was assumed to be zero for the simulation. Numerical energy absorbed values are compared with experimental energy absorbed in Table 7. Percent difference of numerical values when compared with experimental values are also described in the Table 7. It can be seen that the total energy absorbed approximation by the numerical modelling had a percentage difference of up to 35% for non-total penetration

impact events. However, for impact speed of 3.0 m/s, numerical energy absorbed values differed significantly when compared with experimental values. As the failure criteria for the numerical Nomex® honeycomb is not inputted, load bearing capacity of the core elements is not lost for the total penetration impact events. Failure criteria for the Nomex® honeycomb core was not inputted because of the complexity associated in determining failure criteria parameters of the Nomex® honeycomb structure. Because of these reasons, numerical indenter response is predicted stiffer (Figure 62) while the experimental indenter energy is lower than the numerical approximation.

Figure 63 - 65 show the progression of stress waves on Nomex® honeycomb structure for the impact speeds of 1.0 m/s, 1.25 m/s and 3.0 m/s respectively. The propagation of stress wave is evident in Figures 63 and 64 as the change in impact velocity is not significant. Stress field was more globalized for the impact velocity of 3.0 m/s as seen in Figure 65. Increase in maximum von misses stress is observed inside the Nomex® honeycomb structure as impact speed is increased from 1.0 m/s to 1.25 m/s. However, relatively similar values of maximum von misses was observed with higher Nomex® deformation for the impact event of 3.0 m/s. This is because of the energy expanded by deformation of the core at relatively higher speed impact events.

Table 6. Input mechanical properties of 7 layered CFRP facing skins (Type 54-55).

$\rho\ (^{kg}/_{mm^3})$	E_A (GPa)	E_B (GPa)	ϑ_{AB}	G_{AB} (GPa)
1.575 x 10-6	148.92	148.92	0.07	6

XT (GPa)	XC (GPa)	YT (GPa)	YC (GPa)	SC (GPa)
3.857	3.857	3.857	3.857	0.055

Table 7. Numerical vs. Experimental Energy (J) absorbed for composite sandwich.

Numerical	Energy (J)	Percentage Difference
V = 1.00 m/s	1.7594	-
V = 1.25 m/s	4.26711	-
V = 3.00 m/s	21.397	-
Experimental		
V = 1.00 m/s	2.493	34.5029
V = 1.25 m/s	4.78	11.3382
V = 3.00 m/s	13.26	46.9573

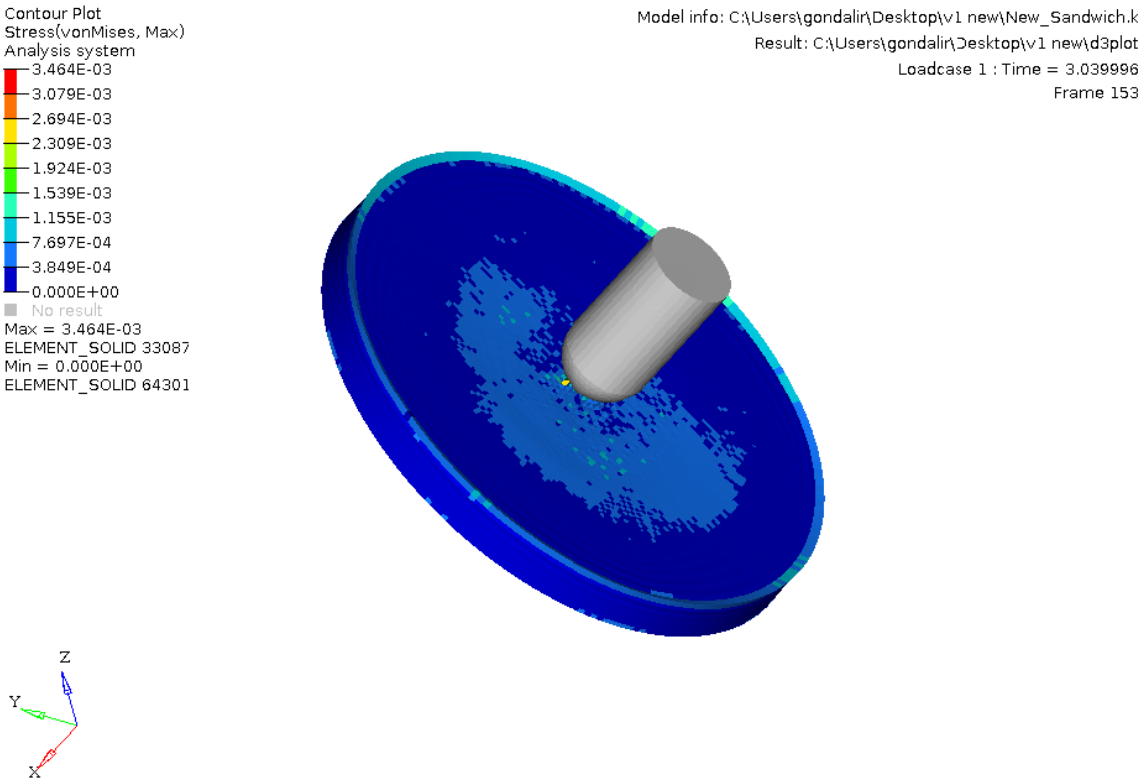

Figure 63. Von Misses Stress (GPa) contour on Nomex® honeycomb at 1.0 m/s impact.

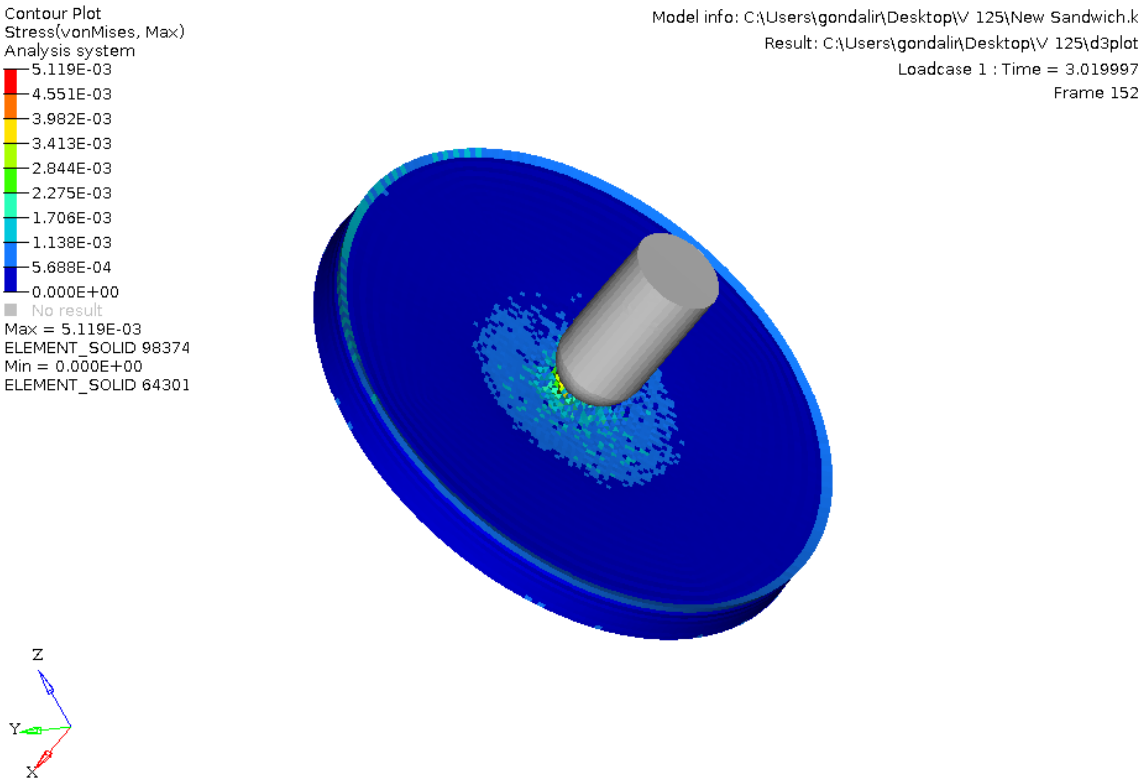

Figure 64. Von Misses Stress (GPa) contour on Nomex® honeycomb at 1.25 m/s impact.

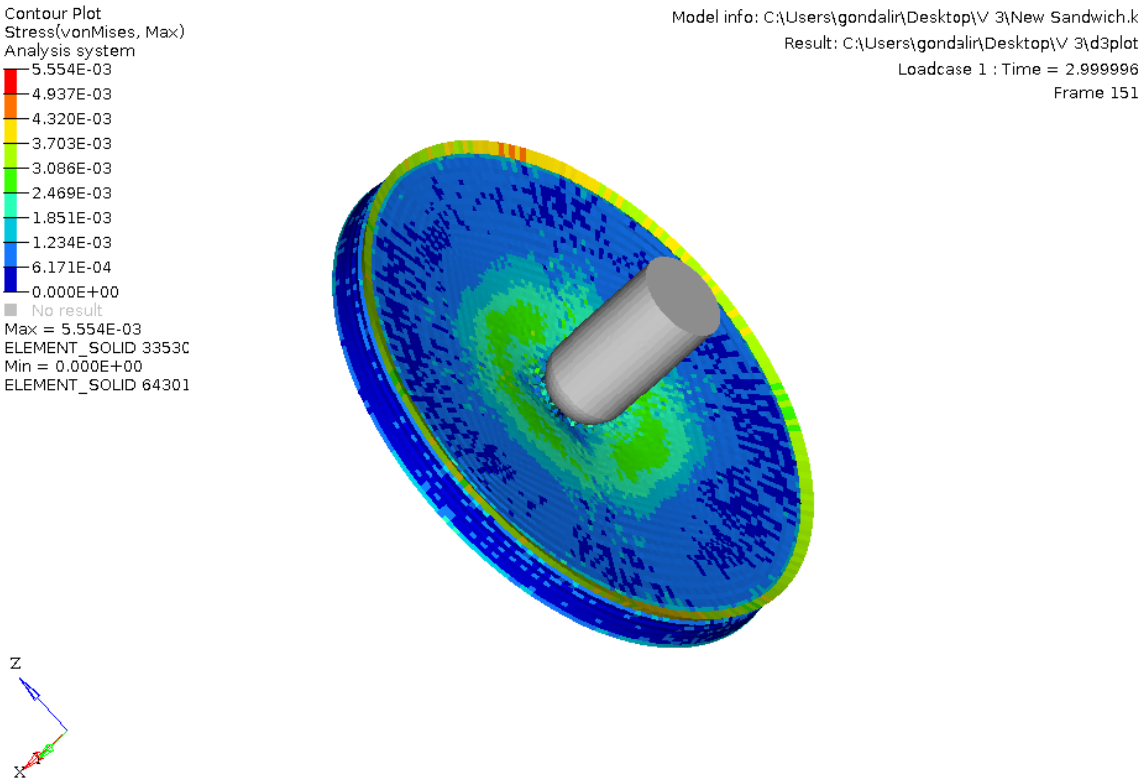

Figure 65. Von Misses Stress contour (GPa) on Nomex® honeycomb at 3.0 m/s impact.

5. Conclusions

2024-T3 aluminum sheet, neat CFRP laminates and sandwich structures with CFRP faceskins of varying cores were studied for their low velocity impact and damage tolerant behavior.

- It was observed that neat CFRP showed a stiffer response with higher peak force during low velocity impact compared to 2024-T3 aluminum sheet and sandwich structures with varying cores.
- Amongst sandwich structures, Nomex® honeycomb core with CFRP faceskins absorbed more specific energy compared to sandwich structures with Sorbothane® and D3O® cores at impact speeds of 1.0 m/s and 1.25 m/s.
- At relatively higher impact speeds of 3.0 m/s, the strain rate sensitivity of D3O® was evident as sandwich structure with CFRP faceskins and D3O® core showed higher specific energy absorption and higher energy per thickness values.
- It was proved that for low velocity impacts greater than or equal to 3.0 m/s, usage of D3O® in composite sandwich structures can yield a lighter and thinner sandwich structure.
- CAI tests for impacted neat CFRP coupons showed a drop in the compressive residual strength when compared to the compressive strength of unimpacted samples.
- Impacted CFRP sandwich coupon with D3O® and Sorbothane® core showed ductile compressive response during CAI tests when compared to CFRP sandwich coupon with Nomex® honeycomb core.

- It was observed that CAI strength of CFRP sandwich structures with a Nomex® honeycomb core was higher than CFRP sandwich coupon with D3O® and Sorbothane® cores.
- Numerical models for 2024-T3 aluminum sheet, neat CFRP laminate and sandwich structure with CFRP faceskins were developed in Hypermesh/ LS-DYNA and verified with experimental results for the dynamic impact loading scenario.
- Modelling approached explained here can save time and money at the coupon level testing as expensive experimentation required for impact testing can be avoided in future.

6. Recommendations And Future Work

The effect of using strain rate sensitive core with CFRP faceskins is discussed in this research. However, future research can be done on improving the damage tolerance of the faceskins by using particulates of strain rate sensitive material into the epoxy of composite. This type of usage can further save the weight of the composite as well as might increase damage tolerance. Moreover, more experiments should be conducted for impact speeds greater than 3.0 m/s to get the broad view on the effect of strain rate sensitivity of D3O® core. Numerical model of CFRP sandwich with D3O® and Sorbothane® core can be developed by performing appropriate material characterization tests on D3O® and Sorbothane® core. Failure criteria parameters for the Nomex® core should be determined its high fidelity numerical modelling. Moreover, strain rate sensitive property of the Nomex® core should be applied in the numerical modelling for accurate prediction of impact behavior at relatively higher impact speed events (e.g. 3.0 m/s). Industry partnership is also referred for the suggested sandwich structure to be fabricated and tested from coupon to component level.

REFERENCES

A350 XWB Technology and innovation. Retrieved from http://www.airbus.com/aircraftfamilies/passengeraircraft/a350xwbfamily/technology-and-innovation/.

Abrate, Serge. (1998). Impact on Composite Structures. pp. 135-228.

ASM Aerospace Specification Metals Inc. (2016). Aluminum 2024-T3. Retrieved from http://asm.matweb.com/search/SpecificMaterial.asp?bassnum=MA2024T3

Berg, K. (1998). Typical Properties For Advanced Composites. Handbook of Composites, pp. 1053-1068.

Christoforou and A.P. (2001). Impact Dynamics and damage in composite structures. Composite Structures, Vol. 52(2), pp. 181-188.

Cook, L., Boulic, A., Harris, D., Bellamy, P and Irving, P.E. (2012). Reliability of Damage Detection in Advanced Composite Aircraft Structures. Safety Regulation Group, Civil Aviation Authority.

D3O® Impact Solutions. (2016). How D3O® Technology Works. Retrieved from http://www.d3o.com/materials/how-d3o-technology-works/.

Dahsin, L. (1988). Impact-Induced Delamination - A View of Bending Stiffness Mismatching. Journal of Composite Materials, Vol. 22, pp. 674-692.

Davies, G.A.O. and Robinson, P. (1992). Predicting failure by debonding/delamination, AGARD: 74th Structures & Materials Meeting, Debonding/Delamination of Composites.

Davies, G.A.O. and Zhang, X. (1994). Impact Damage Prediction in Carbon Composite Structures. International Journal of Impact Engineering, Vol. 16, No. 1, pp. 149-170.

Dobyns, A.L. and Porter, T.R. (1981). A Study of the Structural Integrity of Graphite Composite Structure Subjected to Low Velocity Impact. Polymer Engineering and Science, Vol. 21, No. 8, pp. 493-498.

Dorey, G., Sigerty, P., Stellbrink, K. and Hart J. 'r, W.G. (1987). Impact damage tolerance of carbon fibre and hybrid laminates, Garteur TP-037, Royal Aircraft Establishment technical Report 87057

Faivre, V. and Morteau, E. (2011). Damage Tolerant composite fuselage sizing. Characterisation of accidental damage threat. 48th Flight Airworthiness Support Technology (FAST) Report.

Greenhalgh, E. and Hiley, M. (2003). The assessment of novel materials and processes for the impact tolerant design of stiffened composite aerospace structures. Composites Part A: Applied Science and Manufacturing, 34(2):151-161.

Horton, R.E. and McCarty, J.E. (1987). Damage Tolerance of Composites. Engineered Materials Handbook, Vol. 1, Composites, ASM International

Jackson, W.C. and Polis D.L. (2015). Use of a New Portable Instrumented Impactor on the NASA Composite Crew Module Damage Tolerance Program. 29th American Society for Conference and 16th US-Japan Conference and ASTM D30 Meeting, September 8-10, 2014.

Liu, D. (1988). Impact-Induced Delamination – A View of Bending Stiffness Mismatching. J. of Composite Materials, Volume 22, pp. 674-692.

Marom, G., Drukker, E., Weinberg, A. and Banbaji, J. (1986). Impact behaviour of carbon/Kevlar hybrid composites. Composites 17, 00~0.

Nettles, A.T. (2010). Damage tolerance of composite laminates from an empirical perspective. NASA Technical Reports Server, Doc 20100005132.

Reid, S.R. and Zhou, G. (2000). Impact Behaviour of Fiber-Reinforced Composite Materials and Structures. Woodhead Publishing Limited, pp. 1-3.

Sanchez-Saez, S., Barbero, E., Zaera, R. and Navarro, C. (2005). Compression after impact of thin composite laminates. Composites Science and Technology, Vol. 65, Issue 13, pp. 1911-1919.

Sarlin, E., Apostol, M., Lindross, M., Kuokkala, V.-T., Vuorinen, J., Lepisto, T. and Vippola, M. (2014). Impact properties of novel corrosion resistant hybrid structures. Composite Structures, Volume 108, pp. 886-893.

Starnes, J.H., Dickson, J.N. and Rouse, M. (1984). Postbuckling Behavior of Graphit-Epoxy Panels. ACEE Composite Structure Technology Conference, Seattle, Wash., August 13-16, 137-159 (NASA CP 2321).

Ted Pilla, Inc. (2016). 108 Manual Sputter Coater. Retrieved from http://www.tedpella.com/cressington_html/Cressington-108-Manual-Sputter-Coater.htm

Yang, B., Wang Z., Zhou L., Zhang J., Tong L. and Liang W. (2015). Study on the low-velocity impact response and CAI behavior of foam-filled panels with hybrid facesheet. Composite Structures, Volume 132, pp. 1129-1140.

Waite S. (2006). FAA Damage Tolerance and Maintenance Workshop

Wyoming Test Fixtures Inc. Boeing Compression After Impact Compression Test Fixture (ASTM D 7137). Retrieved from http://www.wyomingtestfixtures.com/Products/c3.html

Zhu, F. (2016). Introduction to LS-DYNA [PowerPoint slides]. Retrieved from https://erau.instructure.com/courses/28313/discussion_topics/414093

Appendices

Appendix A: CFRP Prepreg Material Properties (ACP Composites, Livermore, CA)

Carbon Fiber Room Temperature Storage Prepreg

Our Carbon Fiber Room Temperature Prepreg is a 5.9oz 2x2 twill weave fabric woven from 3K carbon fibers and impregnated with a thermosetting epoxy resin system. It is storable at room temperatures and does not require freezer storage. With the long out life of the resin matrix, the carbon fiber prepreg can be shipped and handled at room temperatures. It is ideal for use when a long shelf life is desired, high-temperature capabilities are not required and controlled resin content is wanted.

Physical Fabric Properties	
Weight	5.9 oz/yd^2
Thickness	.012"
Construction (W x F)	13x13 2x2 Twill Weave
Fiber Type	3K Carbon Fiber Standard Modulus PAN, 33MSI
Resin Matrix	Thermosetting Epoxy
Resin Content	36%

Technical Resin Properties	
Density	1.229 g/cc
Tg (fromG" DMA curve)	270°F
Tensile Strength	10.7 ksi
Tensile Modulus	440 ksi
Elongation @ Break	4.0%
Tg after 24hr Water Boil	169°F
Water Absorption	3.9%

Cure Cycles

There are three optional cure cycles. All three will produce similar properties.

1. • 5°F-per-minute ramp up to 310°F (154°C)
   • Hold for 1 hour
   • <5°F-per-minute ramp down to at least 150°F (66°C) before removing from oven
2. • 5°F-per-minute ramp up to 290°F (154°C)
   • Hold for 2 hours
   • <5°F-per-minute ramp down to at least 150°F (66°C) before removing from oven
3. • 5°F-per-minute ramp up to 270°F (154°C)
   • Hold for 4 hours
   • <5°F-per-minute ramp down to at least 150°F (66°C) before removing from oven

Shelf Life/Storage

The material should remain sealed when not is use and be stored indoors, out of the weather.

- The shelf life is 6 months from the date of manufacture when the maximum storage temperature shall not exceed 90°F (32°C).
- The shelf life is 12 months from the date of manufacture when the maximum storage temperature shall not exceed 75°F (24°C).
- The shelf life is 30 months from the date of manufacture when the maximum storage temperature shall not exceed 0°F (-18°C), with an additional 6 months at <75 °F (24°C).

ACP Composites
1-800-811-2009
www.acpsales.com

Woven Carbon Fiber Fabric

Carbon Fiber fabrics offer technical properties that are popular in various applications where its high strength-to-weight ratio is of importance. In addition to its high strength-to-weight ratio, carbon fabrics are thermally and electrically conductive. The term carbon fiber is used interchangeably with graphite. However, carbon fibers and graphite fibers are made and heat treated at different temperatures and have different carbon contents. ACP's carbon fiber products are manufactured with PAN based medium modulus (33-35 MSI) carbon fiber, not graphite. Carbon fiber has the highest specific stiffness of any commercially available fiber and a very high strength in both tension and compression. The carbon fibers have a surface treatment applied to improve matrix bonding and a chemical sizing which serves to protect the fibers during handling. To maximize the fiber properties, we recommend using an epoxy based resin.

Part	Style	Weave	Weight	Thickness	Count (W x F)	Warp Fiber	Fill Fiber
2.4 oz	84	Plain Weave	2.48 oz/yd2	.006"	16 x 16	1K Carbon Standard Modulus PAN	1K Carbon Standard Modulus PAN
2.9 oz	-	Plain Weave	3.00 oz/yd2	.006"	19.1 x 18.8	1K Carbon Standard Modulus PAN	1K Carbon Standard Modulus PAN
3.5 oz	130	Plain Weave	3.74 oz/yd2	.008"	24 x 24	1K Carbon Standard Modulus PAN	1K Carbon Standard Modulus PAN
5.6 oz	282	Plain Weave	5.78 oz/yd2	.009"	12 x 12	3K Carbon Standard Modulus PAN	3K Carbon Standard Modulus PAN
5.6 oz	284	2x2 Twill Weave	5.78 oz/yd2	.013"	12 x 12	3K Carbon Standard Modulus PAN	3K Carbon Standard Modulus PAN
6.2 oz	94933	2x2 Twill Weave	6.20 oz/yd2	.009"	13.1 x 13.3	3K Carbon Standard Modulus PAN	3K Carbon Standard Modulus PAN
10.9 oz		5H Satin Weave	10.90 oz/yd2	028"	12 x 11.33	6K Carbon Standard Modulus PAN	6K Carbon Standard Modulus PAN
11.2 oz	94910	2x2 Twill Weave	11.14 oz/yd2	.016"	11 x 10.8	6K Carbon Standard Modulus PAN	6K Carbon Standard Modulus PAN
19.75 oz	94940	2x2 Twill Weave	19.44 oz/yd2	.025"	10.7 x 10.2	12K Intermediate Modulus PAN	12K Intermediate Modulus PAN

Fiber	Density	Tensile Strength	Tensile Modulus	Strain to Failure	Specific Tensile Strength	Specific Tensile Modulus	CTE	Decomposition Temp
33MSI	.064 lb/in3	530 ksi	33.5 msi	1.5%	8.33 10^6 in	5.25 10^8 in	-0.33 x 10^-6/°F	6332°F

78 Lindbergh Ave I Livermore, CA 94551
1-800-811-2009 I P. 925-443-5900 I F. 925-443-5901

Appendix B: LS-DYNA Material Type 54-55 Card

*MAT_ENHANCED_COMPOSITE_DAMAGE ***MAT_054-055**

***MAT_ENHANCED_COMPOSITE_DAMAGE**

These are Material Types 54-55 which are enhanced versions of the composite model material type 22. Arbitrary orthothropic materials, e.g., unidirectional layers in composite shell structures can be defined. Optionally, various types of failure can be specified following either the suggestions of [Chang and Chang 1987b] or [Tsai and Wu 1971]. In addition special measures are taken for failure under compression. See [Matzenmiller and Schweizerhof 1991]. This model is only valid for thin shell elements. The parameters in parentheses below apply only to solid elements and are therefore always ignored in this material model. They are included for consistency with material types 22 and 59. By using the user defined integration rule, see *INTEGRATION_SHELL, the constitutive constants can vary through the shell thickness. For all shells, except the DKT formulation, laminated shell theory can be activated to properly model the transverse shear deformation. Lamination theory is applied to correct for the assumption of a uniform constant shear strain through the thickness of the shell. For sandwich shells where the outer layers are much stiffer than the inner layers, the response will tend to be too stiff unless lamination theory is used. To turn on lamination theory see *CONTROL_SHELL.

Card 1

Variable	MID	RO	EA	EB	(EC)	PRBA	(PRCA)	(PRCB)
Type	A8	F	F	F	F	F	F	F

Card 2

Variable	GAB	GBC	GCA	(KF)	AOPT			
Type	F	F	F	F	F			

Card 3

Variable				A1	A2	A3	MANGLE	
Type				F	F	F	F	

*MAT_054-055 *MAT_ENHANCED_COMPOSITE_DAMAGE

Card 4	1	2	3	4	5	6	7	8
Variable	V1	V2	V3	D1	D2	D3	DFAILM	DFAILS
Type	F	F	F	F	F	F	F	F

Card 5

Variable	TFAIL	ALPH	SOFT	FBRT	YCFAC	DFAILT	DFAILC	EFS
Type	F	F	F	F	F	F	F	F

Card 6

Variable	XC	XT	YC	YT	SC	CRIT	BETA	
Type	F	F	F	F	F	F	F	

VARIABLE	DESCRIPTION
MID	Material identification. A unique number or label not exceeding 8 characters must be specified.
RO	Mass density
EA	E_a, Young's modulus - longitudinal direction
EB	E_b, Young's modulus - transverse direction
(EC)	E_c, Young's modulus - normal direction (not used)
PRBA	ν_{ba}, Poisson's ratio ba
(PRCA)	ν_{ca}, Poisson's ratio ca (not used)
(PRCB)	ν_{cb}, Poisson's ratio cb (not used)
GAB	G_{ab}, shear modulus ab
GBC	G_{bc}, shear modulus bc

*MAT_ENHANCED_COMPOSITE_DAMAGE *MAT_054-055

VARIABLE	DESCRIPTION
GCA	G_{ca}, shear modulus ca
(KF)	Bulk modulus of failed material (not used)
AOPT	Material axes option (see MAT_*OPTION* TROPIC_ELASTIC for a more complete description): EQ.0.0: locally orthotropic with material axes determined by element nodes 1, 2, and 4, as with *DEFINE_COORDINATE_NODES. EQ.2.0: globally orthotropic with material axes determined by vectors defined below, as with *DEFINE_COORDINATE_VECTOR. EQ.3.0: locally orthotropic material axes determined by rotating the material axes about the element normal by an angle (MANGLE) from a line in the plane of the element defined by the cross product of the vector v with the element normal. LT.0.0: the absolute value of AOPT is a coordinate system ID number (CID on *DEFINE_COORDINATE_NODES, *DEFINE_COORDINATE_SYSTEM or *DEFINE_COORDINATE_VECTOR). Available in R3 version of 971 and later.
A1 A2 A3	Define components of vector **a** for AOPT = 2.
V1 V2 V3	Define components of vector **v** for AOPT = 3.
D1 D2 D3	Define components of vector **d** for AOPT = 2.
MANGLE	Material angle in degrees for AOPT = 3, may be overridden on the element card, see *ELEMENT_SHELL_BETA or *ELEMENT_SOLID_ORTHO.
DFAILM	Maximum strain for matrix straining in tension or compression (active only for MAT_054 and only if DFAILT > 0). The layer in the element is completely removed after the maximum strain in the matrix direction is reached. The input value is always positive.
DFAILS	Maximum shear strain (active only for MAT_054 and only if DFAILT > 0). The layer in the element is completely removed after the maximum shear strain is reached. The input value is always positive.
TFAIL	Time step size criteria for element deletion: ≤ 0: no element deletion by time step size. The crashfront algorithm only works if t_{fail} is set to a value above zero. $0 < t_{fail} \le 0.1$: element is deleted when its time step is smaller than the given value, >.1: element is deleted when the quotient of the actual time step and the original time step drops below the given value.

*MAT_054-055 *MAT_ENHANCED_COMPOSITE_DAMAGE

VARIABLE	DESCRIPTION
ALPH	Shear stress parameter for the nonlinear term, see Material 22.
SOFT	Softening reduction factor for material strength in crashfront elements (default = 1.0). TFAIL must be greater than zero to activate this option.
FBRT	Softening for fiber tensile strength: EQ.0.0: tensile strength = X_t GT.0.0: tensile strength = X_t, reduced to $X_t * FBRT$ after failure has occurred in compressive matrix mode.
YCFAC	Reduction factor for compressive fiber strength after matrix compressive failure (MAT_054 only). The compressive strength in the fiber direction after compressive matrix failure is reduced to: $X_c = YCFAC * Y_c$ (*default* : $YCFAC = 2.0$)
DFAILT	Maximum strain for fiber tension (MAT_054 only). (Maximum 1 = 100% strain). The layer in the element is completely removed after the maximum tensile strain in the fiber direction is reached. If a nonzero value is given for DFAILT, a nonzero, negative value must also be provided for DFAILC.
DFAILC	Maximum strain for fiber compression (MAT_054 only). (Maximum -1 = 100% compression). The layer in the element is completely removed after the maximum compressive strain in the fiber direction is reached. The input value should be negative and is required if DFAILT > 0.
EFS	Effective failure strain (MAT_054 only).
XC	Longitudinal compressive strength (positive value).
XT	Longitudinal tensile strength, see below.
YC	Transverse compressive strength, b-axis (positive value), see below.
YT	Transverse tensile strength, b-axis, see below.
SC	Shear strength, ab plane, see below.
CRIT	Failure criterion (material number): EQ.54.0: Chang matrix failure criterion (as Material 22) (default), EQ.55.0: Tsai-Wu criterion for matrix failure.
BETA	Weighting factor for shear term in tensile fiber mode (MAT_054 only). ($0.0 \le BETA \le 1.0$)

Remarks:

The Chang/Chang (mat_54) criteria is given as follows:

for the tensile fiber mode,

$$\sigma_{aa} > 0 \quad then \quad e_f^2 = \left(\frac{\sigma_{aa}}{X_t}\right)^2 + \beta\left(\frac{\sigma_{ab}}{S_c}\right) - 1 \begin{cases} \geq 0 \; failed \\ < 0 \; elastic \end{cases},$$

$$E_a = E_b = G_{ab} = \nu_{ba} = \nu_{ab} = 0.$$

for the compressive fiber mode,

$$\sigma_{aa} < 0 \quad then \quad e_c^2 = \left(\frac{\sigma_{aa}}{X_c}\right)^2 - 1 \begin{cases} \geq 0 \; failed \\ < 0 \; elastic \end{cases},$$

$$E_a = \nu_{ba} = \nu_{ab} = 0.$$

for the tensile matrix mode,

$$\sigma_{bb} > 0 \quad then \quad e_m^2 = \left(\frac{\sigma_{bb}}{Y_t}\right)^2 + \left(\frac{\sigma_{ab}}{S_c}\right)^2 - 1 \begin{cases} \geq 0 \; failed \\ < 0 \; elastic \end{cases},$$

$$E_b = \nu_{ba} = 0. \quad \rightarrow G_{ab} = 0,$$

and for the compressive matrix mode,

$$\sigma_{bb} < 0 \quad then \quad e_d^2 = \left(\frac{\sigma_{bb}}{2S_c}\right)^2 + \left[\left(\frac{Y_c}{2S_c}\right)^2 - 1\right]\frac{\sigma_{bb}}{Y_c} + \left(\frac{\sigma_{ab}}{S_c}\right)^2 - 1 \begin{cases} \geq 0 \; failed \\ < 0 \; elastic \end{cases},$$

$$, = \nu_{ba} = \nu_{ab} = 0. \quad \rightarrow G_{ab} = 0$$
$$X_c = 2Y_c \quad for\ 50\%\ fiber\ volume$$

In the Tsai-Wu (MAT_055) criteria the tensile and compressive fiber modes are treated as in the Chang-Chang criteria. The failure criterion for the tensile and compressive matrix mode is given as:

$$e_{mc}^2 = \frac{\sigma_{ba}^2}{Y_c Y_t} + \left(\frac{\sigma_{ab}}{S_c}\right)^2 + \frac{(Y_c - Y_t)\sigma_{bb}}{Y_c Y_t} - 1 \begin{cases} \geq 0 \; failed \\ < 0 \; elastic \end{cases}$$

For β=1 we get the original criterion of Hashin [1980] in the tensile fiber mode. For β=0 we get the maximum stress criterion which is found to compare better to experiments.

In MAT_054, failure can occur in any of four different ways:

1. If DFAILT is zero, failure occurs if the Chang-Chang failure criterion is satisfied in the tensile fiber mode.

2. If DFAILT is greater than zero, failure occurs if the tensile fiber strain is greater than DFAILT or less than DFAILC.

3. If EFS is greater than zero, failure occurs if the effective strain is greater than EFS.

4. If TFAIL is greater than zero, failure occurs according to the element timestep as described in the definition of TFAIL above.

When failure has occurred in all the composite layers (through-thickness integration points), the element is deleted. Elements which share nodes with the deleted element become "crashfront" elements and can have their strengths reduced by using the SOFT parameter with TFAIL greater than zero.

Information about the status in each layer (integration point) and element can be plotted using additional integration point variables. The number of additional integration point variables for shells written to the LS-DYNA database is input by the *DATABASE_EXTENT_BINARY definition as variable NEIPS. For Models 54 and 55 these additional variables are tabulated below (i = shell integration point):

History Variable	Description	Value	LS-Prepost history variable
1. $ef(i)$	*tensile fiber mode*	*1 - elastic* *0 - failed*	*1*
2. $ec(i)$	*compressive fiber mode*		*2*
3. $em(i)$	*tensile matrix mode*		*3*
4. $ed(i)$	*compressive matrix mode*		*4*
5. $efail$	*max(ef(ip))*		*5*
6. *dam*	*damage parameter*	*-1 - element intact* *10^{-8} - element in crashfront* *+1 – element failed*	*6*

These variables can be plotted in LS-Prepost element history variables 1 to 6. The following components, defined by the sum of failure indicators over all through-thickness integration points, are stored as element component 7 instead of the effective plastic strain.

Description	Integration point
$\frac{1}{nip}\sum_{i=1}^{nip} ef(i)$	*1*
$\frac{1}{nip}\sum_{i=1}^{nip} ec(i)$	*2*
$\frac{1}{nip}\sum_{i=1}^{nip} em(i)$	*3*

Appendix C: LS-DYNA Material Type 63 Card

*MAT_063 *MAT_CRUSHABLE_FOAM

***MAT_CRUSHABLE_FOAM**

This is Material Type 63 which is dedicated to modeling crushable foam with optional damping and tension cutoff. Unloading is fully elastic. Tension is treated as elastic-perfectly-plastic at the tension cut-off value. A modified version of this model, *MAT_MODIFIED_ CRUSHABLE_FOAM includes strain rate effects.

Card 1	1	2	3	4	5	6	7	8
Variable	MID	RO	E	PR	LCID	TSC	DAMP	
Type	A8	F	F	F	F	F	F	
Default	none	none	none	none	none	0.0	0.10	

VARIABLE	DESCRIPTION
MID	Material identification. A unique number or label not exceeding 8 characters must be specified.
RO	Mass density
E	Young's modulus
PR	Poisson's ratio
LCID	Load curve ID defining yield stress versus volumetric strain, γ, see Figure 63.1.
TSC	Tensile stress cutoff. A nonzero, positive value is strongly recommended for realistic behavior.
DAMP	Rate sensitivity via damping coefficient (.05<recommended value<.50).

Remarks:

The volumetric strain is defined in terms of the relative volume, V, as:

$$\gamma = 1.-V$$

The relative volume is defined as the ratio of the current to the initial volume. In place of the effective plastic strain in the D3PLOT database, the integrated volumetric strain is output.

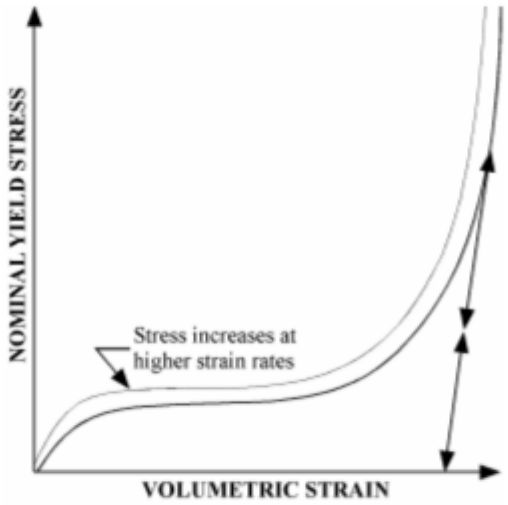

Figure 63.1. Behavior of strain rate sensitive crushable foam. Unloading is elastic to the tension cutoff. Subsequent reloading follows the unloading curve.

Appendix D: LS-DYNA Material Type 4 Card

*MAT_003 *MAT_PLASTIC_KINEMATIC

*MAT_PLASTIC_KINEMATIC

This is Material Type 3. This model is suited to model isotropic and kinematic hardening plasticity with the option of including rate effects. It is a very cost effective model and is available for beam (Hughes-Liu and Truss), shell, and solid elements.

Card 1

	1	2	3	4	5	6	7	8
Variable	MID	RO	E	PR	SIGY	ETAN	BETA	
Type	A8	F	F	F	F	F	F	
Default	none	none	none	none	none	0.0	0.0	

Card 2

Variable	SRC	SRP	FS	VP				
Type	F	F	F	F				
Default	not used	not used	not used	0.0				

VARIABLE	DESCRIPTION
MID	Material identification. A unique number or label not exceeding 8 characters must be specified.
RO	Mass density.
E	Young's modulus.
PR	Poisson's ratio.
SIGY	Yield stress.
ETAN	Tangent modulus, see Figure 3.1.
BETA	Hardening parameter, $0 < \beta' < 1$. See comments below.
SRC	Strain rate parameter, C, for Cowper Symonds strain rate model, see below. If zero, rate effects are not considered.

VARIABLE	DESCRIPTION
SRP	Strain rate parameter, P, for Cowper Symonds strain rate model, see below. If zero, rate effects are not considered.
FS	Failure strain for eroding elements.
VP	Formulation for rate effects: EQ.0.0: Scale yield stress (default), EQ.1.0: Viscoplastic formulation

Remarks:

Strain rate is accounted for using the Cowper and Symonds model which scales the yield stress with the factor

$$1+\left(\frac{\dot{\varepsilon}}{C}\right)^{1/P}$$

where $\dot{\varepsilon}$ is the strain rate. A fully viscoplastic formulation is optional which incorporates the Cowper and Symonds formulation within the yield surface. An additional cost is incurred but the improvement allows for dramatic results. To ignore strain rate effects set both SRC and SRP to zero.

Kinematic, isotropic, or a combination of kinematic and isotropic hardening may be specified by varying β' between 0 and 1. For β' equal to 0 and 1, respectively, kinematic and isotropic hardening are obtained as shown in Figure 3.1. For isotropic hardening, $\beta' = 1$, Material Model 12, *MAT_ISOTROPIC_ELASTIC_PLASTIC, requires less storage and is more efficient. Whenever possible, Material 12 is recommended for solid elements, but for shell elements it is less accurate and thus Material 12 is not recommended in this case.

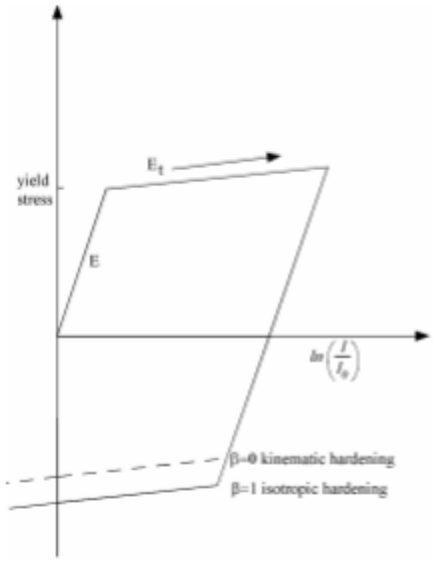

Figure 3.1. Elastic-plastic behavior with kinematic and isotropic hardening where l_0 and l are undeformed and deformed lengths of uniaxial tension specimen. E_t is the slope of the bilinear stress strain curve.

Appendix E: Aluminum 2024-T3 Alloy Sheet Mechanical Properties

Physical Properties	Metric	English	Comments
Density	2.78 g/cc	0.1 lb/in³	AA; Typical
Mechanical Properties			
Hardness, Brinell	120	120	AA; Typical; 500 g load; 10 mm ball
Hardness, Knoop	150	150	Converted from Brinell Hardness Value
Hardness, Rockwell A	46.8	46.8	Converted from Brinell Hardness Value
Hardness, Rockwell B	75	75	Converted from Brinell Hardness Value
Hardness, Vickers	137	137	Converted from Brinell Hardness Value
Ultimate Tensile Strength	483 MPa	70000 psi	AA; Typical
Tensile Yield Strength	345 MPa	50000 psi	AA; Typical
Elongation at Break	18 %	18 %	AA; Typical; 1/16 in. (1.6 mm) Thickness
Modulus of Elasticity	73.1 GPa	10600 ksi	AA; Typical; Average of tension and compression. Compression modulus is about 2% greater than tensile modulus.
Notched Tensile Strength	379 MPa	55000 psi	2.5 cm width x 0.16 cm thick side-notched specimen, K_t = 17.
Ultimate Bearing Strength	855 MPa	124000 psi	Edge distance/pin diameter = 2.0
Bearing Yield Strength	524 MPa	76000 psi	Edge distance/pin diameter = 2.0
Poisson's Ratio	0.33	0.33	
Fatigue Strength	138 MPa	20000 psi	AA; 500,000,000 cycles completely reversed stress; RR Moore machine/specimen
Machinability	70 %	70 %	0-100 Scale of Aluminum Alloys
Shear Modulus	28 GPa	4060 ksi	
Shear Strength	283 MPa	41000 psi	AA; Typical
Electrical Properties			
Electrical Resistivity	5.82e-006 ohm-cm	5.82e-006 ohm-cm	AA; Typical at 68°F
Thermal Properties			
CTE, linear 68°F	23.2 µm/m-°C	12.9 µin/in-°F	AA; Typical; Average over 68-212°F range.
CTE, linear 250°C	24.7 µm/m-°C	13.7 µin/in-°F	Average over the range 20-300°C
Specific Heat Capacity	0.875 J/g-°C	0.209 BTU/lb-°F	
Thermal Conductivity	121 W/m-K	840 BTU-in/hr-ft²-°F	AA; Typical at 77°F
Melting Point	502 - 638 °C	935 - 1180 °F	AA; Typical range based on typical composition for wrought products 1/4 inch thickness or greater. Eutectic melting is not eliminated by homogenization.
Solidus	502 °C	935 °F	AA; Typical
Liquidus	638 °C	1180 °F	AA; Typical